UC Berkeley
UC Berkeley Electronic Theses and Dissertations

Title
Optical Investigations of Intermolecular Electron Dynamics in Low Dimensional Materials

Permalink
https://escholarship.org/uc/item/7wx3331c

Author
Balch, Halleh Baratloo

Publication Date
2019

Peer reviewed|Thesis/dissertation

Optical Investigations of Intermolecular Electron Dynamics in Low Dimensional Materials

by

Halleh Baratloo Balch

A dissertation submitted in partial satisfaction of the

requirements for the degree of

Doctor of Philosophy

in

Physics

in the

Graduate Division

of the

University of California, Berkeley

Committee in charge:

Professor Feng Wang, Chair
Professor Jeffrey B. Neaton
Professor Ming C. Wu

Fall 2019

Optical Investigations of Intermolecular Electron Dynamics in Low Dimensional Materials

Abstract

Optical Investigations of Intermolecular Electron Dynamics in Low Dimensional Materials

by

Halleh Baratloo Balch

Doctor of Philosophy in Physics

University of California, Berkeley

Professor Feng Wang, Chair

The interaction of electrons with an electromagnetic field is one of the most important phenomena in physics. The electromagnetic interaction is central to the absorption and emission of light by matter and permits interpretation of physical phenomena in our natural world. This dissertation uses light-matter interactions to probe the behavior of electrons in atomically thin materials and to develop new scientific tools for the study of intermolecular dynamics.

In Part I, we present and demonstrate a set of principles that permit the rational design of two dimensional covalent organic frameworks with optical and electronic properties not present in their constituent counterparts. We develop a novel low bandgap framework that is characterized under broadband optical spectroscopy, X-ray scattering, transmission electron microscopy, atomic force microscopy, and transport. In inorganic/organic van der Waals heterostructures, we report ultrafast electron dynamics not previously observed in two dimensional covalent organic frameworks with consequences that are relevant to a broad range of materials.

In Part II, we manipulate light-matter interactions in atomically thin materials to develop an optical sensor capable of imaging electric fields generated by intermolecular dynamics. We combine the unique gate-variable optical transitions in graphene with critically-coupled waveguide amplification to convert electrical activity into optical signals while retaining high spatio-temporal resolution. We apply this technique to living systems and noninvasively image signals from and among electrically active cells.

To
Moji and Clif

Contents

II Imaging Electric Fields   47

List of Figures

Acknowledgments

My time in graduate school has been immensely enjoyable thanks to the people who have filled it and what we have been able to accomplish together.

First and foremost, I thank my adviser Feng Wang. The depth of his knowledge, his enthusiasm and curiosity, and his insistence on developing a "simple physical picture" has informed my own approach in research. I am incredibly grateful to Feng for his support in exploring my research interests, which often pushed the boundary of our lab. Extremely well-read on an incredible breadth of scientific research, he proposes interesting ideas and provides helpful suggestions. He surrounded me with excellent scientists and let me run a bit rogue; I am indebted to him for a wonderful experience.

I am grateful to Y. Ron Shen, whose door was always open for guidance and consultation. Throughout graduate school, Ron has provided a unique and encouraging perspective on my career development. Ron's emphasis that fundamental research be meaningful and motivated underpins his rigorous questions and has made me a better scientist and communicator.

I also extend thanks to those who have served on my committees: to Jeff Neaton, whose capacity for productive research at the intersections of scientific disciplines I admire and aspire towards, and whose helpful and encouraging words I deeply appreciate; to Mike Crommie who never fails to define an interesting vision, bespeckled with humor and curiosity. Thanks go to Michael Nacht, who encouraged my interest in the interface of science, public policy, and diplomacy. I am further grateful to Vivek Subramanian and Ming Wu for serving as my external members and for their interest in the work presented here.

The work in this dissertation was made possible and fun due to two highly interdisciplinary collaborations.

Part One of the work presented here is the output of a collaboration that demonstrates what is possible when you bring expertise from neighboring disciplines to a scientific problem outside the scope of any one. Will Dichtel, Seth Marder, Jean-Luc Bredas, and Dan Ralph stand as role models for leadership and mentorship I hope to emulate throughout my owrn work. I have had the great fortune of working with their excellent students and postdocs, whose patience and enthusiasm for working on new and hard problems was invaluable. I am indebted to Michio Matsumoto, Ryan Bisbey, Austin Evans, Reddy Dasari, Hong Li, Simil Thomas, and Ruofan Li for teaching me about synthetic chemistry, DFT, and transport; each made unique and significant contributions in the development of low-bandgap frameworks and I'm grateful to call them friends.

Second, I'd like to thank Bianxiao Cui for starting our collaboration at Stanford– and for allowing us to take over a significant amount of her lab space with our optical setup. The second part of this dissertation owes its existence to the dogged teammate I found in Allister McGuire. Thank you, Allister, for staying in lab way past dinner, letting us into the building on weekends, and shuttling extremely expensive research equipment between Palo Alto and Berkeley. It's been great fun to go through our graduate years in parallel and I'm extremely grateful for your support, good humor, and friendship.

thoughtfulness, and tenacity I deeply admire. A most special thanks to Jane Tandler and Claire Wallace, friends who will remain from the first day of school until long past the last. I often think there's no better place to do a PhD than at Berkeley, maybe because in one way or another, you've all been here.

Finally, thank you to my family for your unwavering support and enthusiasm. To Andreas Bastian, who jumped up each day and picked up far more than his equitable fifty: thank you for making the sum of ones way more than two and for being a total goofball. To my grandparents Nini Rahbari and Ami Baratloo, John and Olga Balch, your stories and support make it evident that anything is possible. To Arash Baratloo and to Shahla Butler, whose advice and experience stretched and strengthened me. To my father, Clifton Balch, and my mother, Mojdeh Baratloo, who taught me to appreciate the beauty in design, the satisfaction in seeing your ideas become a reality, and to find enjoyment in the every day.

Preface

> ...It begins with a scene one meter wide which we view from just one meter away...One hundred meters wide, the distance a man can run in ten seconds, cars crowd the highway, power boats lie at their docks, the colorful bleachers are Soldier Field. This square is a kilometer wide, one thousand meters, the distance a racing car can travel in ten seconds. We see the Great City on the lake shore. Ten to the fourth meters, ten kilometers, the distance a supersonic airplane can travel in ten seconds. We see first around and the end of Lake Michigan, then the whole Great Lake. Ten to the fifth meters, the distance a hovering satellite covers in ten seconds, long parades of clouds, the day's weather in the Middle West. Ten to the sixth, a one with six zeros, a million meters. Soon the Earth will show as a solid sphere. We are able to see the whole Earth now, just over a minute along the journey. The Earth diminishes into the distance but those background stars are so much farther away that they do not yet appear to move. A line extends at the true speed of light....

<div align="right">

Charles and Ray Eames
Powers of Ten

</div>

Through an interplay of scientific discovery and design, this dissertation examines how the interactions of electrons within and among molecules gives rise to physical phenomena emergent across extended length scales. Throughout, we connect the behavior of light and matter at the microscopic length scales to the physical properties and dynamic processes we experience in our every day. In doing so, we span lengths from our built world (e.g. an experimental apparatus) on the order of 1 meter to that of an atom, $\frac{1}{10000000000}$ meter.[1] The diversity of the natural world emerges through the vast number of possible combinations of these atoms. Sir William H. Bragg, known best for his work resolving the atomic structure of crystals through X-ray diffraction, puts it well in his lecture to the Royal Society, *The Atoms of Which Things are Made* [1]:

> The atoms may be compared to the letters of the alphabet, which can be put together into innumerable ways to form words. So the atoms are combined in

---

[1]Since "size" of an atom is ill-defined, I'm describing the size of an atom by the radius from the nucleus to the outer shell of electrons as observed in liquid or solid form.

> equal variety to form what are called molecules. We may even push the analogy
> a little further and say the the association of words into sentences and passages
> conveying meanings of every kind is like the combination of molecules of all kinds
> and in all proportions to form structures and materials that have an infinite
> variety of appearances and properties and can carry what we speak of as life.
>
> W.H Bragg (1925)

This dissertation is organized into two parts:

In Part I, I measure, describe, and utilize combinations of molecules to develop a new class of periodic crystals formed with the chemical and physical diversity afforded by molecular combinations. I focus on the interaction of light and electrons in these molecular materials and outline a set of rules that permit rational design of unique physical phenomena. I describe how, when starting with molecular building blocks, one can realize specific and at times novel physical properties due to the interaction of light and matter and how these properties can be modified in unexpected ways by reduced dimensionality. This first section develops a simplified framework that both uncovers novel physical phenomena that emerge when electrons are confined to reduced dimension, and also might lend understanding to the far greater complexity of molecular structures formed in our natural world.

In Part II, I develop a new tool of optical imaging capable of resolving intermolecular dynamics in space and time. Here, we observe rather than synthesize the complexity present in the natural world. I use our understanding of the unique interaction of light and matter in atomically thin materials and photonic structures to form a spatially resolved image of local electric field distributions produced by dynamic and non-equillibrium aqueous charged systems. The physical observable I detect is the local electric field, which underpins the electronic interactions that drive intermolecular dynamics. The natural world is built of these complex structures and their dynamics make possible the conversion of light to chemical energy in photosynthesis, the (literal) fabric of high-performance materials that persist under extreme heat, pressure, and temperature, and the dynamics of biochemical processes underpinning living organisms. I apply this platform, quite literally, to structures that "carry what we speak of as life" and image the action potentials produced by electrically active biological cells, resolving their local electric fields with single-cell resolution across a wide field-of-view.

This dissertation articulates two complementary research approaches: one based on a discovery-driven approach to scientific unknowns, the other grounded in the development of new tools that permit posing of questions previously unasked. The first, I consider hypothesis-driven or discovery-driven research in which one (basically) asks, "How does X work?". This is a very fun and often far-ranging approach that benefits from experience and interest in many complementary fields, techniques, and scientific underpinnings. The second, I think of as a tool-building or "invention-driven" approach. Here, we have a rather

specific scientific problem and have realized that the necessary measurement requires a tool that does not yet exist. This second approach requires more exactly scoped research. The invention of a new technique requires an idea with an anticipated outcome. But, with the tightly-scoped tolerances come a unique measurement capability that has the possibility of opening up completely new fields of discovery. The dual approach to these scientific questions permit us to develop both a new set of design principles that connect how combinations of molecules can give rise to materials host to unusual physical phenomena and also to develop completely new methods of unraveling dynamic underpinnings in complex molecular materials. Experience integrating both approaches remains one of the greatest joys of my time in graduate school and has made this entire research portfolio an extremely satisfying pursuit.

H.B.B.
UC Berkeley

Part I

Design and Control of Two-dimensional Materials

Chapter 1

Light, Matter, Atoms, and Molecules

> We'll just have to remind ourselves that no one - no scientist, no physicist, no genealogist, no physiologist - has ever discovered anything that can be called a solid. What they have discovered is that our physical universe is energy, and that energy events are relatively very, very remote from one another: atoms, the proton, and electron are as remote from each other as our sun and earth. Physics has found no solids! ... There are no surfaces, there are no solids, there are no straight lines, there are no planes.
>
> Buckminster Fuller

1.1   Introduction

The difference between the transport of charge through a pure metal (10^{-12} Ω-m) and a good insulator (10^{20} Ω-m) can span a range of 10^{30}, which is roughly the scale between us and the diameter of our universe. The scale of this diversity comes from the geometry and the extent to which atoms combine to form a solid and how their electrons interact [2]. Our understanding of these facets of the physical world is of both fundamental and practical importance having led us to an increased understanding of how the quantum mechanical description of atoms and electrons produces some of the robust complexity in our natural world and to the development of useful technologies. Richard Feynman notes [3]:

> If, in some cataclysm, all of scientific knowledge were to be destroyed, and only one sentence passed on to the next generations of creatures, what statement would contain the most information in the fewest words? I believe it is the *atomic hypothesis* (or the atomic *fact*, or whatever you wish to call it) that *all things are made of atoms – little particles that move around in perpetual motion, attracting each other when they are a little distance apart, but repelling upon being squeezed into one another.* In that one sentence, you will see, there is an

enormous amount of information about the world, if just a little imagination and thinking are applied.

The interaction of electrons with an electromagnetic field is one of the most important phenomena in physics. This interaction is responsible for the cohesion of atoms and for the formation of molecules. The electromagnetic interaction is central to the absorption and emission of light by matter, the study of which provides insight into the structure and dynamics of the atoms and molecules and the applications that enable their control. Understanding the mechanisms of the interaction between electrons, atoms, molecules, and the electromagnetic field is essential to our interpretation of physical phenomena in our environment.

The following sections will provide an introduction to a few aspects of how atoms combine to form organic and inorganic materials and their response to an external electromagnetic field and will focus on the topics most relevant to the research presented here.[1]

1.2 Band theory

What is the origin of the electronic bandgap? Let's start with an atom of N electrons. From the Pauli exclusion principle, we know that two electrons cannot have the same state and that the electrons will populate the energy levels sequentially leading to a set of filled states and a set of unoccupied states. The lowest energy transition takes place between the highest occupied state, $|\Psi\rangle$ and the lowest unoccupied state, $|\Psi^*\rangle$ and has energy $\langle\Psi| H |\Psi^*\rangle = E_0$. In molecular parlance, these are referred to as the HOMO and LUMO levels, respectively. However, as we shall see, in a periodic crystal these discrete energy levels will transform into the valence and conduction bands and give rise to a range of physical phenomena not present in their discrete counterparts.

Imagine now bringing two atoms together, where the lowest unoccupied state of atom A is $|\Psi_A\rangle$ and likewise that of atom B is $|\Psi_B\rangle$. As A and B are brought in close proximity, their electronic orbitals will begin to overlap. In a simple picture, we can model this overlap as an interaction between the excited state of the respective atoms, $\langle\Psi_A^*| H |\Psi_B^*\rangle$, corresponding to the off-diagonal matrix element. For a nondegenerate system, $\langle\Psi_A^*| H |\Psi_B^*\rangle = \lambda$ and the

---

[1]There are many excellent several-hundred page texts that contain formal and informal discussion of condensed matter and solid state physics. Favorites of these include J.M Ziman's *Principles of the Theory of Solids*, sprinkled with witty Shakespearean quotes, M.S. Dresselhaus's lecture notes *Solid State Physics (2001)*, Peierls's *Quantum Theory of Solids. Atom-Photon Interactions* by C. Cohen-Tannoudji, J Dupont-Roc, and Gilbert Grynberg provides an advanced perspective on light-matter interactions and is a good complement to Yu and Cardona's *Fundamentals of Semiconductors*, which has a bit of everything for everyone. Of course, no list from a Berkeley PhD would be complete without including Charles Kittel's *Introduction to Solid State Physics*, which is effective at covering a large range of material under a rather simple mathematical framework and is enduring despite its insistent and incessant use of both CGS and SI units throughout.

excited state component of the Hamiltonian of the joint systems can be written:

$$H = \begin{bmatrix} \langle \Psi_A^* | \Psi_A^* \rangle & \langle \Psi_A^* | \Psi_B^* \rangle \\ \langle \Psi_B^* | \Psi_A^* \rangle & \langle \Psi_B^* | \Psi_B^* \rangle \end{bmatrix} = \begin{bmatrix} E_0 & -\Delta \\ -\Delta & E_0 \end{bmatrix} \tag{1.1}$$

Diagonalizing the excited state component of the Hamiltonian, we find eigenvalues $\lambda_\pm = E_0 \pm \Delta$ where the excited state energy E_0 has split into two states, $E_0 + \Delta$ and $E_0 - \Delta$. As we extend our two-atom system to a complete crystalline solid, the compounding splittings result in infinitesimally small energy differences that ultimately comprise a single "energy band". The occupied orbital states form the valence bands while the unoccupied states form the conduction bands and we describe the difference between the highest energy state in the valence band and the lowest energy in the unoccupied band as the *band gap*.
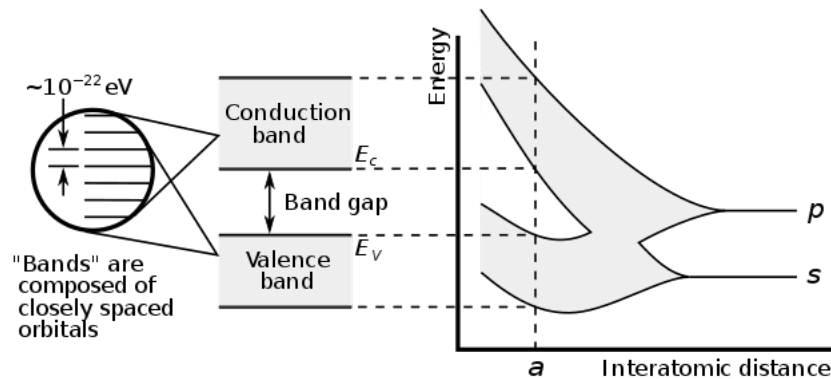
Figure 1.1: Schematic of the origin of the electronic band gap [4].

Say we now turn on an external electric field. If the energy bands are either filled or empty, no electrons will move and this crystal will behave as an insulator. In contrast, if one of the energy bands is only partly filled, the energy gap has been breached, and the solid will conduct as a metal. Semiconducting behavior arises when the valence (conduction) band should be fully filled (empty) but the energy energy gap, E_g, is only slightly larger than the thermal energy of the system $k_B T$ (usually on the order of hundreds of meV to a few eV). In this event, conducting behavior can be induced by exciting electrons across the gap (into the aptly-named conduction band) using a small external potential, or light in the ultraviolet (UV) to near-infrared (NIR).

As is apparent, the final landing spot of electrons in the formation of a solid has an enormous impact in the subsequent physical phenomena present in the material. Many aspects of a solid's electronic properties can be estimated by counting the number of distinct electronic wavefunctions per unit cell of the solid [5]. Recall that in a crystal with perfect translation symmetry, momentum is a well-defined quantum number. From periodic boundary conditions we know at that there are exactly as many allowed wave vectors in the Brillouin zone as there are unit cells in the crystal. Each wave vector, $\vec{k}$, corresponds to a

distinct spatial electronic wave function in the crystal. In accordance with the Pauli exclusion principle, each spatial wavefunction can support 2 electrons: one spin up, and another, spin down. In a crystal comprised of N unit cells, we can count N allowed wave vectors and 2N electronic states. These 2N electronic states correspond to two electron states per band per unit cell. As such, knowing the number of electrons per unit cell can provide good insight in to the electronic properties of the crystal as a whole:

1. A solid with one electron per unit cell is always a metal. These systems will always have a half-filled band, no bandgap, and will conduct.

2. A solid with an odd number of electrons is always a metal. Each electronic band can support two and no more than two electrons, an odd number of electrons will always result in a half-filled band, no bandgap, and permit conductivity.

3. An even number of electrons per unit cell does not always have a band gap. Though an even number of electrons will result in fully-filled bands, these bands can overlap in energy. As a result, it can be energetically favorable to populate upper bands, leaving lower bands unfilled.

4. All divalent elements are metals and all tetravalent metals are either metals or semi-conductors.

5. The transition metals, some of which we will discuss in further detail, contain incomplete d-orbitals when higher energy states are filled. When transition metals atoms are brought together to form a solid, the high energy $4s$ electrons will form an 's-like' band, appearing similar to a conduction band in a simple metal. Meanwhile, the d-electrons will remain localized close to the atomic core. However, the overlap of electronic wavefunctions will form a 'd-like' band that can contain up to 10 electrons. In a lattice, the s-band and d-band will hybridize to form a partially-filled band that promotes s-like electron conduction.

These simple rules of thumb offer a framework for the design of inorganic lattices, which we will extend to that of organic systems in later parts of this text.

1.3 A brief review of σ and π electrons and their bonds

Many striking features of semiconducting materials – both inorganic and organic – can be understood by invoking a rather simple description of π and σ bonds and understanding their respective behaviors. As is common throughout this text, we begin with the carbon atom. A carbon atom is host to six electrons. From the tetrahedral infrastructure of diamond to

the mirror planes of acetylene and the aromatic benzene, the diversity of carbon bonding permits much of the diversity we observe in the natural world [6].

We start in the fully bonded case: diamond. As illustrated in the top panel of Figure 1.2, a carbon atom's four valence electrons involve a combination of 2s and 2p orbitals. When mixed into four sp^3 hybrid orbitals, these outer shell electrons can form four single bonds with a tetrahedral geometry. In diamond, the carbon lattice is formed through single bonds from the overlap of an sp^3 orbital of one carbon atom and the orbital of a bonded atom along the inter-nuclear axis. As a result, these bonds are axially symmetric and are called σ-bonds with the associated electrons termed σ-electrons. A complete crystal of such a bonding structure forms what we know of as diamond. The tetrahedral symmetry forms a rigid three-dimensional structure that accounts for diamond's strength, durability, and hardness.
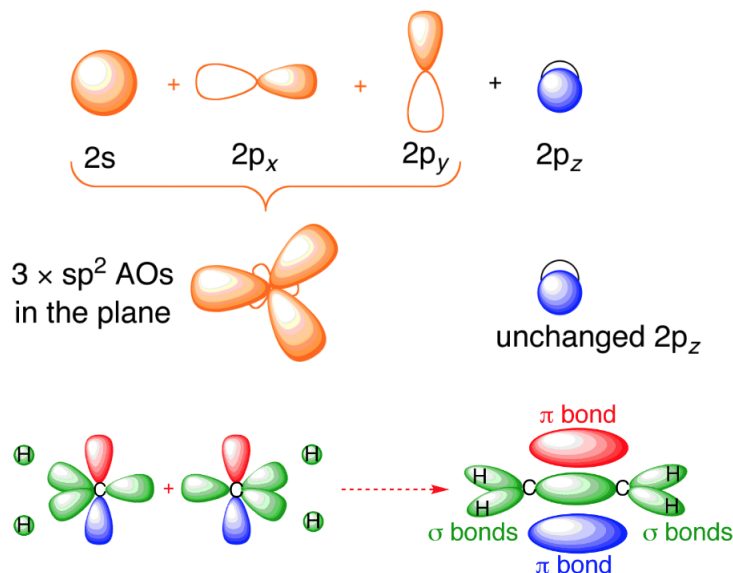
Figure 1.2: Illustration of π and σ bonds of an ethylene molecule [7].

Now in contrast, were we to bring together two carbon atoms such that they form a double bond, we now have the compound *ethylene* (Figure 1.2). Instead of forming sp^3 hybridized orbitals, the electrons undergo sp^2 hybridization to form three sp^2 hybridized orbitals. These orbitals form three σ bonds: one between the two carbon atoms and two each with hydrogen atoms. However, unlike in the fully bonded diamond structure, in ethylene there is a remaining electron in the 2p orbital of each of the carbon atoms. This spare 2p-type electron we enumerate $2p_z$ and protrudes perpendicular to the intermolecular axis. When two carbon atoms of this electronic configuration are brought into proximity,

the unpaired electrons in the $2p_z$ orbital overlap laterally to form a π bond and associated π-electrons.

A most special case of carbon bonding occurs when the set of atoms is host to alternating double and single bonds, forming a chain or ring structure (Figure 1.3). Such structures are referred to as *conjugated* structures whose bonding permit the π-electrons to move over the entire extent of the molecule. The electrons in conjugated systems have
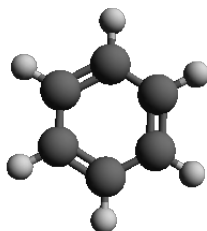
Figure 1.3: Illustration of a benzene ring with alternating double and single bonds.

greater kinetic energy (and less potential energy) than their non-conjugated counterparts. As a consequence, it is instructive to treat the π electrons and σ electrons separately. For example, π bonds are considerably weaker than σ bonds. As a result, the lowest energy electronic excitations are the $\pi - \pi*$ transitions with an energy gap in the visible regime and are of central interest to the research presented in this dissertation. When studying
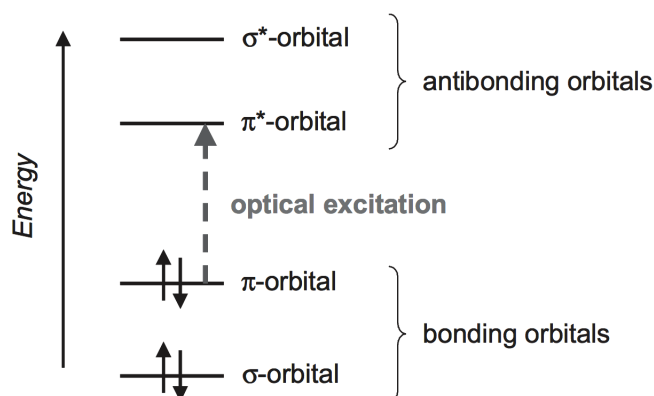
Figure 1.4: Energy levels of a π-conjugated molecule [8].

the electronic properties of conjugated organic molecules and their crystalline complexes (as we do here), we can apply semi-empirical approaches and use a simplified Hamiltonian that takes only the π electrons into account. The simplest model treats the π electrons in a free-electron model and approximate the π electrons are moving in a box of an effective length defined by the size of the molecule [6]. Like the quantum mechanical particle in a

box, conjugated systems of longer extent will be host to lower energy excited state transitions. This simplest "particle in a box" approach is actually quite instructive in estimating electronic and optical properties of the system (for example, the bandgap) [9]. And, as we will see, even this simple description will be sufficient for an informative interpretation of the optical and electronic properties observed in new periodic lattices of two-dimensional covalently-bound organic frameworks.

Chapter 2

Introduction to Covalent Organic Frameworks

> You can't start with pure color. You start with light.

<div align="right">Sheila Hicks</div>

2.1   Everything starts with carbon

We start with the carbon atom and its now familiar six valence electrons. If we stitch six such carbon atoms together, we form what is called by the organic chemists, a benzene ring. The atoms in the benzene ring, shown in Figure 2.1, is held together by six alternating double and single bonds– three of each.

carbon   benzene   graphene   π-bonded
                  ring   sheet   monomolecular networks
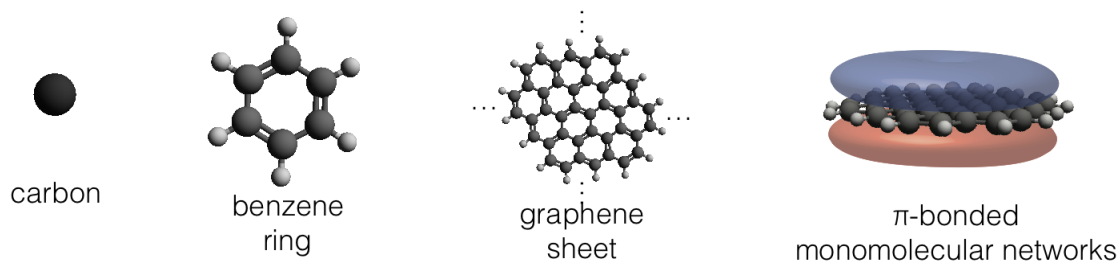
Figure 2.1: Illustration of the formation of a π-bonded network.

Now imagine we take many such benzene rings and stitch *them* together. We have formed a single sheet of graphene: not by removing material from a crystal from the earth, but rather from the ground up, built from its atomic and molecular constituent parts. As discussed in our review of σ and π bonds, these benzene rings will fuse together through

σ bonds, leaving one $2pz$ electron projecting roughly perpendicular to the plane. In this model, we can consider graphene the simplest covalently bound molecular lattice.

2.2 A molecular library for design

The next question we pose is, to what extent is it possible to extend this idea to the broader family of planar molecules, which encompass a vast set of possible starting building blocks. Leveraging the tools of synthetic chemistry, this approach opens up a library of molecular
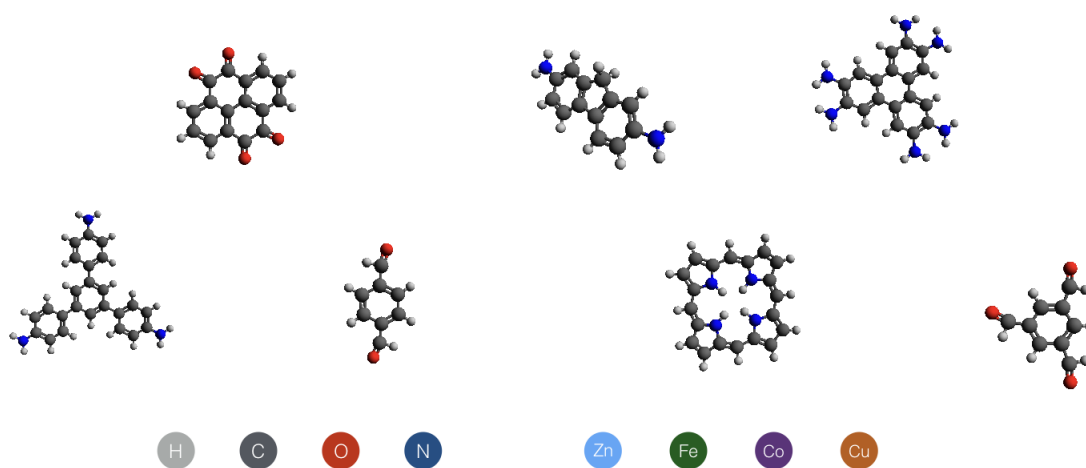
Figure 2.2: A myriad of planar organic molecules.

building blocks with which to design and build new crystals with long range electronic coupling and molecular precision. By varying the linkage chemistry and functionalization, we can further tune the intermolecular bonding, electron, and phonon coupling, and eventually even observe new optical, electronic, and magnetic properties as a function of symmetry and dimension.

2.3 Symmetry and dimension in 2D covalent organic frameworks

Two dimensional covalent organic frameworks (2D COFs) are an emerging class of layered 2D materials comprised of planar conjugated molecules organized through in-plane covalent bonds into a periodic crystal. The conjugation of the underlying lattice gives rise to π-bonded orbitals that permit van der Waals interlayer coupling in the stacking direction.

We describe the constituent molecules as *node* and *linker* molecules. The 2D COF is formed through the bonding of the node and linker molecules along their planar axes,
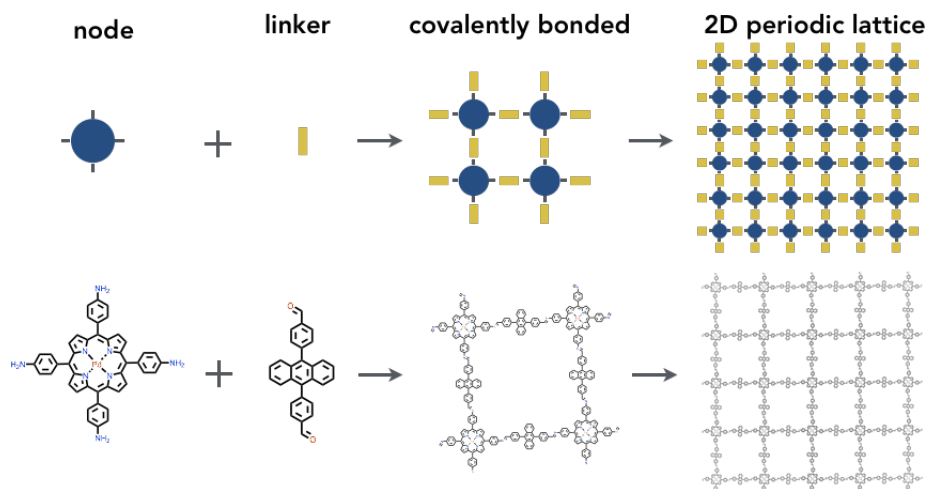
Figure 2.3: Design and construction of the geometric framework lattice.

where choice of this bond sets the geometric structure of the lattice and guides many of the physical properties of the crystal (Figure 2.3).

four-fold symmetric node

three-fold symmetric node
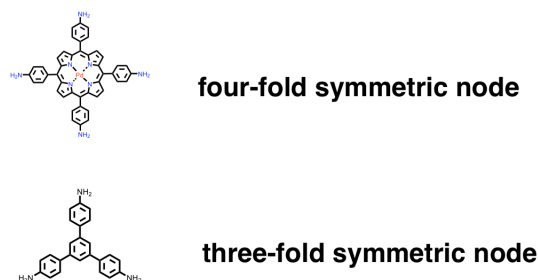
Figure 2.4: Symmetry of the COF node.

Elegantly, the symmetry of the lattice is set by the symmetry of the node. A $2n$-fold symmetric node will form a rectangular, oblique, or square lattices, whereas a $3n$-fold symmetric node will form a lattice in the hexagonal symmetry group. Lattice parameters, such as the lattice constant, is largely set by the linker molecule (Figure 2.6). There are few key features to note at this time. First, choice of the linker molecule can vary the lattice constant, a, from less than 2nm to over 5nm [10].

Second, it is worthwhile to remember that these lattice constants are an *order of magnitude* larger than that of their inorganic counterparts. The consequences of this are profound. A small but perhaps one of the more intuitive examples are in consideration of the first Brillouin zone of the crystal. The inter-layer ($\pi - \pi$) distance of the 2D COF crystal is ≈0.4 nm. In contrast, the *intra-layer* (i.e. in-plane) lattice constant, a, is on the order of

rectangular lattice   **hexagonal lattice**
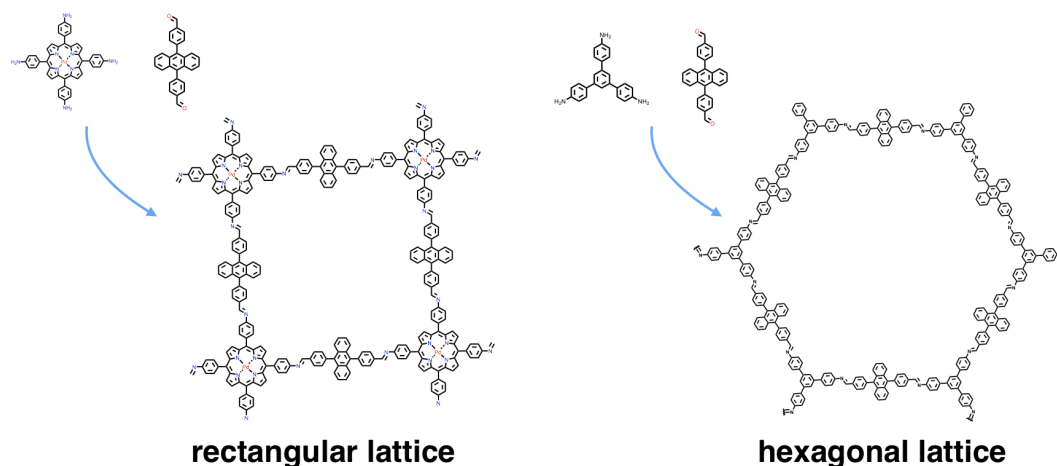
Figure 2.5: Symmetry of the COF node sets the symmetry of the lattice.
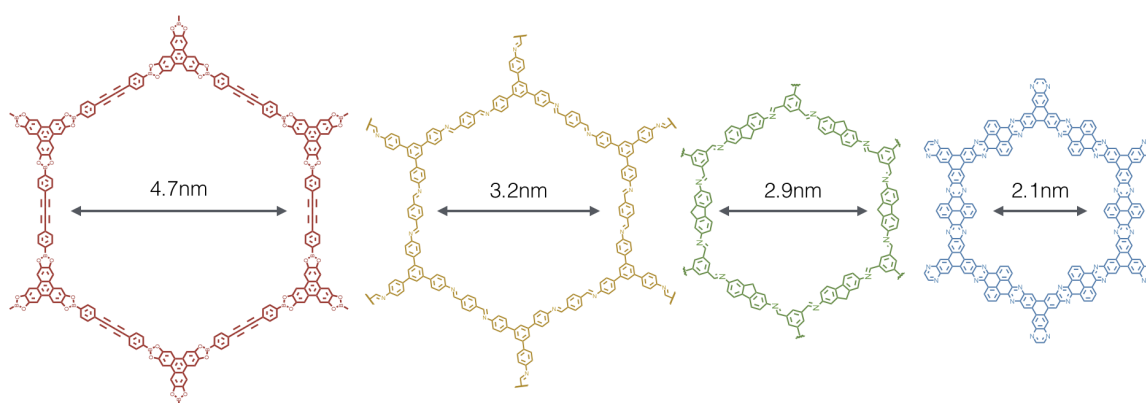
Figure 2.6: The framework lattice constant is set through choice of the linker.

4 nm. In the momentum picture, the in-plane E-k dispersion bandwidth will necessarily be far narrower than the bandwidth in the direction of the van der Waals stacking.

There are two interesting results from this. First, one might expect that the coupling of 2D COFs to their local dielectric environment can lead to dramatic modifications of the electronic structure. Engineering the dielectric environment of 2D materials is a rich area of researc [11, 12], and an area to which 2D COFs might be particularly well-suited to contribute. Second, the electronic structure of the in-plane lattice momentum will necessarily appear to have narrow energy bandwidths with high effective charge carrier masses. While this will correspond, on the one hand, to limited delocalization of the π-electrons, on the other, in specific symmetries, the large lattice constant can permit strongly correlated electronic behavior to remain robust under temperature or disorder perturbations.

2.4 Particles in a very large box: the intermolecular bond

A parameter whose import cannot be overstated is the choice of intermolecular atomic bond. The most often synthetic routes in the condensation[1] of the 2D COF crystal are (i) C=N (imine, hydrazone, and squaraine) (ii) B-O (boronate ester, and boroxine), (iii) Aromatic C=N (triazine, phenazine), (iv) C=C (alkene), (v) C–N (amide, imide, β-ketoenamine), and (vi) B=N (borazine) [13]. While each has unique synthetic conditions under which the bond can form, we will focus in this text on the C=N, C–N, and B-O bonds, respectively.

Like inorganic crystals, the path an electron traverses as two atoms approach is set by the hybridization of the electronic wavefunction. We develop an intuitive understanding of

boronate-ester bond   **imine bond**

insulating 2D COFs   semiconducting 2D COFs
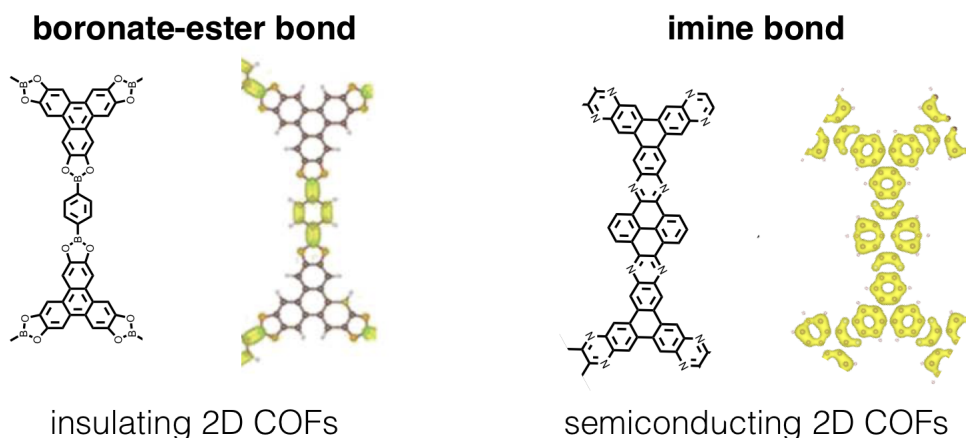
Figure 2.7: COF bonds: The extent of electronic delocalization is dratmatically modified by the selection of intermolecular atomic bond.

this through an example of the role the intermolecular bond plays in the electronic structure of the COF lattice. In Figure 2.7, we show the same node molecule (triphenylene) linked through two different linker-bonding mechanisms: the boronate ester (B–O) and the imine (C=N). On the left, the boronate ester bond (B–O) is formed through the covalent exchange at the oxygen-boron interface between the phenyl and triphenylene moities. The chemical strucutre is shown on the left and the frontier molecular orbitals (yellow) of the COF lattice valence band on the right. The valence band wavefunctions of the π-electrons are heavily localized on the phenyl ring forming the linker of the COF lattice.

On the right we show the same triphenylene node molecule now with a pyrene linker forming an imine (C=N) bond at the intermolecular interface. (Figure 2.7, right) While the charged endgroups of the B–O linker restricted frontier electron wavefunction delocalization,

---

[1]Condensation reaction: In synthetic chemistry, the term *condensation* is used to describe the reaction in which two (or more) molecules combine to form a larger molecule and a smaller byproduct molecule, such as H_2O. A definition perhaps of use to those reading this text from a physicist's perspective.

the covalent bond set by the C=N atomic link permits long-range electronic delocalization across the entire unit cell backbone of the COF lattice.

Recall now our discussion of aromatic compounds in section 1.3. To design the elctronic properties, here again one can use the simple "particle-in-a-box" picture to anticipate, for example, the bandgap of the boronate ester linked COFs will necessarily be larger than that of the imine linked COF, for the same constituent molecules. To develop specific mechanical properties, one will note that the boronate ester and imine bond have different bonding energies and solvation conditions, leading the B–O to dissolve under aqueous conditions but retain a higher degree of crystallinity due to the steric structure of the bond. What at first appears to be the difference of a few atoms in a crystal of many, the variation in intermolecular bond can have profound consequences to the optical, electronic, mechanical, and even thermal properties of the resulting 2D COF material.

Chapter 3

Control of Intermolecular Electron Dynamics in 2D Covalent Organic Framework Films

> It's hard to define the word *form*, but I wanted to make work that was multidimensional and that went back and forth in space yet remained what it was: a small, concentrated area that was essentially flat.
>
> Vija Celmins

3.1 Introduction

Formation of functional, crystalline, two-dimensional framework films is central to both the study of their intrinsic physical properties. However, the field of covalent organic framework research emerged, initially, with a focus on porous material synthesis for applications spanning gas adsorption to aquatic filtration and research largely focused on synthesis of microcrystalline COF powders and pressed pellet devices. In contrast, research in the past few years has made great strides on developing synthetic routes amenable to form two-dimensional COFs as thin films [14, 15, 16]. Central to this work – and the focus of the present chapter – is research on the synthesis of free-standing crystalline films and the development of techniques for its post-synthetic fabrication, manipulation, and chemical functionalization.

3.2 Ideas in reversible synthesis

Two conceptual strategies are useful when considering the growth of crystalline, oriented two-dimensional covalent organic frameworks [17]. First, one could take a *kinetic* approach,

where the constituent building blocks are first positioned into a maximally organized lattice
and subsequently frozen into place through an irreversible polymerization process. The
kinetic approach can make use of templating, surface-assisted effects, and polymerization
techniques actuated through changes in local charge concentrations (such as pH) or through
photopolymerization. An alternative approach would be to form covalent bonds from the
start, but under dynamic and reversible conditions. In this appoach, we search for a local
thermodynamic minima where, using reversible covalent bonds, monomer assembly can form
oriented and periodic lattices of large domain.

   We will use the latter approach, leveraging the reversibility of an imine bond formed
under acid-catalyzed condensation . In an imine condensation, the building block molecules
are synthesized with amine and aldehyde end groups, respectively. Under reaction conditions,
the NH_2 and O combine to release a molecule of H_2O and form a covalent bond (Figure 3.1).
Under aqueous acid-catalyzed conditions, this process continues towards a thermodynamic
minima and is reversible but energetically favors the crystalline system.
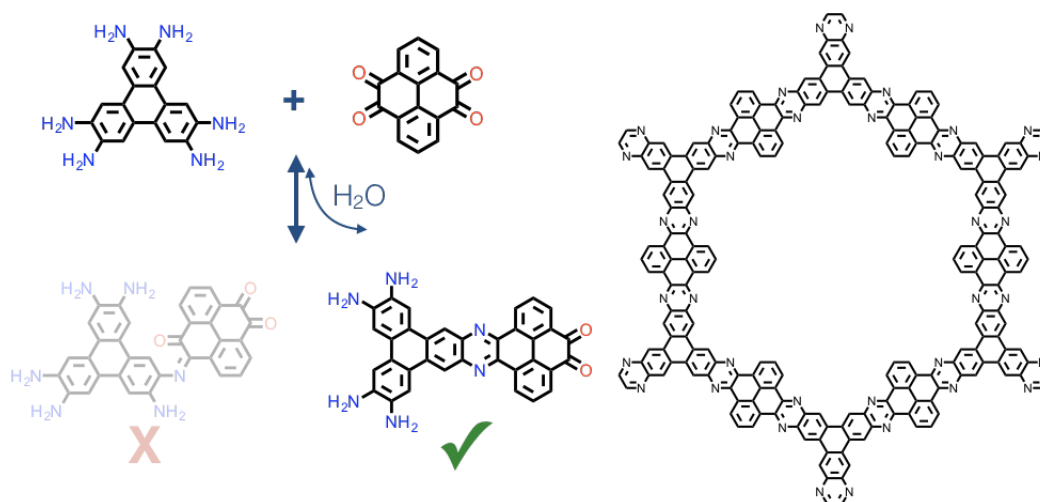
Figure 3.1: Illustration of the formation of a covalent bond through a reversible imine condensation.

   Under solvothermal conditions, this reaction will form microcrystalline powders of covalent organic frameworks. As discussed in the later, under substrate supported conditions,
solvothermal synthesis of imine-conjugated frameworks can form oriented, and crystalline
sheets [14, 18, 19, 20]. In contrast to substrate-supported films, the synthetic community has
expended substantial effort to develop free-standing films through *interfacial polymerization*.
Approaches have ranged from traditional Langmuir-Blodgett conditions to air-water and
liquid-liquid interfaces where the polymerization itself is restricted to the two-dimensional
interface [21, 22, 23, 24, 25]. In the effort to make atomically thin two dimensional frameworks, polymerization at interfaces is a compelling approach for it can form homogeneous
films that extend over arbitrarily large areas.

3.3   Interfacial polymerization of films

As illustrated in Figure 3.2 (left), we form the imine-linked covalent organic framework from an amine- and aldehyde-terminated starting monomers that form a node-linker pair. In principle, any node-linker pair can work. Here, we use 1,3,5- tris(4-aminophenyl)benzene (TAPB) and terephthalaldehyde (PDA) monomer constituents. The starting molecules are loaded into a reaction vial containing an organic solution formed of 12.5 mM TAPB and PDA 18.8 mM in 1,4-dioxane/mesitylene (4:1 v/v, 1 mL). Aqueous scandium-triflate ($Sc(OTf)_3$), a Lewis acid catalyst, at 0.001 equivalence per amine link is then added to the bottom of the reaction vial, forming an liquid-liquid interface of water and oil [26]. The thickness of the
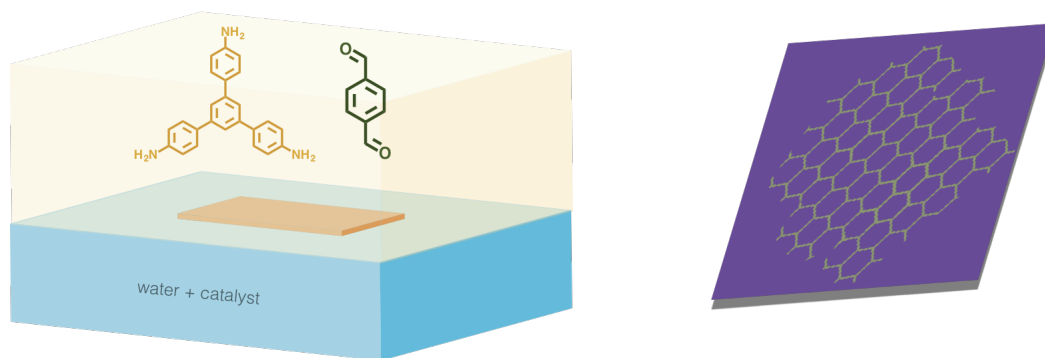
Figure 3.2: A schematic of interfacial polymerization.

resulting interfacial polymerization can be tuned through the monomer concentration and reaction time: synthesis for 5 minutes results in <4 nm thin films while synthesis at higher concentrations for 30 minutes results in films as thick as ≈ 1 μm. The interfacial film can then be scooped onto an arbitrary substrate (e.g. SiO_2, Si, Al_2O_3, fused silica, etc.), rinsed with IPA, and dried under supercritical CO_2 exchange (critical point drying).

We find that drying under supercritical CO_2 is critical for the preservation of the COF structure. Unlike traditional inorganic films, covalent organic frameworks are formed at very low density and can be considered crystalline porous polymers. Under standard growth techniques, the framework film is saturated with water and solvents in the reaction solution. Water has a high surface tension in air. Upon film extraction under ambient conditions, the liquid will rapidly evaporate from the film and in the process exert a large tangential force from the release of surface tension as the liquid converts from the liquid to gaseous state.

In the pressure-temperature phase diagram, the critical point describes the pressure-temperature coordinate at which the physical characteristics of liquids and gases are indistinguishable. As a result, systems at their critical point can convert between liquid and gaseous

SEM   Optical micrograph
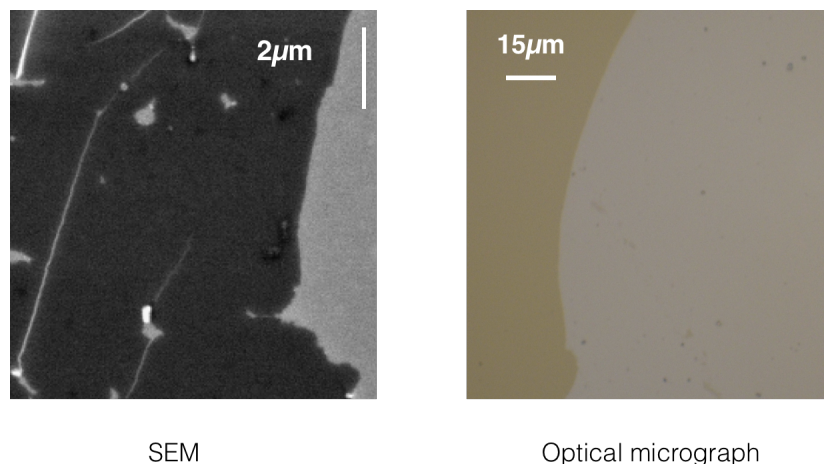
Figure 3.3: Scanning electron micrograph and optical micrograph of TAPB-PDA COF film
grown under interfacial polymerization.

phases without crossing the interface between liquid and gas states. While the critical point
of water is at $374°C/220$ bar, liquid CO_2 has a critical point at $31°C/74$ bar, and is amenable
to most sample conditions.

To dry films under supercritical CO_2, we maintain the film (substrate supported if
ultrathin or free-standing if grown to thick film form) under a solution environment of ultra-
pure IPA. Sample is then placed into a small case made of woven cotton and saturated in
ultra-pure IPA. We find it important to maintain the solution environment throughout the
preparation process to retain the crystallinity (porosity) as-grown. The cotton case is placed
into the critical point drying chamber and filled again with ultra-pure IPA, which we find to
be the best solvent for CO_2 exchange. After critical point drying, the sample can be removed
from the case and handled as normal for subsequent characterization and measurement.

3.4 Probing electronic transitions to lattice structure with broadband spectroscopy

As with any new synthetic approach, it is necessary to confirm the formation of the an-
ticipated electronic bonding and morphological structure. Optical spectroscopy provides a
robust tool set to do so. In the following sections, we will use wavelengths spanning X-rays
to the infrared to resolve the organization of the molecular lattice, detect the new electronic
transitions formed of the extended delocalization of electronic wavefunctions across the pe-
riodic lattice, and probe the intermolecular bonding through intrinisc vibrational modes.

Vibrational spectroscopy of bond formation

To characterize and verify the synthetic formation of covalent imine bonds, we use Fourier transform infrared spectroscopy (FTIR) to observe the changes in the vibrational modes based on the intermolecular bonding. The low energy of the far-infrared excites the vibrational modes of the lattice. Like weights on a spring, the atomic species that comprises the $-NH_2$, $-C=O$, O-H, and $-C=N-$, bonds all have slightly different intrinsic vibrational modes.
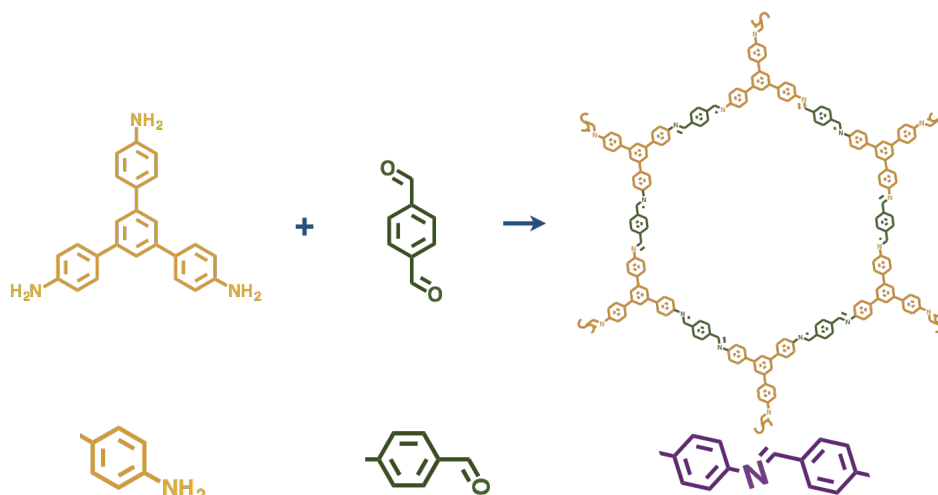
Figure 3.4: Illustration of chemical bonds that change during synthesis and which are probed under FTIR spectroscopy.

Figure 3.4 illustrates the end-group atomic bonds that change during the synthesis of the imine COF. In Figure 3.5, we plot their corresponding FTIR spectra. The aldehyde $-C=O$ bond exhibits a strong mode at 1690 cm^{-1}, as seen in the green trace in Figure 3.5 and highlighted with a green dashed line. The characteristic mode of the amine bond is due to the stretching of the N-H atoms the the range 3300-3500 cm^{-1} (yellow). We observe these characteristic resonances in the starting monomers. We can then look at the imine COF film (purple). In this spectra, the vibrational modes corresponding to the amine and aldehyde groups are replaced by the characteristic vibrational resonance mode of the imine covalent bond, which is that of the C=N imine stretch (1622cm^{-1}). Notably, no residual aldehyde signal remains, which suggests a high efficiency of conversion to the imine bond.

Electronic signatures of conjugation

We can subsequently examine how the formation of the covalent bond and the formation of a periodic lattice modifies the available electronic states of the system through optical
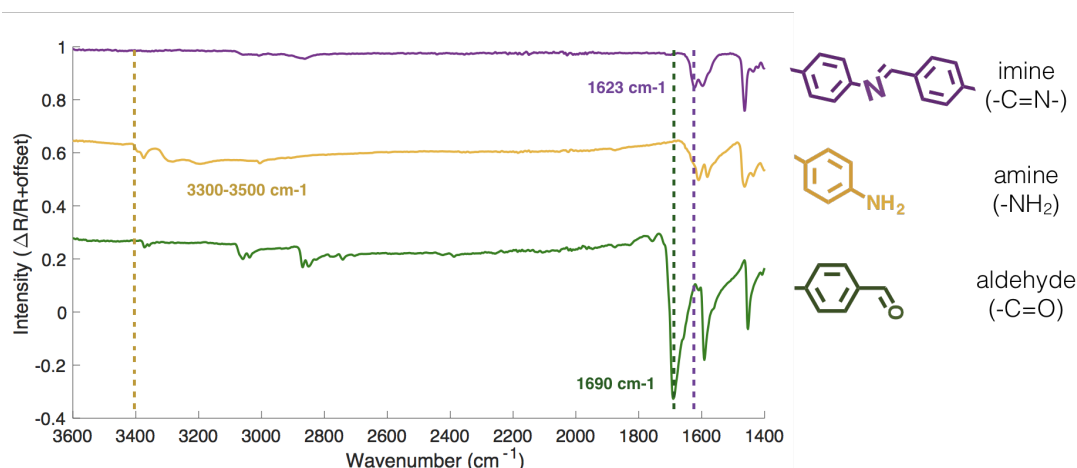
Figure 3.5: FTIR spectra of the constituent monomer and imine bond vibrational modes.

absorption spectroscopy. In Figure 3.6, we plot the absorbance of the two starting monomers in yellow and orange, respectively. These show strong resonances in the UV regime as one would expect of a small conjugated molecule. In contrast, the absorption spectra of the COF film, shown in light green, shows the emergence of a completely new absorption peak at ≈400nm, in addition to a strong resonance at the absorption of the node linker. This new resonance appears at lower energy than that of its constituent monomers and may be attributed to the emergence of extended delocalization of the π-electrons in the COF film.

One might ask, however, whether this new resonance is indeed due to the new conjugated system, and to what extent it is affected by the lattice itself. The dimer is composed of the node molecule (TAPB) capped singly by the linker, to form a macromolecular structure that retains the conjugated bonding but does not retain the periodic lattice of the framework film. One estimation of electronic delocalization is in the comparison of the *dimer* spectra (teal) to that of the complete lattice (light green). Here, we observe first that the new resonance indeed appears at the initial formation of the imine covalent bond in the dimer. Under formation of the framework, this resonance of the covalent system undergoes a redshift by several hundred meV. As we described in the introduction to COFs, we are observing the effective lengthening of the quantum well in the particle-in-a-box analogy: with longer range delocalization permitted by the formation of the COF ring, we observe a decrease in the electronic energy states in the form of a redshift of the absorption resonance. In doing so, we demonstrate that through choice of constituent monomers and linkage chemistry, we can obtain new electronic and optical properties in free-standing films of arbitrary area.
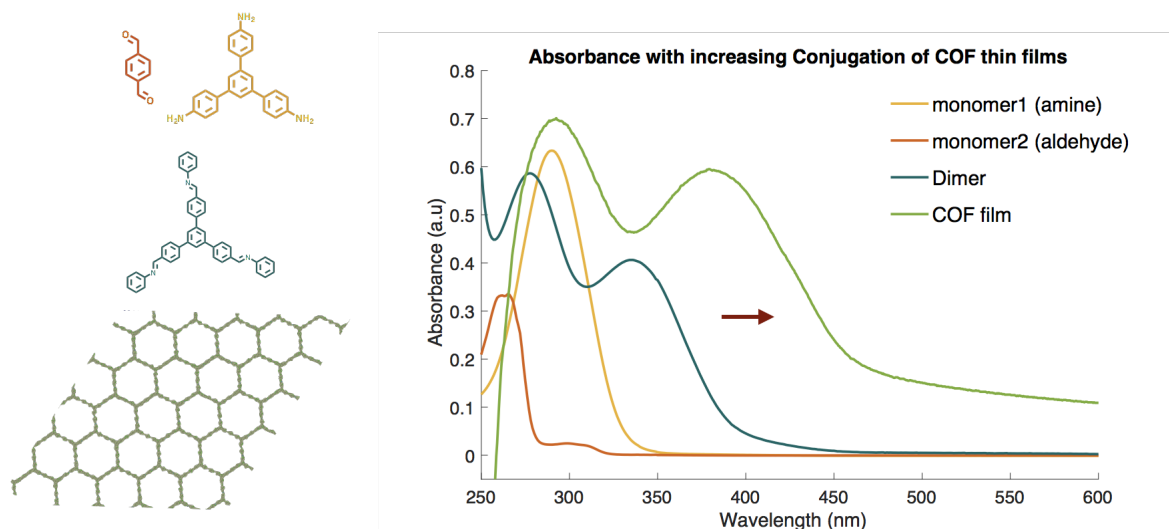
Figure 3.6: Optical absorption of interfacially-grown imine COF film exhibits lower energy absorption compared with monomer precursors.

3.5   Functionalization

Up to this point, we have largely focused on the optical and electronic COF properties and the design principles therein. We hav focused our attention on the tunability and versatility of chemical linkages, moities, and bond-types, which is one of the largest challenges in the synthetic community. However, the scope of the emergent electronic dynamics we are able to explore is limited by the requirement that the bonds be reversible. It is generally understood that less reversible linkages provide a chemical *stability* that is highly desirable in specific applications. For these kinds of applications, it may be desirable to form crystalline covalent organic frameworks that are bound by irreversible bonds. One approach to this problem is to take a leaf from the *kinetic* approach to COF formation and separate the process of forming the crystalline lattice from the formation of irreversible bonds. In doing so, we can affect an irreversible COF film, synthesized under flexible and scalable processes but robust under harsh chemical and physical conditions. The example we'll look at here is that of a post-synthetic modification of our imine bond to an aromatic polyamide, sometimes better known in its commercial form: Kevlar. Best known for its high tensile-strength-to-weight ratio, Kevlar is found in applications spanning aerospace, rigging, ballistcis, and high performance composites. At the molecular level though, Kevlar is an aromatic polyamide, comprised of aromatic amide chains held together through inter-chain hydrogen bonding(Figure 3.7). Here, we set out to develop a 2D polyamide, and to understand the subsequent mechanical, thermal, and optical properties of this system. To develop a 2D polyamide, we began with the imine-linked TAPB-PDA framework described above. Once the interfacially-grown imine-
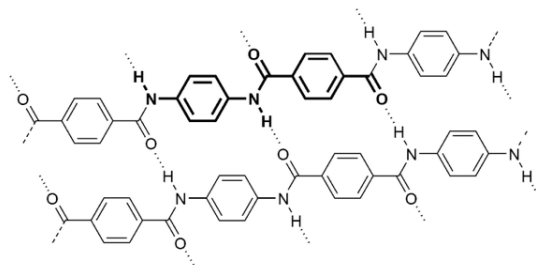
Figure 3.7: Chemical structure of linear Kevlar [27].
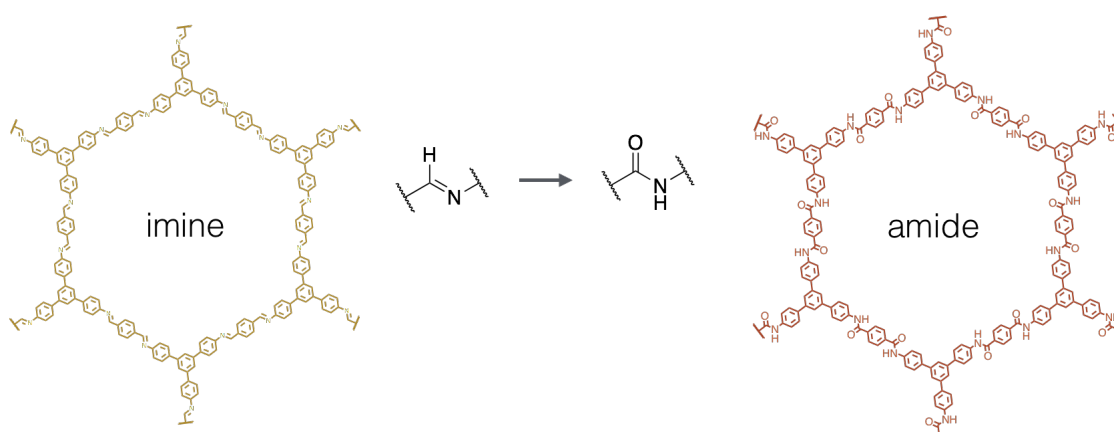
Figure 3.8: Conversion of an imine-linked framework to an amide-linked framework.

film was formed, we transferred it to float on an oxidizing bath, which converts the imine linkages to amide linkeges *in situ* [28]. The fully oxidized films can then be washed, dried, and transferred according to the methods described above.
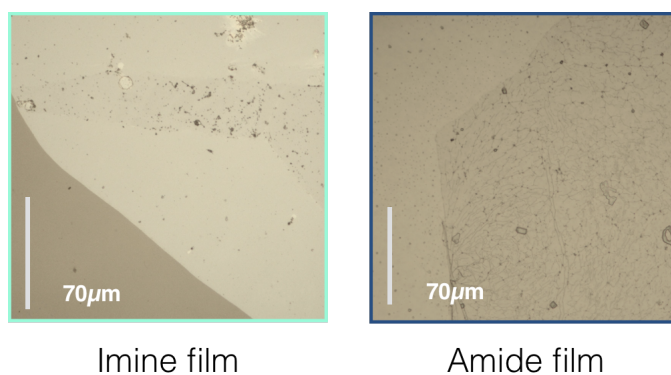
Figure 3.9: Optical micrograph of imine and amide films, both from the same imine film synthesis. Amide film subject to post-synthetic modification.

We confirm the crystallity of the imine and amide films with X-ray diffraction, and optical absorption. First, we observe the conversion of imine to amide linkers renders the film nearly completely transparent on glass substrate(Figure 3.9). In FTIR spectroscopy, we observe the spectrum of the imine (1622 cm^{-1} C=N stretch) is fully replaced by the amide signal (1651 cm^{-1} C=O) (Figure 3.10). We again see complete conversion of the imine bond to amide bonds. Under optical absorption, we observe a striking change in both
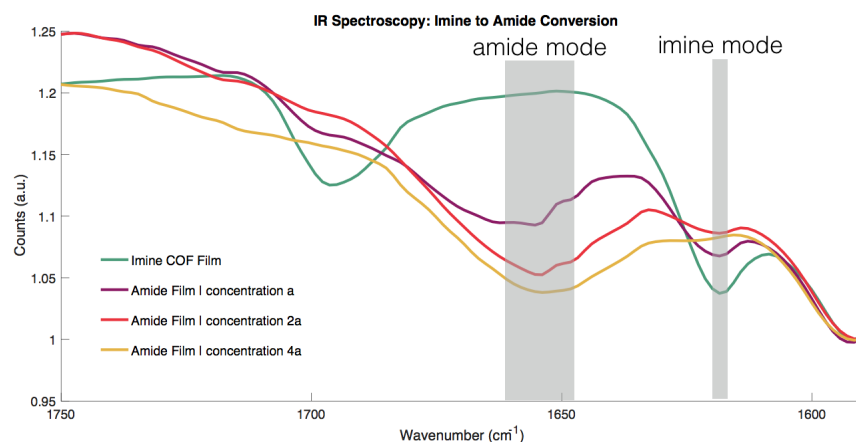
Figure 3.10: FTIR spectroscopy of the imine to amide conversion as a function of increased amidation.

absorption peaks and lineshape (Figure 3.11). The new absorption peak formed through the
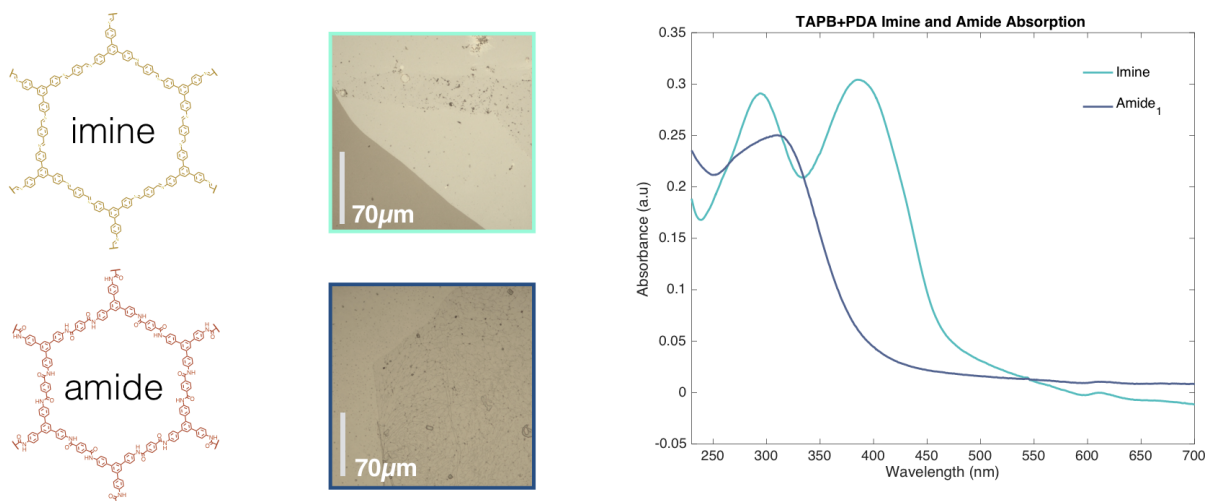
Figure 3.11: Absorption spectrum of the imine and amide films from the same imine synthesis. Amide film subject to post-synthetic modification.

covalent conjugation of the COF lattice in the imine COF completely disappears, reflecting the confinement of the electronic wavefunction under amidation.

3.6 Conclusion

Leveraging the flexibility of synthetic chemistry and broadband optical spectroscopy, we have designed and demonstrated a set of free-standing conjugated films whose optical resonances reflect the extended lattice formed in the two-dimensional covalent organic framework. In addition, we present an approach to convert materials grown under flexible and scalable imine chemistry to materials robust under extreme chemical and physical environments.

Chapter 4

Emerging Ultrafast Electron Dynamics in 2D Covalent Organic Framework van der Waals Heterostructures

> Well, if you take material you like and you know how far you can take it from what is traditional to do . . . you like to take it another step. And if it teaches you some geometry . . . you find that you can go from two dimension to three dimension, that interests me.
>
> Ruth Asawa

4.1 Introduction

The strong electronic interactions between adjacent two-dimensional layers give rise to many compelling quantum phenomena in van der Waals heterostructures observed both as emergent strong layer dependent properties in homo-multilayers and also in coupled quantum dynamics in hetero-bilayer and multilayers. For example, semiconducting transition metal dichalcogenides (TMDCs) exhibit an indirect to direct bandgap transition when thinned down to a monolayer due to momentum-dependent interlayer coupling, while hetero-bilayers of TMDCs have shown ultrafast charge transfer between layers [29, 30, 31, 32], exceptionally long spin and valley polarization lifetimes [33, 34], and emerging exciton physics in Moiré superlattices [35, 36]. Layered organic semiconductors, such as two-dimensional covalent organic frameworks (COFs), can offer exciting new opportunities for studies of low dimensional physics in van der Waals heterostructures, because the COF electronic bandstructure can be rationally tailored via choice of constituent molecules and linkage chemistry [37, 17]. With emergent properties intimately tied to the electronic states at the heterostructure in-

terface, the ability to tune the bandgap of COF in hybrid organic-inorganic van der Waals heterostructures would enable the design and realization of novel quantum phenomena across extended length scales and with molecular precision.

Current research on 2D COFs has focused on the development of powerful new synthetic techniques that extend electronic conjugation [38, 39, 40, 41, 42], promote crystallinity [14, 43, 44], and scale across moieties [10, 17]. Experimental investigation of layer-layer coupling effects between different COF layers and between COF-inorganic 2D layers has been lacking due to the large bandgap and low crystallinity of most existing COF materials.

Here, we report the first study of layer dependent optical properties in a new low-bandgap and crystalline COF and report the observation of unusual energy transfer between the coupled COF and inorganic MoS_2 monolayers in a COF/TMDC heterostructure. We rationally design a semiconducting thienoisoindigo-pyrene (TIIP) COF with a low bandgap comparable to that of TMDC semiconductors. We use solvothermal synthesis to form highly crystalline TIIP COF films on monolayer MoS_2 and use micro-exfoliation to realize ultra-thin TIIP COF/MoS_2 heterostructures. We reveal surprising layer-dependent photophysics in the TIIP COF, where photoluminescence efficiency of TIIP is dramatically enhanced in ultra-thin sheets, reminiscent of inorganic TMDC layers. In addition, we observe ultrafast charge transfer dynamics between the MoS_2 monolayer and TIIP COF, which again changes dramatically for in ultrathin TIIP COF films. These results suggest that the interlayer coupling in 2D covalent organic frameworks has a profound effect on the evolution of the excited state, permits unique and specific tuning of the excited state dynamics in 2D COF/TMDC heterostructures, and offers new opportunities to design novel quantum phenomena at the organic/inorganic interface.

4.2 Conceptual design of a low bandgap 2D covalent organic framework

To achieve a low-bandgap COF with bandgap comparable to inorganic TMDC semiconductors, we designed a new 2D van der Waals stacked thienoisoindigo-pyrene (TIIP) COF with the two-fold symmetric pyrene as a node molecule linked by thienoisoindigo ([45, 46, 47]). The illustration of the unit cell of the 2D TIIP COF in Figure 4.1 shows the two-fold symmetry of the lattice set by the pyrene node covalently bound to thienoisoindigo through imine bonds. The 2D COF forms a rhombohedral lattice with ≈ 2.9 nm lattice constant.

The bulk TIIP crystal is built up of van der Waals bonded layers of the covalently bound 2D lattice. The charge density in TIIP COF is predicted to be delocalized across the unit cell (Figure 4.2) and the electronic structure (Figure 4.3) suggests the TIIP COF is a semiconductor in its bulk form with an indirect bandgap of about 1.4 eV. Notably, in contrast to inorganic van der Waals materials like the TMDCs, the interlayer $(\pi - \pi)$ distance is nearly an order of magnitude smaller than the intralayer lattice constant of 2D COFs. This strongly enhances the importance of interlayer coupling compared to that of
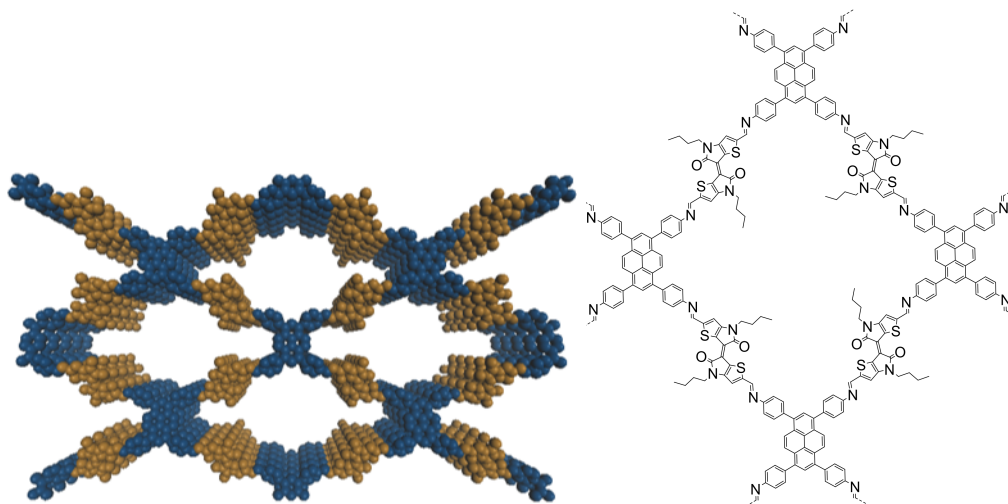
Figure 4.1: Illustration of the thienoisoindigo-pyrene (TIIP) COF and the corresponding chemical structure.

intralayer coupling in organic COF materials.
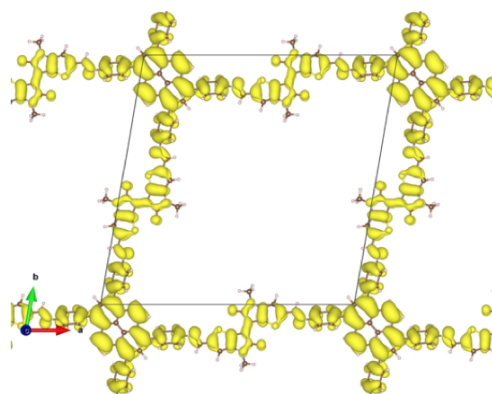
Figure 4.2: Charge density distribution in the valence band maximum of the TIIP COF.

4.3   Synthesis

Two outstanding challenges to the formation of semiconducting 2D COF films have been the solubility of low-bandgap monomers and the control of electronic delocalization across the intermolecular unit cell. We addressed the former by designing a new building block, N, N'-dibutyl-6,6'-diformylthienoisoindigo, and incorporated butyl groups along the planar core of the thienoisoindigo monomer. The latter we addressed through formyl end groups
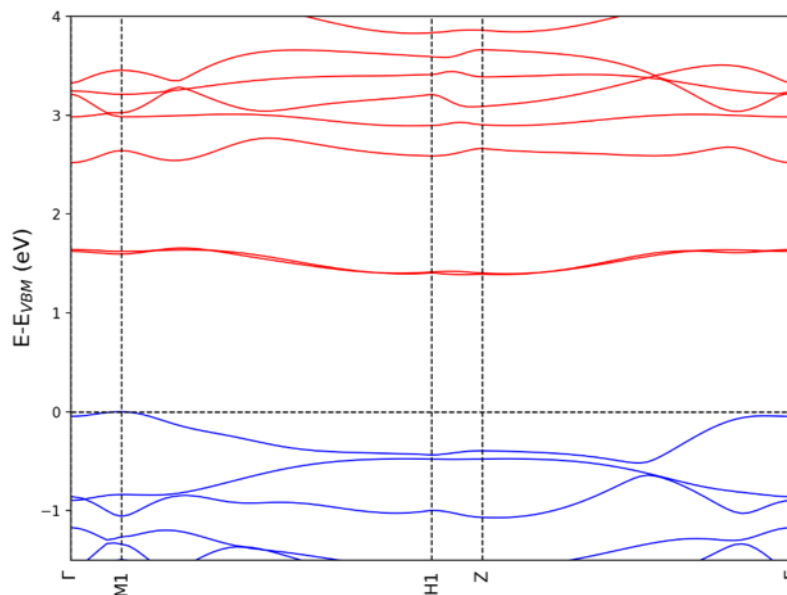
Figure 4.3: Electronic band structure of layered 2D TIIP COF.

for imine functionalization, promoting conjugation across the thienoisoindigo-pyrene bond (Figure 4.4 and [48] for monomer synthesis).
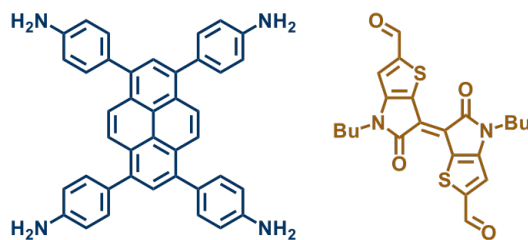
Figure 4.4: Chemical structure of the TIIP molecular monomers.

We grew highly crystalline thienoisoindigo-pyrene (TIIP) COF films through an optimized solvothermal synthesis that permits direct growth on sapphire and/or monolayer TMDCs. Film synthesis was a solvothermal direct-polymerization of 1,3,6,8-tetrakis(4-aminophenyl)pyrene and N, N'-dibutyl-6,6'-diformylthienoisoindigo in an imine condensation reaction. Following an extensive screen of solvent mixtures, we solubilized the starting monomers using a tertiary solvent blend of 5:5:2 volume o-dichlorobenzene:n-butanol:mesitylene. To promote homogenous and crystalline film growth, we minimized the formation of powder precipitates formed in the solvothermal reaction vessel. To do so, we screened for optimal imine catalyst, catalyst loading, temperatures, monomer concentration, stoichiometry, and reaction concentration. The final reaction took place in a mixture of of 2 mM TAPPy and

4 mM thienoisoindigo dialdehyde (TII-DA) with 5 vol% 9M acetic acid dissolved in the solvent blend. These reactants were then sealed, heated to 100 °C and allowed to react for 72 hours. We extracted the resulting TIIP layers and TIIP/TMDC heterostructures from the growth solution, washed, and dried under supercritical CO_2. We find that 2D TIIP COF films grow as homogeneous film on the entire family of monolayer transition metal dichalcogenides grown by both CVD and exfoliation techniques. A representative optical micrograph of TIIPCOF grown directly on CVD MoS_2 is shown in Figure 4.5 where a white triangle indicates a single crystal MoS_2.
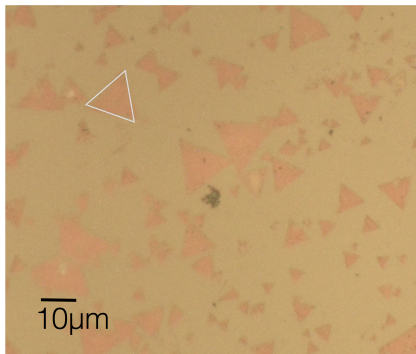
Figure 4.5: Optical micrograph of TIIP COF grown directly on MoS_2.

4.4 Structural characterization in real and momentum space

We investigated the structural properties of the TIIP COF and COF/MoS_2 heterostructures through optical microscopy, X-ray scattering, AFM, and TEM. We quantitatively confirmed the formation of TIIP COF in both real and momentum space using transmission electron microscopy (TEM) and X-ray scattering. Using film transfer methods described in Figure 4.8, the TIIP COF films can be transferred to TEM grids for direct imaging (Figure 4.6). TEM imaging directly resolves the COF lattice and the corresponding in-plane lattice spacing of ≈2.5 nm. The Fourier transform of the real space image confirms the rhombohedral symmetry of the TIIP COF lattice.

We use grazing-incidence wide angle X-ray scattering (GIWAXS) to resolve the quantitative lattice parameters and confirm the crystallinity of the periodic 2D COF structure and the orientation of the 2D van der Waals stacked sheets (Figure 4.7).

We observe diffraction peaks at 2.5 nm corresponding to the 100 scattering peak of the in-plane lattice, and at 3.4 Å along the q_z axes, corresponding to the van der Waals stacking direction. Both correspond well with the theoretically predicted values of 2.9 nm and 3.5 Å, respectively.
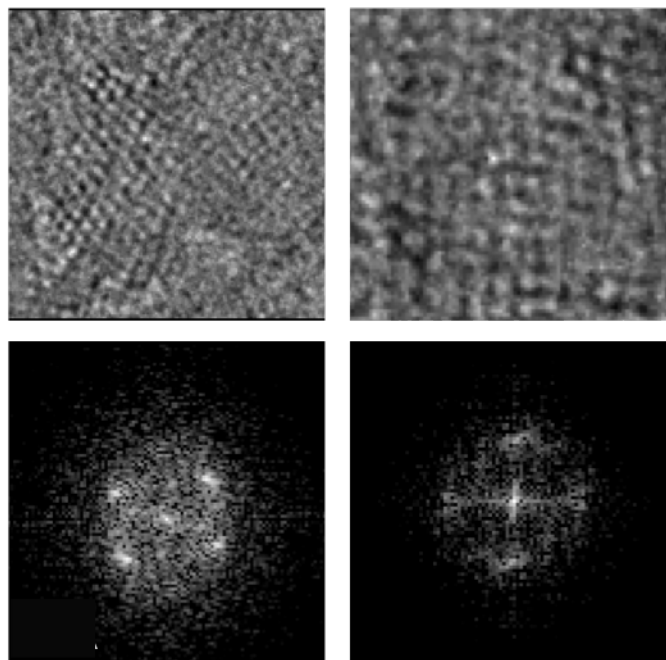
Figure 4.6: TEM images and the corresponding Fourier Transforms of the layered 2D TIIP COF.

4.5 Techniques for exfoliation and transfer

Like the semiconducting transition metal dichalcogenides, the covalently bound lattices of 2D COFS are held in vertical alignment through relatively weak van der Waals forces. When the layered crystal is oriented parallel to the substrate, covalently bound sheets can be separated by interrupting the interlayer van der Waals interactions. Extending techniques from inorganic 2D material manipulation, we developed a method of micromechanical exfoliation that permits exfoliation of TIIP COF sheets down to <2.5 nm (Figure 4.8).

As seen in illustration 1 and 2, layered 2D TIIP COF is grown directly on CVD TMDCs. Using a micro-manipulator with XYZ degrees of freedom, we place a PET stamp directly on the COF surface. The temperature of the sample stage is elevated to 60 ^{circ}C and then cooled to 45 ^{circ}C, at which point the stamp is slowly lifted in Z using a microcontroller (Thorlabs). The original substrate will have few-layer COF remaining, ranging from <2.5 nm to 10 nm in thickness (Figure 4.10). The PET stamp now has the 2D COF stack which can be transferred to arbitrary substrates and sample platforms (e.g. TEM grids). Figure 4.9 shows optical micrograph of the transferred 2D COF film.

This micromechanical manipulation enables both exfoliation of TIIP COF and also the ability to transfer sheets of TIIP COF to arbitrary substrates, devices, and other 2D
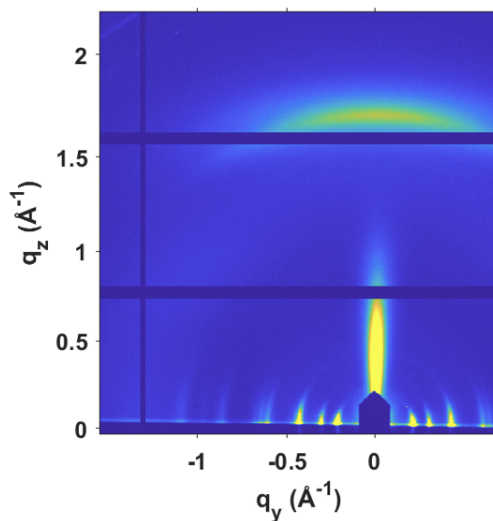
Figure 4.7: GIWAXS of TIIP COF films on monolayer MoS$_2$.
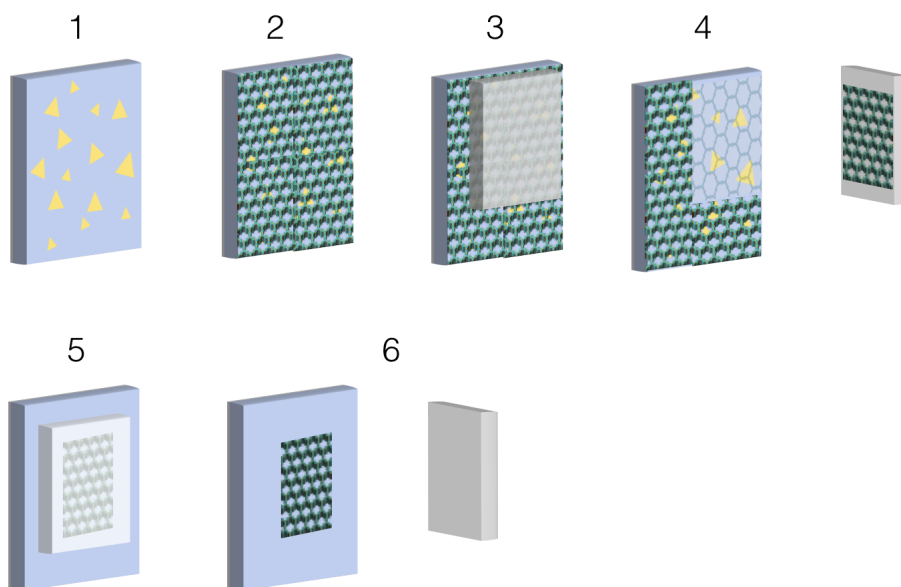
Figure 4.8: Schematic of dry-transfer pickup and exfoliation of 2D COFs.

materials. While COF exfoliation has been demonstrated through chemical exfoliation of powders [49, 50, 51, 52], with synthesis of high quality bulk crystals, mechanical exfoliation permits a completely dry-transfer process that opens opportunities to study intrinsic and device physics in 2D COFs.
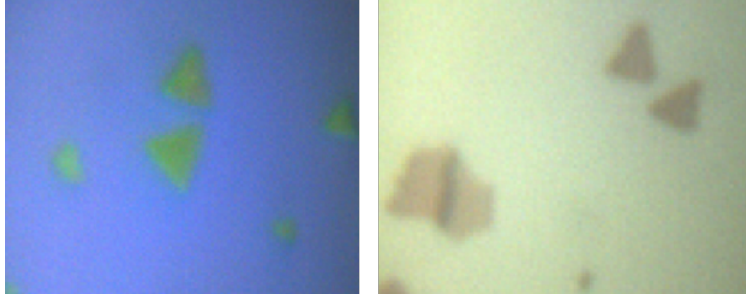
Figure 4.9: Optical micrograph of the transferred COF film on SiO_2/Si substrate.

4.6   Transport measurements

We first performed electrical transport measurements of the COF thin film using both pre-patterned bottom contacts and large-area top-contacts using standard nano fabrication techniques. We observe conductivities in the TIIP COF film of $\sigma \approx 4 \times 10^{-5}$ S/m, which is among the highest intrinsic electrical conductivities reported in 2D COFs [38, 53, 54, 55, 44](Figure 4.11). Notably, while many COF measurements have been made on pressed pellets of compressed powders, here, growth of highly crystalline films TIIP COF permits direct contact in our electrical transport measurements and opens up opportunities for facile integration into functional optoelectronic devices.

4.7   Optical spectroscopy

Figures 4.12 shows the optical absorption spectrum of the TIIP COF film. The TIIP COF film shows two broad absorption resonances at $\approx$ 1.7 eV and 1.9 eV. The lowest COF absorption is shifted by about 300 meV from that of the thienoisoindigo monomer. In the TIIP COF / MoS_2 heterostructure, we observe additional absorption resonances at 1.9 eV and 2.1 eV, corresponding to the MoS_2 A and B excitons. We note that the optical gap of MoS_2 overlaps with that of TIIP COF in the COF/MoS_2 heterostructure.

We investigate the photophysics in COF/MoS_2 heterostructures using photoluminescence (PL) spectroscopy and find a striking layer-dependence. We performed PL spectroscopy on the TIIP COF/MoS_2 heterostructures at 77 K under 2.33 eV excitation. The resulting spectra are normalized by measurement power, time, and sample thickness (Figure 4.13). As an indirect-gap material, the PL emission from bulk TIIP COF is expected to be a phonon-assisted process with low quantum yield (QY). Emission from the bulk TIIP COF indeed shows low QY. In contrast, we observe an increase in the PL efficiency measured from the few-layer COF by two orders of magnitude. In addition, we report a large blueshift in the emission energy between the bulk and few-layer COF films. In the bulk films, we observe two broad emission peaks centered at $\approx$1.4 eV and $\approx$1.6 eV that emit with low efficiency. In contrast, in the few-layer COF, we observe a single feature of $\approx$100
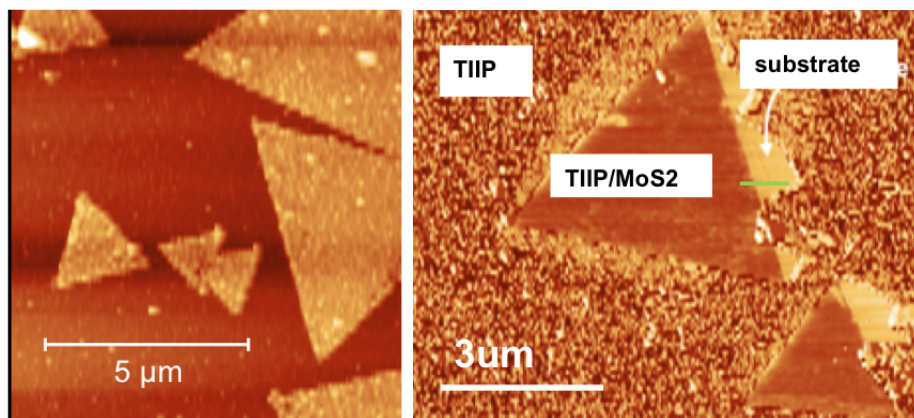
Figure 4.10: AFM of bulk and exfoliated 2D COF with topographical linescans.

meV FWHM and centered at ≈1.75 eV. While a detailed understanding of the electronic structure remains outstanding, these experimental observations propose a layer-dependence
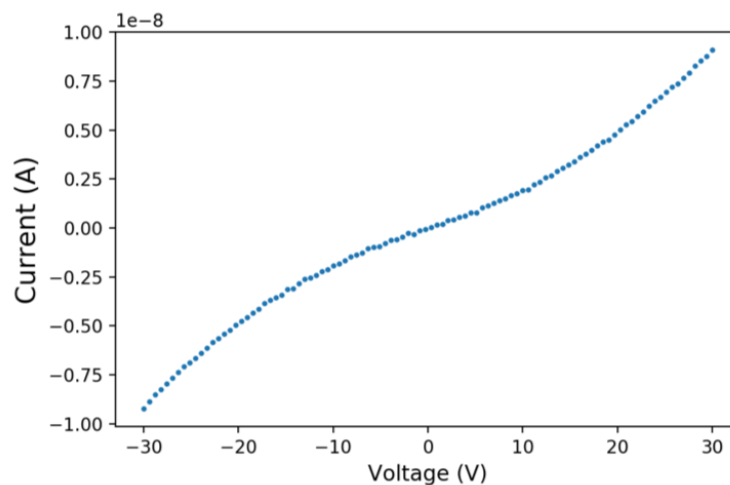
Figure 4.11: Top-contact transport of layered 2D TIIP COF.
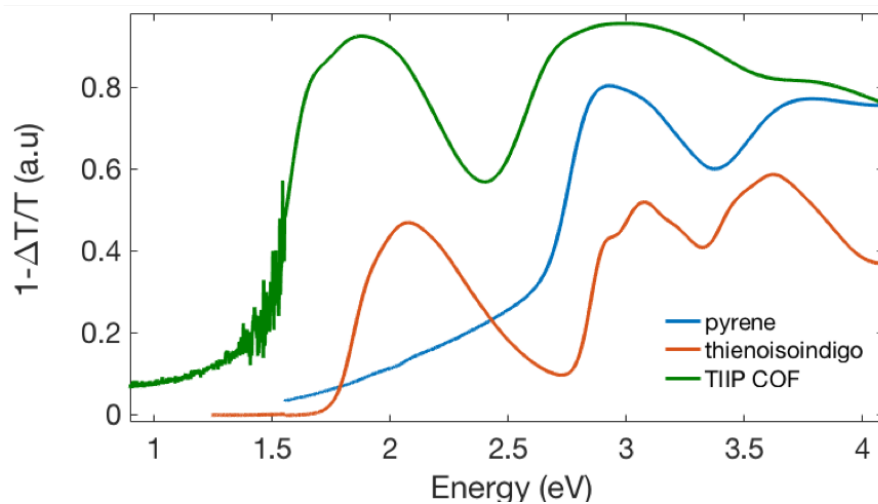
Figure 4.12: Transmittance of TIIP COF films and constituent monomers.

not previously appreciated in 2D COFs.

The observed strong enhancement in emission from the ultra-thin film is reminiscent of behavior in low dimensional inorganic semiconductors. For example, nanocrystals and nanostructures from indirect bandgap semiconductors, such as silicon, exhibit increased photoluminescence efficiency relative to the bulk and increased emission energy with decreasing crystal size as a direct consequence of the quantum confinement of electronic states [56, 57]. In semiconducting TMDCs, such as bulk MoS_2, the direct gap at ≈1.9 eV occurs at the K point of the Brillouin zone, whereas the conduction band minimum and valence band maximum are located along the Gamma-K direction and form the indirect gap. As layer
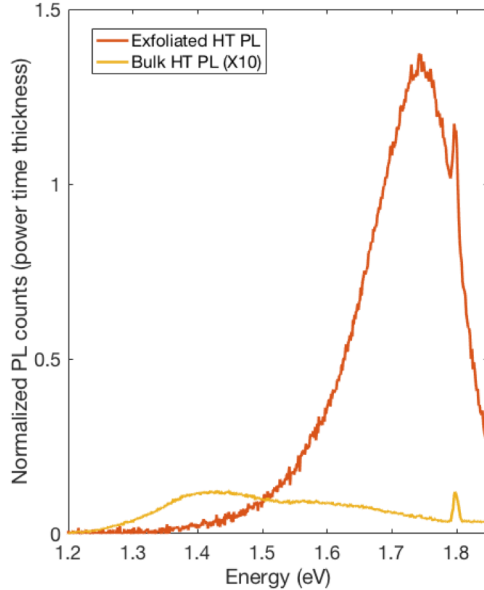
Figure 4.13: Layer-dependent photoluminescence in TIIP COF films.

number decreases in MoS2, the indirect gap exhibits a large confinement-induced increase in the transition energy [29, 30].

For TIIP COF, the valence band maximum at M1 and the conduction band minimum along the M1-H1 direction forms the indirect bandgap (Figure 4.3). Our *ab initio* electronic structure calculations estimate the hole effective mass in the bulk to be $\approx 0.4 m_0$ and with a ≈ 400 meV bandwidth around the valence band maximum in the out-of-plane direction. In contrast, the in-plane coupling seen in the H1-Z direction is an order of magnitude less dispersive, with an estimated bandwidth of only ≈ 50 meV. In contrast to the TMDCs, the TIIP COF exhibits markedly stronger interlayer electronic coupling than intralayer coupling, resulting in the strong confinement effects and the layer dependent emission seen in the data.

4.8 Emerging electron dynamics in covalent organic framework heterostructures

Next, we probe the energy transfer dynamics between the organic TIIP COF and the inorganic MoS_2 layers using photoluminescence excitation (PLE) spectroscopy. In PLE, we monitor the COF PL spectra as we sweep the excitation photon energy across the energy range spanning the MoS_2 A- and B- exciton resonances. The resulting 2D PLE spectra of ultra-thin COF/MoS_2 heterostructures exposes two bright features where the emission of the COF has been enhanced at excitation energies of ≈ 1.9 eV and ≈ 2.1 eV (Figure 4.14, left). For a more informative analysis, we integrate each emission spectra over the tail of the COF emission and normalize by the excitation energy and integration time. The integrated

linecuts exhibit two resonant features at excitation energies ≈1.9 eV and ≈2.1 eV, respectively (red trace in Figure 4.14, right). While the COF absorption is relatively flat over this regime, these energies coincide with the A- and B- exciton absorption of MoS_2 (blue trace 4.14, right). The enhancement of COF emission in response to excitation at the MoS_2 resonances provides direct evidence of an energy transfer process from MoS_2 to the TIIP COF in the TMDC/COF heterostructure.
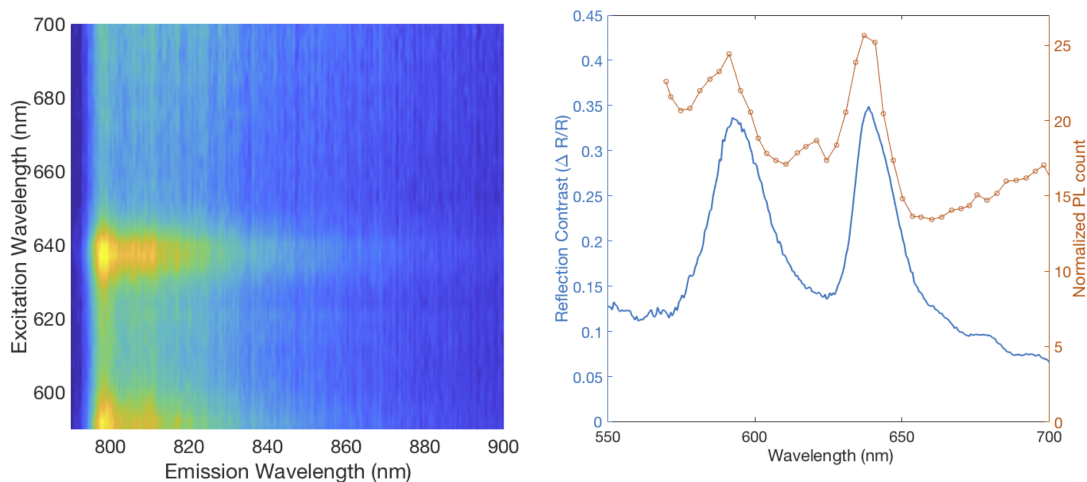
Figure 4.14: Photoluminescence excitation of the TIIP/MoS_2 heterostructure and corresponding linecuts.

We also show the PLE spectra of bulk TIIP COF alone (no MoS_2), which clearly does not show any enhancement without the heterostructure (Figure 4.15).
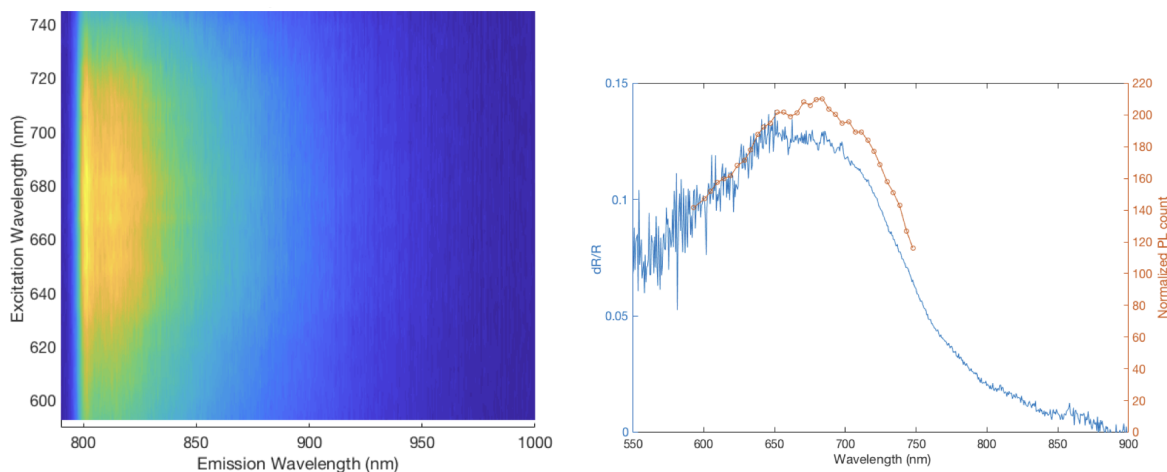
Figure 4.15: Photoluminescence excitation of bare TIIP and corresponding linecuts.

Comparison of the integrated PLE linecuts to the heterostructure absorption spectrum provides quantitative insight into the efficiency of the energy transfer process revealed through PLE spectroscopy (Figure 4.14, right). The absorption spectrum is obtained from reflection contrast measurements ($\Delta R/R$). For thin samples on transparent substrates, the reflection change is directly proportional to the change in absorption coefficient. Comparing the ratio of the A-exciton resonance of MoS_2 to the broad COF absorption background (blue trace), we observe that the MoS_2 A-exciton resonance absorption is nearly 300% of that of the COF absorption. In contrast, we observe only $\approx$60% PLE enhancement (red trace) at the MoS_2 A-exciton resonance. This comparison suggests that the energy transfer efficiency – the fraction of the optical absorption in MoS_2 that leads to TIIP COF excitation through energy transfer – is limited to about 20%.

The relative quenching of MoS_2 photoluminescence can provide an additional perspective on the energy transfer efficiency in the COF/MoS_2 heterostructure. Figure 4.16 shows the PL emission from the MoS_2 A-exciton in bare MoS_2, the ultra thin TIIP/MoS_2 heterostructure, and the bulk TIIP/MoS_2 heterostructure. In the bulk TIIP/MoS_2 heterostructure, we observe that emission from the monolayer MoS_2 A-exciton resonance (1.9 eV), prominent in isolation (green), is quenched by $\approx$85% in the heterostructure (yellow). In contrast, in the ultra thin heterostructure, the MoS_2 emission is quenched by only $\approx$15%.
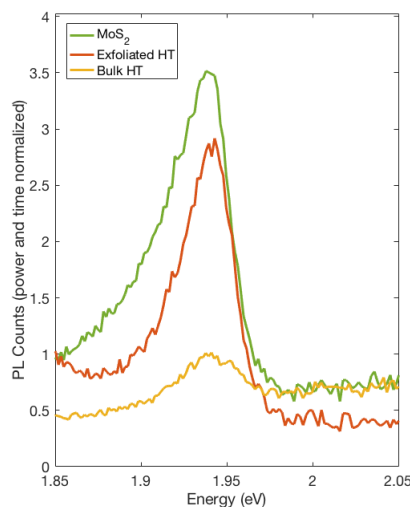
Figure 4.16: Quenching of MoS_2 photoluminescence in the COF/TMDC heterostructure.

Taken together, we can understand both the energy transfer efficiency from the PLE data and the quenching of MoS_2 emission in the context of a competition between the rate of recombination in MoS_2 and the rate of energy transfer in the heterostructure. The efficiency of luminescence is defined by the countervailing timescales of radiative (e.g. emissive) and nonradiative decay pathways (e.g. transfer). The PL efficiency in the COF/MoS_2 het-

erostructure is given by:

$$\eta = \frac{\gamma_{rad}}{\gamma_{total}} \tag{4.1}$$

where γ_{rad} is the radiative recombination rate and γ_{total} is the total recombination rate, consisting of the sum of the decay rate from MoS_2 and the energy transfer rate: $\gamma_{total} = \gamma_{MoS_2} + \gamma_{transfer}$.

In monolayer MoS_2, the total decay rate, γ_{MoS_2}, is on the order of ≈ 1 ps^{-1} [58]. In Figure 4.16, we observe that the emission from the MoS_2 in the bulk heterostructure is reduced by $\approx$7X which suggests the presence of an alternative, faster, decay pathway with a total rate

$$\gamma_{total} \approx 7\gamma_{MoS_2} \tag{4.2}$$

Thus, we can estimate

$$\gamma_{transfer} \approx 6\gamma_{MoS_2} \approx (166fs)^{-1} \tag{4.3}$$

Most dynamic processes in MoS_2 monolayers take place on the order of several to tens of picoseconds [59]. However, as reported in van der Waals heterostructures of TMDCs [31], in 2D materials with strong Coulomb interactions, ultrafast transfer processes can take place on the order of tens to hundreds of femtoseconds.

The excited state dynamics of the few-layer COF/MoS_2 heterostructure appear starkly different. In the heterostructure formed of ultrathin COF, we observe the PL from MoS_2 to be quenched by only $\approx$15%, or $\gamma_{total} \approx 1.15\gamma_{MoS_2}$, using the argument we laid out above. Again,

$$\gamma_{total} = \gamma_{MoS_2} + \gamma_{transfer} \tag{4.4}$$

but now we see that

$$\gamma_{transfer} \approx 0.15\gamma_{MoS_2} \approx (6.6ps)^{-1} \tag{4.5}$$

We compare this to the $\approx 20\%$ energy transfer efficiency that led to increased COF emission at the MoS_2 exciton resonances in our PLE data (Figure 4.14), corresponding to

$$\gamma_{transfer} \approx 0.2\gamma_{MoS_2} \approx (5ps)^{-1} \tag{4.6}$$

which agreees well with the transfer rate derived from PL quenching. With decreasing COF layers, our two independent measurements indicate that the excited state dynamics of the TIIP/MoS_2 heterostructure slows by over 30× in comparison to the bulk heterostructure. Combined, these experimental data suggest that despite having a unit cell over a magnitude larger and consisting primarily of light atoms, the heterostructure formed of TIIP COF with monolayer MoS_2 substantially modifies the dynamics of the excited states in the coupled system.

4.9 Conclusion

These results present a new perspective on optically active 2D covalent organic frameworks. Our data demonstrates that the formation of a highly crystalline and semiconducting 2D

TIIP COF permits strong layer-dependent electronic properties not previously observed in 2D covalent organic frameworks, but with dramatic consequences for optoelectronic devices. We present a new experimental platform for studying the underlying physics that can be easily extended throughout this new family of semiconducting 2D COFs and the TMDCs. We further demonstrate that from the unexpectedly strong interlayer coupling emerge new ultrafast energy transfer pathways in TIIP/MoS$_2$ heterostructures which are themselves layer-dependent. In addition to providing a platform for new optoelectronic devices, consequences of this work can be directly applied to a much broader group of van der Waals bonded solids and reveal distinctive electronic properties present in 2D COFs that enables research leveraging synthetic control of optoelectronic properties, at the scale of functional devices, with molecular precision.

Chapter 5

Future Directions

To see far is one thing, going there is another.

Constantin Brancusi

The work presented in these chapters reflect a fundamental shift in the maturity and complexity of the scientific questions we can ask in framework materials. Here, we outline directions of future research that might be both productive and fascinating.

5.1   Semiconducting 2D covalent organic frameworks

The development of semiconducting frameworks was critical to our ability to observe and modulate their optoelectronic properties. Specifically, having bandgaps of <2 eV makes electrostatic gating accessible permitting studies of transport and modulation of carrier densities. There are a couple interesting directions from here.

First, while we presented one semiconducting two dimensional covalent organic framework (TIIP COF) in Chapter 4, this was in fact one of three potential candidates we developed to study (Figure 5.1). Each framework retained the thienoisoindigo node and differed only by the linker molecule with the integraton of a phenyl and thiophene linker, respectively. We observe a striking change in the electronic band dispersion based on this molecular shift where the bandgap ranges from < 1 eV to over 2 eV and the bandwidth changes by several fold.

While Figure 5.1 demonstrates how the variation of chemical moiety along the backbone of the framework can modify the optical properties, theory also predicts a direct-to-indirect bandgap transition in the monolayer limit of the two dimensional COF films (Figure 5.2). In bulk TIIP COF, theory predicts the valence bandwidth on the order of ≈ 0.4 eV, with an effective mass of $m_h = 0.4m_0$. An indirect gap material in the bulk, the TIIP COF has a bandgap of $E_g \approx 1.4$ eV, while its direct gap is $E_g \approx 1.6$ eV. Notably, the dispersion in the out-of-plane direction of the bulk COF (M1-H1 direction) is substantially stronger
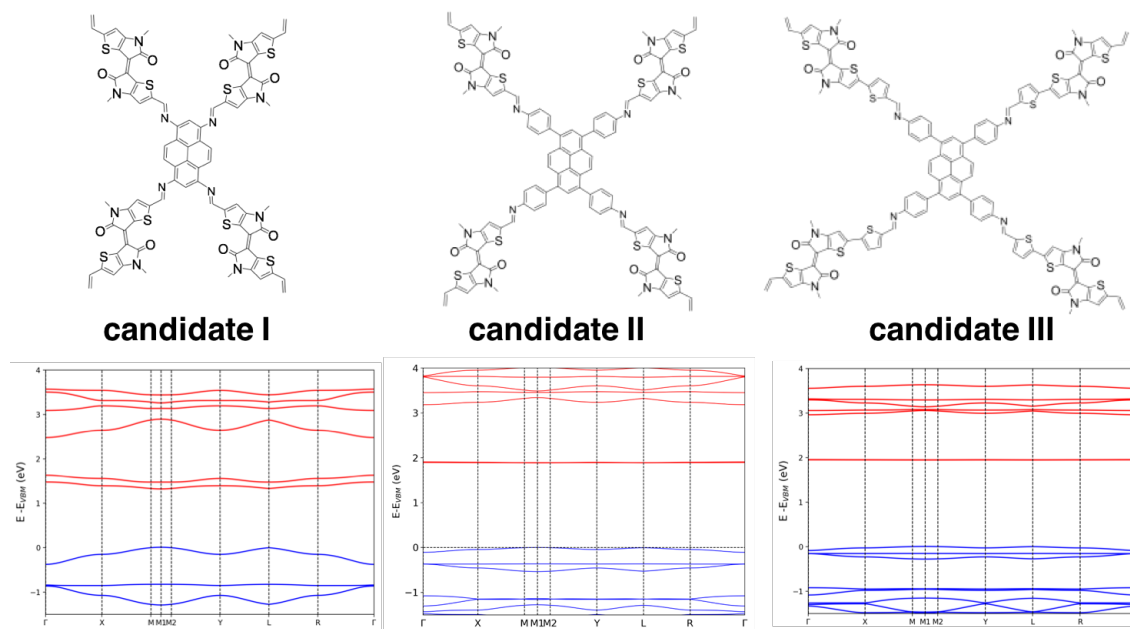
Figure 5.1: Electronic bandstructures of candidate frameworks.
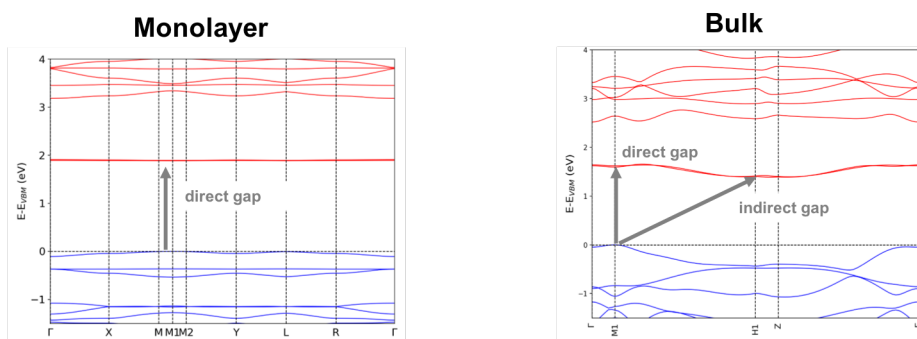
Figure 5.2: Electronic bandstructures of monolayer and bulk TIIP COF.

than the in-plane dispersion (H1-Z direction). Reminiscent of inorganic two dimensional materials, the monolayer TIIP COF is predicted to have a direct energy gap of $E_g \approx 1.8$ eV.

Another interesting direction in semiconducting 2D COFs will be the implementation of careful transport measurements to high quality films. Specifically, the strong asymmetry in the interlayer and intralayer coupling strengths suggest the possible asymmetry in their transport as well. However, care must be taken to ensure transport measurements can be interpreted meaningfully. In order to achieve this, the crystalline 2D COF films must be of nearly perfect crystallinity. Studies should take care to characterize the contact formed between the electrode and COF interface, particularly in light of the order of magnitude unit cell mismatch.

These theoretical predictions are particularly interesting in the context of the emerging photoluminescence and energy transfer dynamics we observe in bulk and ultrathin TIIP COF films in Chapter 4 and extending this work to the monolayer limit will assuredly be interesting. Moreoever, a rich body of research could be found by extending the synthetic, preparation, and characterization tools developed in this dissertation to additional semiconducting covalent organic frameworks to study the intrinsic and interfacial optical and electronic properties, charge and energy transfer, and the emergence of quantum phenomena spanning confinement effects to spin transfer and lifetimes.

5.2 Strongly correlated physics in 2D covalent organic frameworks

Superlattices at the two dimensional interface

Another direction of interest for future research is in 2D superlattice heterostructures with atomically thin materials such as graphene and the transition metal dichalcogenides. The generation of a periodic potential on a crystal lattice forms a new translational period in the periodic boundary conditions [60]. This periodic potential defines a new wave vector of
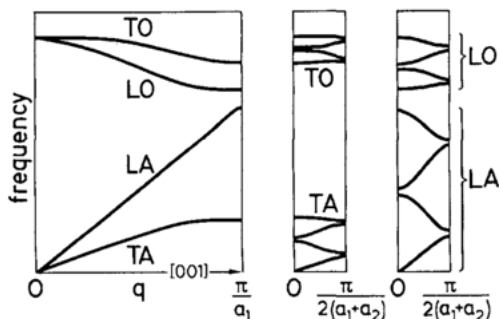
Figure 5.3: Superlattice band folding [60].

the system– the superlattice wave vector– which permits us to describe $\vec{k_{SL}}$ as a conserved quantity due to its translational invariance. In doing so, the energy bands of the Brillouin zone "fold over" and form a "reduced" Brillouin zone, termed the *superlattice Brillouin zone* (Figure 5.3). In this zone-folding scheme, new modes appear in the superlattice Brillouin zone at k=0, which can now be Raman and IR active modes probed via optical spectroscopies.

Flat bands in two dimensional COFS

As we have seen, symmetry and dimension can have a profound effect on the electronic behavior in two dimensional covalent organic frameworks. Specifically, the symmetry of a

lattice with delocalized electrons determines whether the corresponding energy bands will be strongly dispersive or be host to non-trivial flat bands [61].

For example, theory predicts that a 2n-fold symmetric node can generate significant the electronic couplings between adjacent sites, which can give rise to strongly dispersive electronic bands. This was our motivation to choose a 2-fold symmetric node to build the TIIP COF. On the other hand, frameworks built from conjugated 3-fold symmetric nodes can form a honeycomb–kagome lattice with three inequivalent sites per unit cell. In the nearest-neighbor approximation, with a single orbital at each site, the high symmetry of this system can lead to the formation of a completely flat band and two dispersive bands due, essentially, to destructive interference of the electronic wavefunctions giving rise to non-trivial wavefunction localization [62]. The consequences of flat electronic dispersion can be profound and produce strongly correlated electronic phenomena spanning the Mott insulator to superconductivity.

Flat bands emerge naturally in high symmetry two dimensional COFs. In addition, to achieve a strongly correlated system, one would like the Coulomb energy, U, of the system to be much much greater than the kinetic energy, K. In a two-dimensional crystal, $U \approx \frac{e^2}{\epsilon L}$ and $K \approx \frac{\hbar^2 k^2}{2m_e} \approx \frac{1}{m_e L^2}$. As discussed in Chapter 4, two dimensional covalent organic frameworks intrinsically have a very large lattice constant (and thus very large L) and large effective mass (also due, in part, to the very large lattice constant) making strongly correlated effects an interesting area for future study from both an experimental and theoretical perspective.

Part II

Imaging Electric Fields

Chapter 6

New Scientific Tools

> In every field of industry, new problems have presented themselves and new tools have been created capable of resolving them. If this new fact be set against the past, then you have a revolution.
>
> <div align="right">Le Corbusier</div>

6.1   Introduction

Part II will focus on the development of a new technique capable of imaging local electric fields in space and time. We will use our understanding of the interaction of light and matter in atomically thin materials and dielectric materials to convert the local electric potentials into an optical response. In doing so, we will be able to spatially resolve dynamic distributions of local electric fields across a field of view and apply this new capability to the study of dynamic biological systems in aqueous environments.

When we think of measuring the motion of an electron, we thinks of measuring current. To do so, we place a conducting wire where we expect the source of electrons to be. This results in several nontrivial requirements from an experimental point of view. First, we must know where to place the wire. Adjacent to another conducting material, for example. Second, we must be able to reasonably place a thin wire at this output of charge. What if this is quite difficult to do? Or, perhaps more interestingly, what if the transport of electrons occurs in places in we don't in fact expect? This was quite the case when ionic channels embedded in cellular membranes inside living organisms were discovered to control the transport of charge across cell membranes and regulate intercellular communication.

In the first section, I will discuss our design and development of the electric field imaging system. The sensor is based on the unique optical transitions in graphene, in which a small change in local potential at the surface of the atomically thin sheet can manifest in a dramatic modification to the light absorbed. By imaging sheet of graphene, we are able to spatially and temporally distinguish areas where the electric field above graphene is

fluctuating. To amplify this response, we couple graphene to a planar dielectric waveguide that acts much like a Fabry-Perot cavity operated under frustrated total internal reflection.

In the second section, I discuss our application of this technology to the detection of action potentials in living cells. Bioelectric phenomena is ubiquitous. Electrically active cells, like neurons, heart cells, electrically active bacteria, fungi, cellular organelles, and even membrane-enveloped viruses, dynamically vary their transmembrane potential as a result of local chemical and electrical stimuli [63]. Action potentials form the communication pathways of our nervous system and contribute to our ability to move, speak, and form memories. We are interested in opportunities to study these phenomena and, especially, phenomena not easily measured via conventional means of detection.

6.2 The atomic structure of graphene

Graphene is composed of a two-dimensional honeycomb lattice (Figure 6.1), with two in-equivalent carbon sites per unit cell, known as the A and B sites. The unit cell itself forms a rhombus with primitive lattice vectors are $\vec{a}_1 = a(1,0)$ and $\vec{a}_2 = a(-1/2, \sqrt{3}/2)$ and lattice constant $a \approx 0.246$ nm. The reciprocal lattice vectors of the first Brillouin zone are given by $\vec{b}_1 = (2\pi)(1, 1/\sqrt{3})$ and $\vec{b}_2 = (2\pi)(0, 2/\sqrt{3})$.
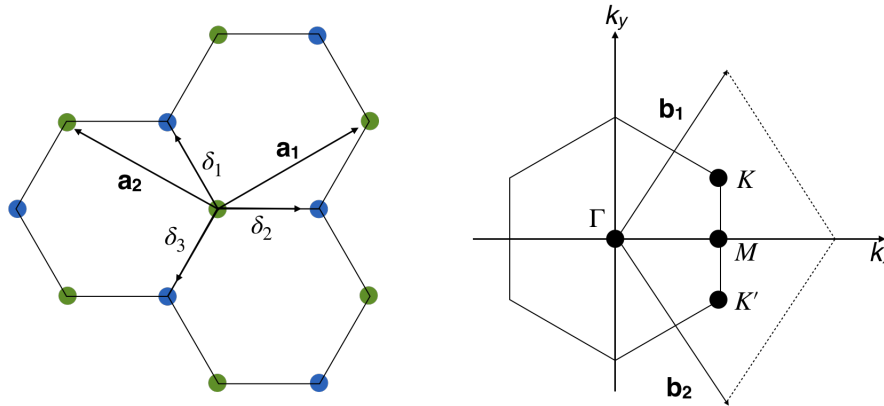
Figure 6.1: Graphene's honeycomb lattice and the first Brillouin Zone. Left: the hexagonal lattice structure of graphene is comprised of two interpenetrating triangular lattices. $\vec{a}_1$ and $\vec{a}_2$ are the lattice vectors, δ_1, δ_2, and δ_3 are the nearest-neighbor vectors. Right: First Brillouin zone with reciprocal lattice vectors $\vec{b}_1$ and $\vec{b}_2$. The Dirac cones are located at the K and K' points in the first Brillouin zone.

Each carbon atom has six electrons: two associated to its core and four outer shell electrons occupying the $2s, 2p_x, 2p_y$, and $2p_z$ orbitals. The electrons in the $2s, 2p_x$, and $2p_y$, orbitals form sp^2 hybridized orbitals giving rise to the in-plane σ bonds forming graphene's lattice. The remaining carbon $2p_z$ orbitals form covalent π-bonds and are directed perpendicular to the graphene plane[64]. As the energy levels responsible for most experimentally observable properties are those located close to the Fermi energy, and the low-energy electronic levels are determined primarily by the $2p_z$ orbitals, we can restrict our attention to the π orbitals.

6.3 The electronic structure of graphene

Tight binding approximation

The simplest description of the electronic structure of graphene can be obtained using the tight binding approximation. In 1947, P.R. Wallace extended the tight binding approximation to calculate the electronic band structure of monolayer graphene [65]. There are many additional references that use tight binding model for graphene, some of which are enumerated in references [66, 67, 68, 69]. In the tight binding approximation, we assume:

1. For an isolated atom, the energy eigenvalues and eigenfunctions of an electron are known.

2. Each electron in the solid can be assigned to an atomic site – aka 'tight binding'.

3. The periodic potential of the lattice is reasonably well approximated by a superposition of the atomic potentials.

4. The difference between the superposition of atomic potentials and the actual potential can be described as a small perturbation (and so perturbation theory applies).

The atomic wavefunction for an atom at lattice site $\vec{R}_n$ is given by $\phi(\vec{r} - \vec{R}_n)$. The Schrödinger equation for an electron associated with an isolated atom is:

$$[-\frac{\hbar^2}{2m}\nabla^2 + U(\vec{r} - \vec{R}_n) - E^0]\phi(\vec{r} - \vec{R}_n) = 0 \tag{6.1}$$

where $U(\vec{r} - \vec{R}_n)$ is the atomic potential and E^0 is the atomic eigenvalue. If atoms are brought together to form a periodic crystal described by periodic potential, $V(\vec{r})$, $\psi(\vec{r})$ and $E(\vec{k})$ correspond to the wave function and the energy eigenvalue in the crystal. We can then rewrite Equation 6.1 as:

$$[-\frac{\hbar^2}{2m}\nabla^2 + V(\vec{r}) - E]\psi(\vec{r}) = 0 \tag{6.2}$$

Under the tight binding approximation, $V(\vec{r})$ is simply a sum of atomic potentials

$$V(\vec{r}) \approx \sum_n U(\vec{r} - \vec{R}_n) \tag{6.3}$$

and the energy eigenvalues, $E((\vec{k})$ are given by

$$E(\vec{k}) = \frac{\langle \vec{k}| \mathcal{H} |\vec{k}\rangle}{\langle \vec{k}|\vec{k}\rangle} \tag{6.4}$$

The Hamiltonian in the tight binding approximation is written as

$$\mathcal{H} = \mathcal{H}_0 + \mathcal{H}' = -\frac{\hbar^2}{2m}\nabla^2 + V(\vec{r}) \tag{6.5}$$

for which $\mathcal{H}_0$ provides the Hamiltonian for the atomic site, n

$$\mathcal{H}_0 = -\frac{\hbar^2}{2m}\nabla^2 + U(\vec{r} - \vec{R_n}) \tag{6.6}$$

and $\mathcal{H}'$ is the small (perturbative) difference between the atomic potential at site n described by $\mathcal{H}_0$ and the actual periodic potential of the crystal.

$$\mathcal{H}' = V(\vec{r}) - U(\vec{r} - \vec{R_n}) \tag{6.7}$$

In graphene, with two atoms per unit cell, we choose Bloch wavefunctions on the A and B sublattices as our basis:

$$\psi_{\vec{k}} = C_A\psi_{\vec{k}}^A + C_B\psi_{\vec{k}}^B \tag{6.8}$$

Limiting hopping to nearest neighbor interactions, the Hamiltonian is given by

$$H = \begin{bmatrix} H_{AA} & H_{AB} \\ H_{BA} & H_{BB} \end{bmatrix} = \begin{bmatrix} \epsilon & -\gamma_0 f(\vec{k}) \\ -\gamma_0 f(\vec{k})^* & \epsilon \end{bmatrix} \tag{6.9}$$

$$f(\vec{k}) \equiv \sum_{j=1,2,3} e^{i\vec{k}\cdot\delta_j} = e^{i\vec{k}\cdot\vec{R_1}} + e^{i\vec{k}\cdot\vec{R_2}} + e^{i\vec{k}\cdot\vec{R_3}} \tag{6.10}$$

where ϵ is the eigen energy of the $2p_z$ orbital and $\gamma_0 \approx 3.0$ eV is the nearest neighbor interaction integral. $f(\vec{k})$ is set relative to the A sublattice and gives the sum of phase factors from the nearest neighbors contributed by the B sublattice. Diagonalizing the Hamiltonian obtains the eigenvalues and eigenfunctions:

$$E_\pm(\vec{k}) = \epsilon \mp \gamma_0|f(\vec{k})| \tag{6.11}$$

$$= \epsilon \pm t\sqrt{[1 + 4\cos^2\frac{k_y a}{2} + 4\cos\frac{\sqrt{3}k_x a}{2}\cos\frac{k_y a}{2}} \tag{6.12}$$

where the plus corresponds to the the antibonding (π^*) electronic band and the minus to the bonding (π) band. Notably, in this approximation, the π and π^* bands are degenerate near the K and K' points. Expanding Equation.6.10 near the degeneracy at the K and K' points, $\vec{k} = \vec{K} + \vec{q}(|\vec{q}| \ll |\vec{K}|)$ and at energies $(E - \epsilon) \ll t$ gives

$$E_\pm(\vec{q}) \approx \epsilon \pm v_F|\vec{q}| + \cdots \tag{6.13}$$

Thus, near the K and K' symmetry points, the Fermi velocity, $v_F \approx 10^6$ m/s, is independent of energy or momentum. Notably, the linear dispersion of graphene parallels that of photons of light– where we replace the speed of light by the Fermi velocity and note that $v_F \approx c/300$, remarkable for a solid state system. In further similarity to the linear dispersion of light and absence of a bandgap at the Dirac point, we note that the mass of electrons in graphene must too be zero. Most interesting for the work presented here, the

electronic structure and the symmetry from which it emerges determines most of the unique electronic, optical, and thermal physical properties in the atomically thin material.

The corresponding eigenfunctions can be written

$$\Psi_K(n\vec{q}) = \frac{1}{\sqrt{2}}e^{i\vec{q}\cdot\vec{r}}\begin{bmatrix} e^{-i\theta_q/2} \\ ne^{i\theta_q/2} \end{bmatrix} \tag{6.14}$$

where θ_q is the angle between the wavevector $\vec{q}$ and k_x, and $n = 1$ (or -1) for the conduction (or valence) band, respectively. This dual-component wavefunction has the same form as a spin-1/2 particle system, from which we derive the name *pseudo-spin* to describe this orbital degree of freedom. For in the K-valley, the direction of the pseudo-spin is parallel to momentum in the conduction band and antiparallel in the valence band. The two components in the pseudo-spin have the same amplitude and electrons in the A and B sublattices will experience the same potential. Consequently, the pseudo-spin is confined to the 2D plane. However, if the A and B sublattices are no longer symmetry – as is the case if the inversion symmetry is broken – the pseudo-spin will develop an out-of-plane component. The conical dispersion and pseudo-spin of the electronic states in graphene determine many of the unique electronic and optical properties in graphene [70, 71].

6.4 Optical transitions in graphene

In the single particle picture, there are two principle excitations in graphene, the direct interband transition and the direct intraband transitions, as illustrated in Figure 6.2. In this linear picture, the optical response of graphene is described by the optical conductivity $\sigma_{graphene}(\omega)$, and related to the permittivity by

$$\sigma_{3D}(\omega) = \frac{\sigma_{graphene}(\omega)}{d} \tag{6.15}$$

$$\varepsilon(\omega) = \varepsilon_0\varepsilon_r = i\frac{\sigma_{3D}(\omega)}{\omega} \tag{6.16}$$

where ω_{3D} is the effective three-dimensional optical conductivity, d is the thickness of graphene, and ϵ_r is the permittivity of the environment or background.

Interband transitions

Under an interband transition, an electron in the valence band is excited to the conduction band through the absorption of a photon. Since we will primarily consider normal incidence and the speed of light, c, is much larger than the Fermi velocity of the electron, v_F, we can neglect the momentum of the absorbed photon and consider the interband transition connecting states with the same momentum. The consequence of interband transitions can
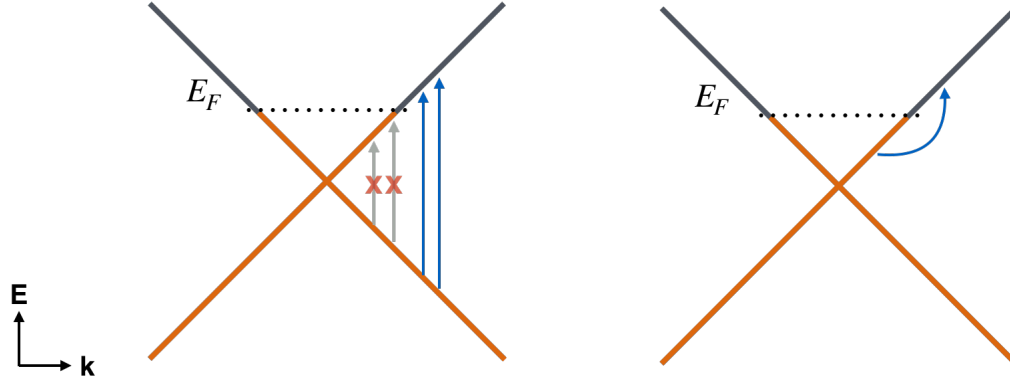
Figure 6.2: Optical transitions in monolayer graphene. Left: Interband transitions from filled states (orange) in the valence band to empty states (grey) in the conduction band. Transitions prohibited by the Pauli blocking effect are shown as grey lines with a red x. Right: Intraband transitions from filled states below the Fermi energy (E_F) to empty states above the Fermi energy within the same electronic band.

be described with first order perturbation theory and Fermi's golden rule for graphene in response to an external electromagentic field [72, 73].

We consider the propagation of an electromagnetic plane wave, $\vec{E} = E_0 \cos(\omega t)\hat{x}$ incident on a sheet of graphene whose Fermi energy is set to the charge-neutral point (all conduction states are empty and all valence states are filled). The incident energy flux W_0 is given by $W_0 = \frac{c}{4\pi}|\vec{E}|^2$. The absorbed energy flux by graphene is $W_{abs} = \Gamma\hbar\omega$. We describe the transition probability from an initial state using Fermi's Golden Rule, $\Gamma_{i\to f} = \frac{2\pi}{\hbar}|M_{if}|^2\rho_f(E_f)$, where Γ is the transition probability, M_{if} is the matrix element of the transition, and ρ is the density of states of the final state (at $E_f = E/2 = \hbar\omega/2$). The density of states in two dimensions is linear in energy: $\rho(E)_{2D} = \frac{m}{\pi\hbar}$, and thus for our 2D Dirac fermions, we can write $\rho(\frac{\hbar\omega}{2}) = \frac{\hbar\omega}{\pi\hbar^2}v_F^2$.

To make matters simple, we choose the gauge such that the scalar potential $\psi = 0$ and the vector potential $\vec{A} = A_0 e^{i\omega t}\hat{x}$, so that we can rewrite the electric field simply as $\vec{E} = \frac{\partial\vec{A}}{\partial t} = i\omega\vec{A}$. The beauty of selecting your gauge is that we can obtain the total Hamiltonian in the presence of an electromagnetic field by the simple substitution of $\vec{q} \to \vec{q} + e\vec{A}$ into Equation 6.13. The Hamiltonian describing the interaction of the electromagnetic field with the graphene sheet $\mathcal{H}'$ can be then written:

$$\mathcal{H}' = \frac{ev_F\sigma}{c} \cdot \vec{A} = \frac{ev_F}{i\omega}\sigma_x\frac{E_0}{2}e^{i\omega t} \tag{6.17}$$

and the total Hamiltonian of the electromagnetic wave impinging upon graphene

$$\mathcal{H} = \mathcal{H}_\prime + \mathcal{H}' = v_F\sigma \cdot (\vec{p} - \frac{e}{c}\vec{A}) \tag{6.18}$$

If we describe the initial state $|i\rangle = |v\vec{q}\rangle$ and the final state as $|f\rangle = |c\vec{q'}\rangle$ under the absorption of one photon as, we can write

$$\Gamma_{i\to f} = \frac{2\pi}{\hbar} |\langle i|\mathcal{H}'|f\rangle|^2 \delta(\hbar\omega_{i\to f} - \hbar\omega) = \frac{dW_{i\to f}}{dt} \tag{6.19}$$

From the eigenfunctions in Equation 6.14, the matrix elements can be simplified to

$$|\langle i|\mathcal{H}'|f\rangle|^2 = \left(\frac{ev_F E_0}{2\omega}\right)^2 \sin^2\theta_{\vec{q}}\delta_{\vec{q}\vec{q'}} \tag{6.20}$$

Averaging over all initial and final states, and taking into account both spin and valley degeneracies,

$$|\langle i|\mathcal{H}'|f\rangle|^2 = \frac{1}{8}e^2 v_F^2 \frac{E_0^2 \cos^2(\omega t)}{\omega} \tag{6.21}$$

$$= \frac{1}{8}e^2 v_F^2 \frac{|\vec{E}|^2}{\omega^2} \tag{6.22}$$

and we find

$$W_{abs} = \Gamma\hbar\omega \tag{6.23}$$

$$= \frac{c}{4\pi}|\vec{E}|^2 \tag{6.24}$$

The total power absorbed is

$$P = \Sigma_{i,f}\hbar\omega\frac{dW_{i\to f}}{dt} \tag{6.25}$$

$$= \frac{W_{abs}}{W_0} \tag{6.26}$$

$$= \frac{\pi e^2}{\hbar c} = \pi\alpha \approx 2.3\% \tag{6.27}$$

where α is the fine structure constant. By expressing total absorption, P in terms of optical conductivity,

$$P = \frac{1}{2}\mathfrak{Re}\left(\vec{j}\cdot\vec{E^*}\right) = \frac{1}{2}\mathfrak{Re}\left(\sigma\right)|\vec{E_0}|^2 \tag{6.28}$$

Comparing this to Equation 6.27, we find

$$\mathfrak{Re}\left(\sigma\right) = \frac{\pi e^2}{2h} \tag{6.29}$$

which is independent of frequency, ω. Here, we have obtained one of the striking properties of graphene: graphene's optical conductivity and absorption is independent of both frequency and any material-dependent parameter including the Fermi velocity, v_F and is defined only by

fundamental constants that are related to the confinement to two-dimensions and zero energy gap. This constant absorption in graphene is often referred to as a "universal absorption" and holds from the mid-infrared through ≈ 3 eV where the electronic dispersion deviates from a linear band.

As illustrated in Figure 6.2, the Fermi level determines the energy at which specific transitions are allowed or forbidden. The illustration above depicts an electron-doped (n-doped) graphene. Transitions with photon energy $\hbar\omega < 2|E_F|$ are forbidden due to Pauli blocking (grey lines). Transitions with photon energy $\hbar\omega > 2|E_F|$ are allowed (blue lines). The position of the Fermi level determines whether an interband transition of a specific energy is forbidden or allowed. As we will see in the following research chapters, the Fermi level can be tuned through electrostatic gating, which permits the threshold energy of permitted transitions to be tuned continuously.

To describe the Pauli blocking effect on the real and imaginary parts of the optical conductivity, we can describe the interband contribution of the optical conductivity as

$$\mathfrak{Re}\left(\sigma_{graphene}\right) = \frac{\pi e^2}{2h}\left[1 + \frac{1}{\pi}\left(\tan^{-1}\frac{\hbar\omega - 2E_F}{\gamma} - \tan^{-1}\frac{\hbar\omega + 2E_F}{\gamma}\right)\right] \tag{6.30}$$

$$\mathfrak{Im}\left(\sigma_{graphene}\right) = -\frac{e^2}{8\pi\hbar}ln\frac{\left(\hbar\omega + 2|E_F|\right)^2 + \gamma^2}{\left(\hbar\omega - 2|E_F|\right)^2 + \gamma^2} \tag{6.31}$$

where γ is the interband broadening from temperature, finite carrier lifetime, and inhomogeneous doping. The imaginary part of the optical conductivity is determined by the Kramers-Kronig relations.

Intraband transitions

The intraband transition in graphene is shown on the right in Figure 6.2 and connects initial and final states within the same band. Because of the large momentum mismatch between the Fermi velocity and the speed of light, intraband transitions require an addition momentum contribution, such as phonons or scattering from impurities and defects. Consequently, spectroscopic studies of intraband transitions can provide insight into the interaction of free electrons with impurities. The intraband transitions in graphene are often called the "free-carrier response," exhibit similar electrical and optical properties as simple metals, and can be described by Drude theory with an optical conductivity

$$\sigma\left(\omega\right) = \frac{D\tau}{\pi}\frac{1}{1 + i\omega\tau} \tag{6.32}$$

Here, the Drude weight, $D = e^2 v_F\sqrt{\pi n}$ and depends on the carrier density n. From this we see the tunability of the optical conductivity through electrostatic gating. The scattering time τ is related to the intraband broadening $\gamma = 1/\tau$, and is determined by defects in the sample and can be measured by DC transport measurements of conductivity.

Chapter 7

Imaging Electric Fields with Graphene Optoelectronics

> There are 360 degrees, so why stick to one?
>
> Zaha Hadid

7.1   Introduction

Signaling and manipulation through the control of electric field distributions is ubiquitous to both biological and physical systems. For example, intercellular electrical activity is central to the signaling and computation of excitable cells such as cardiac and neuronal cells [74]. The voltages generated by bio-electric fields span three orders of magnitude and can fluctuate on the scale of microseconds to hours [75, 76]. Likewise, the generation and manipulation of electric fields inside microscopic channels is the backbone of microfluidics and lab-on-a-chip diagnostics [77, 78]. In the latter applications, electric field gradients are intentionally designed to create strong dielectrophoretic forces, which permit the trapping and control of individual chemical droplets or biological samples along programmable pathways covering hundreds of microns [79, 80, 78].

Over the past decade, there has been a concerted effort to develop new techniques to observe and analyze the dynamic field fluctuations in liquids, such as the development of multitransistor arrays [81, 82], voltage-sensitive dyes [83, 84, 85, 86, 85], and new computational paradigms to model [87, 88] electric field behavior. However, it remains an outstanding challenge to achieve label-free, nonperturbative detection with high field sensitivity and high spatio-temporal resolution.

For example, the study of network-scale biological activity requires the ability to nonperturbatively record signals from ≈ 10 μm areas over a large field of view and with sub-millisecond temporal sensitivity. The predominant label-free method of detecting local electric fields across cellular networks are multielectrode and multitransistor arrays [89].

These techniques require prefabricated electrode arrays that are difficult to scale up, are individually amplified, and do not provide the flexibility to measure electrical fields at arbitrary spatial positions. Compared to electrical techniques, optical imaging permits high throughput detection that is compatible with simultaneous complementary measurements. Despite these advantages, there is little research into label-free optical platforms that permit the spatio-temporal detection of electric field distributions [90] . Here, we address this subset of problems with a critically coupled waveguide-amplified graphene electric field (CAGE) imaging platform, which permits label-free imaging of the dynamics of electric fields in solutions under non-equilibrium conditions [91].

7.2 A carbon lattice as a nonperturbative sensor of electric fields

Atomically thin materials like graphene offer exceptional opportunities for electrical field sensing due to their unique physical properties and intrinsic sensitivity to their environment. Over the past decade, graphene's optoelectronic properties have been studied extensively [73, 92]. In addition to its distinctive electronic transport properties, graphene couples strongly to light across the visible and the infrared frequency range. A pristine sheet of graphene has a constant absorption of $\pi\alpha \backsim 2.3\%$ at all frequencies [93]. In addition, this absorption can be modulated through electrostatic gating: a gate-induced shift of the Fermi energy that forbids specific optical transitions in graphene due to Pauli blocking (Figure 5.2). We employ this field-dependent optical absorption to achieve highly sensitive and parallel optical detection of local electrical fields.

Realizing this goal requires new optical designs that optimize the detection sensitivity and parallel readout simultaneously. For example, simple transmission mode imaging of gated monolayer graphene yields a 1% change of transmitted light over a gate voltage change of 200 mV around the Pauli blocking region. This results in a voltage sensitivity of only 2 mV, accounting for a typical laser with noise levels of 10^{-4}. However, physical and biological applications require orders of magnitude improvement in voltage sensitivity. To increase the light-matter interaction in graphene, researchers have explored different approaches such as coupling graphene to silicon waveguides [94, 95, 96], photonic crystal cavities [97, 98], plasmon resonances[99, 100, 101], and metamaterials [102]. These existing methods can improve the voltage sensitivity of optical detection, but are incompatible with parallel detection and imaging.

In our design, we paired a one-dimensional slab waveguide operated in a critical coupling configuration to amplify the natural optical responsivity from graphene under a local electric field perturbation. In the subsequent sections, I will discuss how we demonstrate highly sensitive, high-speed optical imaging of local electric field dynamics in solutions using graphene and a critical-coupled planar waveguide. Using a custom Python simulation, we designed the critically-coupled waveguide amplified platform to obtain the so-called critical

coupling condition [103] where the effective absorption of monolayer graphene approaches 100%. Close to the critical-coupling point, the voltage sensitivity can be enhanced by orders of magnitude. In addition, the planar waveguide permits two-dimensional time-resolved imaging of the electric field distribution in the solution above graphene.

We gave our device the *nom de guerre*, the "CAGE sensor", extracted from the **c**ritically coupled waveguide **a**mplified **g**raphene **e**lectric field sensor. As I'll discuss below, "CAGE" imaging achieves a voltage sensitivity down to a few microvolts, a response speed of microseconds, spatial resolution of several microns, and highly parallel readout of the dynamics of electrical field distributions.

7.3 Gate-dependent optical absorption in graphene

To optimize the optical response of the device, we examine the gate dependence of graphene's optical absorption in an ionic solution. To do so, we collect the optical reflection as a function of gate voltage from monolayer graphene on a glass substrate in ionic phosphate buffer solution with a Ag/AgCl under normal incidence at 1.55 μm. We can estimate the voltage sensitivity in this configuration based on the change in absorption in a transmission configuration due to the application of the external gate voltage to be $(\Delta T/T)/dV = 0.0048\%$ per millivolt of external gate.

The absorption is derived from the reflection data based on Fresnel equations. We find the absorption at zero-gate voltage to be 2.19 %, which is close to the theoretical universal optical absorption of graphene (2.3%). The absorption decreases around $\pm$ 0.4 V until ±1 V due to the band filling effect. The absorption of monolayer graphene can therefore be tuned from 0.47% to 2.19% over the gate voltage range $\pm1V$. The optical absorption of graphene, A_{gr}, contains contributions from both interband and intraband transitions in graphene. Its frequency dependence at different Fermi energies, E_F, can be approximated by

$$A_{gr}(E_F) = \frac{\pi e^2}{\hbar c} \left[1 + \frac{1}{\pi} \left(\tan^{-1} \frac{E + 2|E_F|}{\Gamma} \right) \right] + \frac{3e^2}{\hbar c \tau} \frac{|E_F|}{E^2 + (1/\tau)^2} \tag{7.1}$$

Where E is the incident photon energy, Γ, the broadening due to the interband transition, and $1/\tau$ the broadening due to the intraband transition. The Fermi level, E_F varies with the carrier concentration, n, as

$$E_F = h v_F \sqrt{\pi n} \tag{7.2}$$

where the Fermi velocity, v_F, is 1.1×10^6 m/s.

In the electrolytic cell, the average carrier concentration, n_0, can be described by a capacitor model

$$n_o = C(V_g - V_{CNP}) \tag{7.3}$$

Here, C is the capacitance of the solution double layer that forms at the surface of graphene under Ag/AgCl gating, and V_{CNP} is the charge neutral point. We can also introduce a

local carrier concentration broadening of $\Delta = 5 \times 10^{11}$ cm^{-2}. From this the conductivity of graphene can be modeled as:

$$A_{gr}(n_0) = \frac{\int A_{gr}(n)e^{-(n-n_0)^2/\Delta^2}dn}{\int e^{-(n-n_0)^2/\Delta^2}dn} \tag{7.4}$$

Fitting our data to this model with an 80 meV broadening of the intraband and interband transitions and a double layer capacitance of $C = 2.07\mu F$ cm^{-2}.

7.4 Experimental apparatus

The schematic of the CAGE structure is shown in Figure 7.1, formed of a prism-coupled slab waveguide coated on one side by large-area monolayer graphene. Large-area graphene
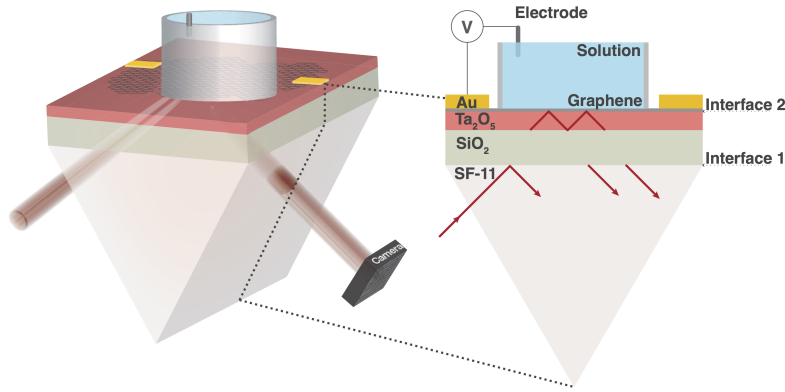
Figure 7.1: Illustration of the CAGE imaging device (left) with a cross-sectional schematic (right).

is grown by chemical vapor deposition and transferred to a prism coated with 150 nm of Ta$_2$O$_5$ (n = 2.0856), forming a high refractive index waveguide. We use an equilateral SF-11 glass prism (n=1.743) with a 1000 nm top layer of SiO$_2$ (n = 1.444) to evanescently couple the incident beam into the waveguide. The reflected light is then collected by an infrared objective and imaged onto an InGaAs camera and photodiode.

A collimated TE-polarized 1.55 μm incident beam is coupled evanescently into the waveguide at an oblique angle so that the condition for total internal reflection is satisfied at the SF-11/SiO$_2$ and Ta$_2$O$_5$ interfaces. Under this framework, we can describe the waveguide as a Fabry-Perot cavity with high reflection coefficients $|R_1|$ and $|R_2|$ at the two interfaces. Notably, $|R_1|$ and $|R_2|$ deviate from unity due to the frustrated total internal reflection from the finite thickness of SiO$_2$ at the first interface and the absorption of graphene at the second interface.

The total optical setup is shown (not to scale) in Figure 7.2. A stable, 1.55 μm 15
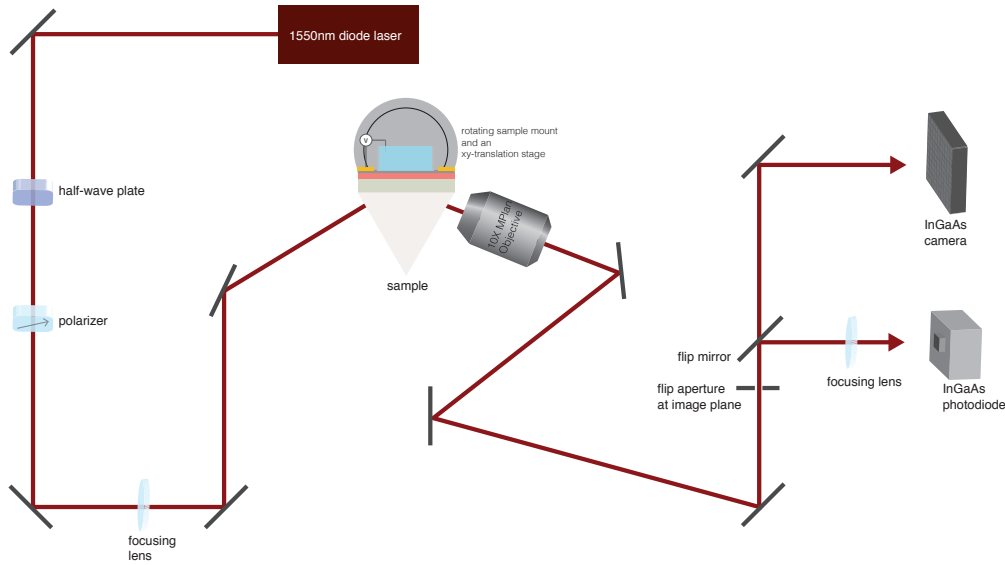
Figure 7.2: Diagram of the optical path

mW laser beam is generated by a butterfly telecom laser with a current and temperature
controller. The laser used here is Newport Model 708 8-Channel Butterfly, and the controller
is Newport Model 9016 Modular Controller. We fix the incident polarization in the TE-
direction using a half-wave plate and subsequently clean the outgoing beam using a calcite
polarizer.

In the imaging mode, the incident beam is collimated and coupled into the CAGE
platform for optimal sensitivity. In the scanning detection mode, the incident beam is
controlled with a 17.5cm focusing lens to have an NA=0.002 and selects an area at the
graphene interface. The incident light couples into the waveguide from one side of the
prism. The prism coated with the planar waveguide is placed on a XY-translational stage
and a rotating stage (center, Figure 7.2) which allow for fine-tuning of the sample position
and incident angle while keeping the input beam path fixed. The outcoupled light is then
collected by a 10X MPlan objective or a large lens and sent into an InGaAs two-dimensional
camera (Allied Vision Technologies Goldeye 008 SWIR), an InGaAs one-dimensional camera
(Andor 1.7 μm InGaAs DU490A) and into a low-noise InGaAs photodetector, respectively.
A circular iris is used to select the probing area for photodiode measurements. The specified
highest acquisition speed of the Goldeye camera is 186 fps. However, the native software,
Acquire Control, has maximum frame rate of 80 fps. For video collection in the subsequent
chapters, we operate the camera in an SDK configuration described below.

The Goldeye G-008 camear is interfaced to a desktop computer via a highspeed ethernet cable to a gigE CT card. We use two secondary software: Vimba SDK, which includes Vimba Viewer, and Streampix 7 from Norpix, which we use to record high-frame rate videos. When recording, the feature setting "Highspeedmode" must be set to "true" and the parameter, Height, must be manually set to Height = 160.

7.5 The critically coupled waveguide in CAGE

To describe the interaction of light with the multilayer device, we can separate the photonic system into two sub-systems: first, the $SF-11/SiO_2/Ta_2O_5$ stack and second, the $Ta_2O_5/graphene/solution$ stack.
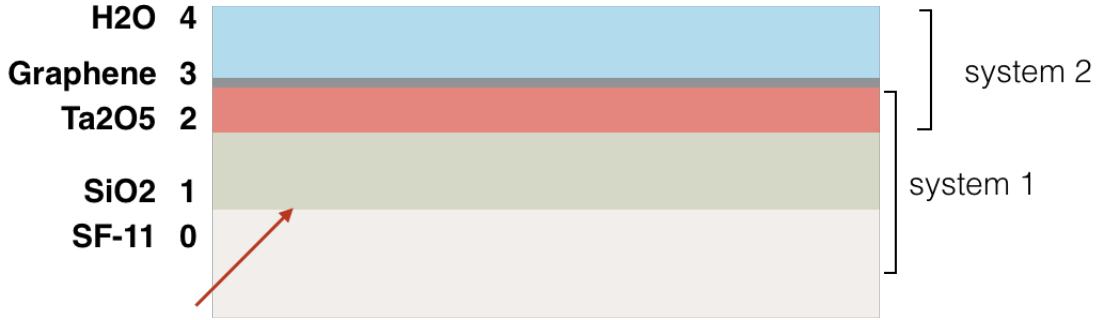
Figure 7.3: The photonic system into two sub-systems: first, the $SF-11/SiO_2/Ta_2O_5$ stack and second, the $Ta_2O_5/graphene/solution$ stack. The red arrow indicates the direction of incident light.

We can describe the first sub-system in the context of frustrated total internal reflection (FTIR) [104]. Frustrated total internal reflection takes place when an evanescent wave formed by total internal reflection in the high refractive index medium tunnels across a low index gap between two high refractive-index planes.

In the context of our first sub-system, SF-11 and Ta_2O_5 form the high refractive index layers where light is coupled through SiO_2 evanescently. We can describe reflection and transmission coefficients as R_{01} and T_{01} and R_{21} and T_{21}, corresponding to the light at the 0/1 interface between SF-11 and SiO_2, and that incident from the Ta_2O_5 side of the SiO_2, the 2/1 interface. From the Fresnel equations described above, we know that $|R_{01}| = |R_{21}|$ and $T_{01}T_{21} = (1 - |R_{21}|^2)e^{\delta_{01}+\delta_{21}+\pi}$, where δ is the phase [105].

The second sub-system is formed by the $Ta_2O_5/graphene/solution$ structure. The reflection R_{32} describes the reflection coefficient for light from the 3/2 interface in Ta_2O_5. We calculate R_{32} using the Fresnel relations and through the use of perturbation theory for graphene's absorption.

$$R_{32} = 1 - A_{gr} \times \text{Re}\left[\frac{(1 + R_{32}^0)^2}{R_{32}^0}\right] = 1 - A_{gr} \times 1.66 \tag{7.5}$$
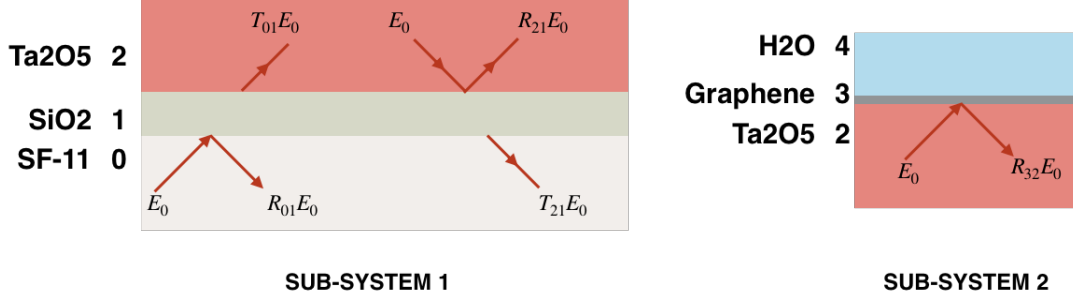
Figure 7.4: Cross-section of the CAGE interfaces, described here as subsystem-1 and sub-system 2. These two sub-systems act as highly reflective interfaces and form a Fabry-Perot cavity.

where A_{gr} is graphene's absorption, and R_{32}^0 is the reflection coefficient at the Ta_2O_5/solution in the absence of graphene.

These two sub-systems each form a highly reflective interface because the coefficients T_{01}, R_{21} and R_{32} can be very large. As a result, we can treat the optical cavity formed by these two interfaces as a Fabry-Perot cavity. We consider the total reflected radiation, E_r as the interference of the multiple reflections in the reflective cavity

$$\frac{E_r}{E_0} = R_{01} + T_{01}T_{21}R_{32}e^{\imath\delta}\left[1 + (R_{21}R_{32}e^{\imath\delta}) + (R_{21}R_{32}e^{\imath\delta})^2 + \ldots\right] \tag{7.6}$$

$$= R_{01} + \frac{T_{01}T_{21}R_{32}e^{\imath\delta}}{1 - R_{21}R_{32}e^{\imath\delta}} \tag{7.7}$$

where E_0 is the incident electric field as indicated in Figure 7.4, $e^{\imath\delta}$ is the total phase accumulation of the propagating beam in the Ta_2O_5 waveguide cavity. Relating the reflection and transmission coefficients via the relations described above and defining $\Delta = \delta_0 + \delta_1 + \delta_2 + \ldots$ to be the round trip phase accumulation in the waveguide, we can simplify Equation 7.7 to

$$\frac{E_r}{E_0} = e^{\imath\delta}\frac{|R_{21}| - |R_{32}|e^{\imath\Delta}}{1 - |R_{21}||R_{32}|e^{\imath\Delta}} \tag{7.8}$$

The resonance condition of the Fabry-Perot cavity takes place at constructive phase accumulation, $e^{\imath\Delta} = 1$, which is the same condition as the zeroth mode for a planar waveguide [106]. The total phase accumulation depends sensitively on the angle of the incident beam coupled into the waveguide structure. At the resonance condition, the total reflection from the cavity is given by

$$R = \frac{(|R_{21}| - |R_{32}|)^2}{(1 - |R_{21}||R_{32}|)^2} \tag{7.9}$$

Because graphene's optical absorption can be varied by an electrostatic gate, the value of $|R_{32}|$ can be varied *in situ* (Figure 7.5). As seen in Figure 7.5,
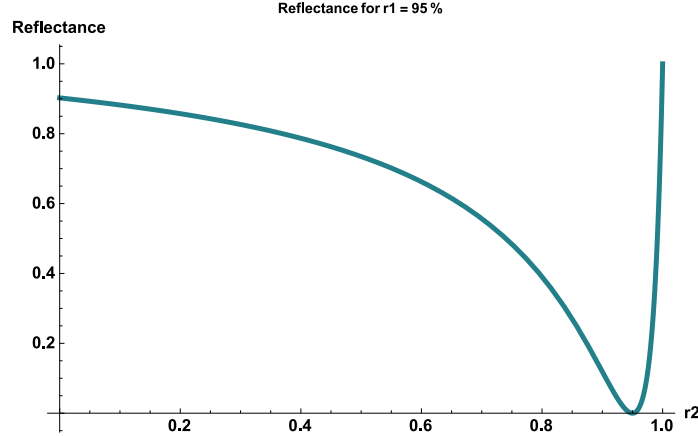
Figure 7.5: By tuning the value of $|R_{32}|$, the total reflectance from the cavity can be varied dramatically.

$$|R_{32}| = 0 \rightarrow R \approx 1 \quad (7.10)$$

$$|R_{32}| = 1 \rightarrow R = 1 \quad (7.11)$$

$$|R_{32}| = |R_{21}| \rightarrow R = 0 \quad (7.12)$$

To obtain the highest sensitivity to the local electric field at the 3/4 interface, we gate graphene to the critical coupling condition, where $|R_{21}| = |R_{32}|$ and the total reflection, R=0 indicating that all of the propagating radiation has been absorbed by graphene over the propagation distance of the waveguide.

7.6 Characterization of the CAGE optical response

The operational sensitivity of CAGE detection to the dynamics of the local electric field is characterized by the relative reflectivity change, dR/R, caused by a change in voltage induced by the local electric field, dV. Figure 7.6 shows the gate-dependent reflectivity response of a typical CAGE detector in a saline solution. The incident 1.55 μm beam is collimated and TE polarized, as discussed earlier.

The resonance condition of the waveguide determines the angle of incident light inside the SF-11 coupling prism to be $\approx$ 60 degrees from normal. With a 1000 nm SiO2 layer, the frustrated total internal reflection $|R_{21}| = 98.2\%$. The reflection coefficient at the Ta_2O_5/solution interface, $|R_{32}|$, is 97.5% at the charge neutral point (Vg = -0.14V) due to graphene absorption, which leads to a total reflection of R $\approx$ 1.5% . Graphene absorption can be set subsequently by electrostatic gating through the solution. The critical coupling condition $|r_1| = |r_2|$ is realized at $Vg = +0.41$ V (electron doped) and $Vg = -0.69$ V (hole doped), resulting the lowest total reflectivity, R. (The residue value of R=0.63% at critical
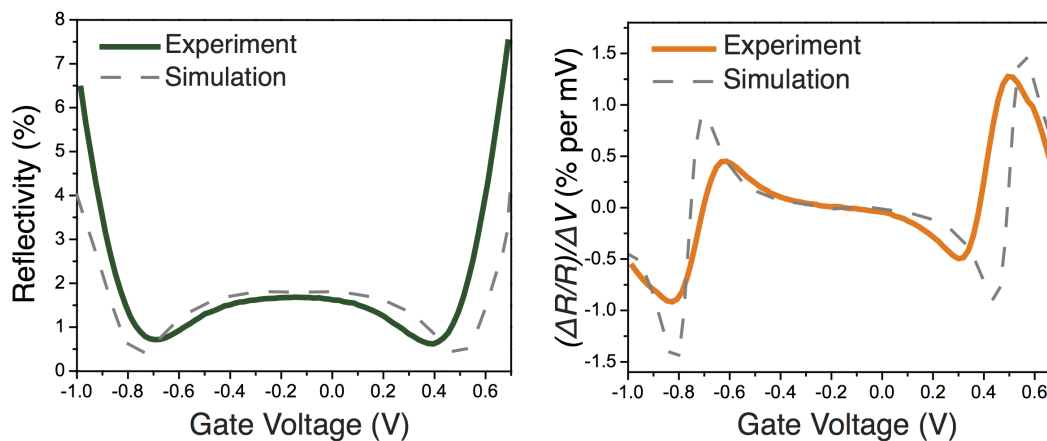
Figure 7.6: Characterization of the optical response of the CAGE sensor.

coupling is due in part to a slight divergence in the incident beam and in part due to defects
in the CVD-grown graphene and the waveguide thin film deposition). Further increase of
carrier doping leads to a decrease of graphene absorption corresponding to $|r_1| < |r_2|$ and one
obtains an increase in total reflectivity. The grey dashed line in Figure 7.6 shows the sim-
ulated optical response of our device using graphene absorption determined experimentally.
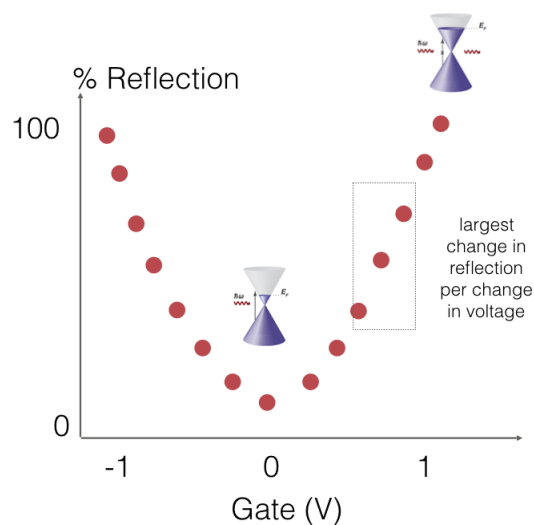
Figure 7.7: Schematic of the maximum sensitivity of the CAGE sensor in the context of
graphene's Fermi energy.

The sensitivity of CAGE detection to dynamics of the local electric field is charac-

terized by the relative reflectivity change, dR/R, caused by a change in voltage induced by the local electric field, dV. The right figure in Figure 7.6 shows the calculated (dR/R)/dV as a function of the gate voltage from the reflectivity response shown on the left of Figure 7.6. CAGE detection is most sensitive close to the critical coupling condition, where the greatest optical modulation is achieved for a given change in local electric field (Figure 7.6). For example, a single millivolt of field-induced voltage produces a 1.2% change in reflection at Vg = 0.53 V. This sensitivity is over 200 times higher than that of the direct transmission configuration (1% optical change per 200 mV). The noise of the commercially available 15 mW 1.55 μm butterfly diode lasers is around 0.01% RMS across a 10 Hz - 10 kHz bandwidth. Consequently, the CAGE detection permits optical readout of electrical voltages smaller than 10 μV across a wide field of view.

7.7 Noise floor and bandwidth
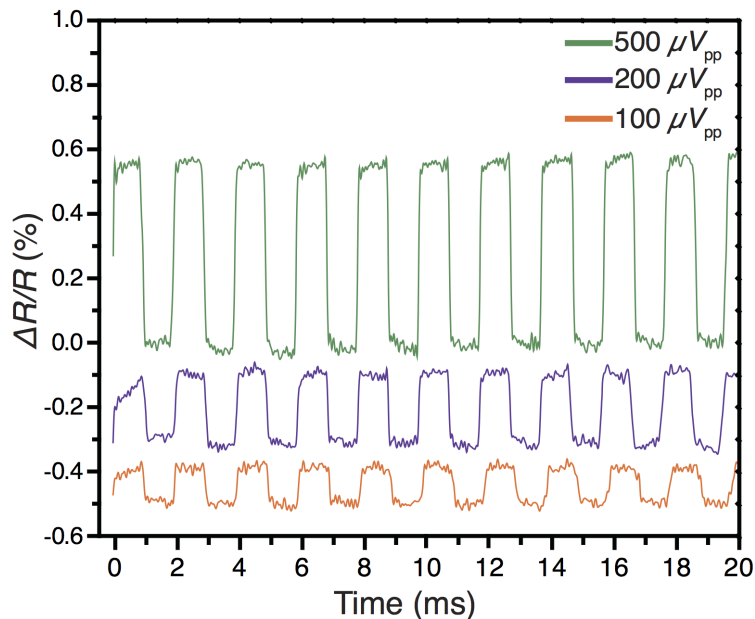
Figure 7.8: Voltage sensitivity of the CAGE field sensor: A periodic rectangular waveform is applied with varying peak-to-peak voltages and the optical response is recorded.

CAGE optical detection of small electric field fluctuations is demonstrated in Figure 7.8. The gate voltage at graphene was set at the highest sensitivity point (0.53 V, as seen in Figure 7.6). We applied periodic rectangular pulse sequences with peak voltages ranging from 500 μV to 100 μV and recorded the optical readout with a wide band-pass filter from 10 Hz to 10 kHz. The relative reflectivity change is 0.58 %, 0.23%, and 0.11% for 500 μV, 200 μV, and 100 μV voltage pulses, respectively. The results are consistent with the

(dR/R)/dV = 1.2% per mV reported in Figure 7.6. Clear periodic modulation is observed at
Vpp = 100 μV with a signal to noise ratio (SNR) of 6.5. This measurement reflects optical
detection capabilities of $\approx 15\mu$V or, equivalently, a change of carrier concentration of 2.3^8
electrons/cm^2 in graphene. The noise level at 0.017% in Figure 7.8 is due to a combination
of laser intensity fluctuations and vibrations of optical components. Much higher SNR and
therefore higher voltage sensitivity would be possible by improving the optomechanical and
laser source stabilities.
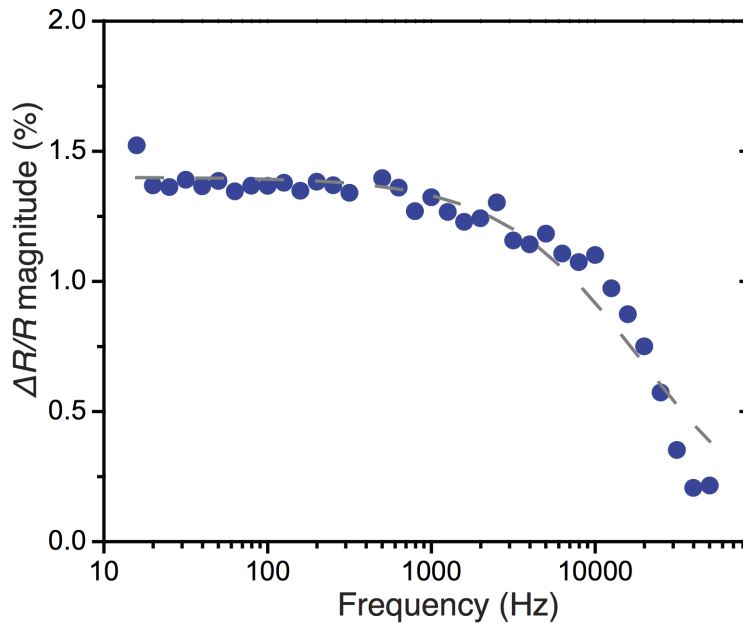
Figure 7.9: Temporal bandwidth of the CAGE sensor: the frequency dependence of the
optical signal demonstrates sensitivity to high speed fluctuations up to 10 kHz. The results
provided by an RC equivalent circuit that accounts for the double layer capacitance and
graphene resistance is plotted in the grey dashed line.

The temporal response of CAGE detection is determined by the RC constant of the system,
where C is the capacitance of the graphene/electrolyte interface and the resistance, R, is
governed by graphene conductance. For local electrical field fluctuations, the effective area
and capacitance is small and the response speeds can be very high. Experimentally, we
characterized the frequency response of the CAGE detector using a relatively large graphene
area (200 μm by 400 μm), underscoring the applicability of our measurements to large
fields of view. Figure 7.9 shows that the dR/R value remains largely constant up to 10
kHz and decreases at higher frequencies. These measurements yield a 3 dB frequency of 13
kHz (Figure 7.9 dashed) and an RC constant of 20 μs. This 10 kHz fast response enables
direct observation of electric field dynamics on timescales spanning action potentials [2,3]
and electrophoretic manipulation [8,9].

7.8 Detecting local electric field fluctuations with spatial and temporal resolution

In the previous sections, we have described how the CAGE sensor works, how to conceive of its efficacy, and tested its bounds in voltaic and temporal resolution. Now, we will discuss its ability to not only detect but to image, rapidly and in parallel across a wide field of view.

Spatial resolution

The spatial resolution of the CAGE imaging system is dominated by the propagation distance in the waveguide. There is a direct inverse relation between the voltage sensitivity of the system and the spatial resolution: for higher spatial resolution, we require a shorter waveguide propagation distance, which limits the total effective signal amplification. Another important consideration discussed earlier is graphene's optical responsivity as a function of wavelength, which is maximized in the near infrared regime. All subsequent considerations assume $\lambda = 1550$ nm. For the future applications discussed above, we designed the waveguide to permit a voltage sensitivity of 10 μV which corresponds here to a spatial resolution of 10 μm.

To demonstrate the spatial resolution of the CAGE imaging system, we spread polystyrene microspheres with a diameter of 1μm across the graphene/waveguide surface. Figure 7.10 shows an image taken with the CAGE optical system of one polystyrene micro-
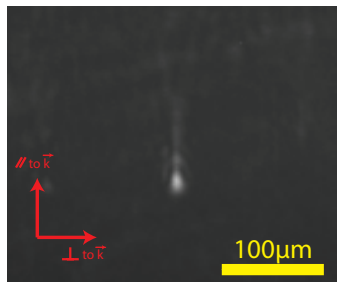
Figure 7.10: An image of the microsphere taken with the CAGE optical system.

sphere. Using a 10X MPlan objective with an N.A. = 0.26, we obtain a 7μm lower limit for spatial resolution. Since the smallest resolvable feature is larger than the diameter of the polystyrene microsphere, we treat the microsphere as a point source and can use the intensity profile to report the point spread function of the system. The intensity profiles of the linecuts are shown in Figure 7.11 in the directions parallel and perpendicular to the direction of propagation in the waveguide, $\vec{k}$. The FWHM is 10 μm in the $\vec{k}_\perp$ direction and 16 μm in the $\vec{k}_\parallel$ direciton, which represents the spatial resolution in each direction of the waveguide. We also observe a long decay of 40 μm in the $\vec{k}_\parallel$ which is due to the slow decay in the direction of propagation. Focused light have a finite angular spread due to the
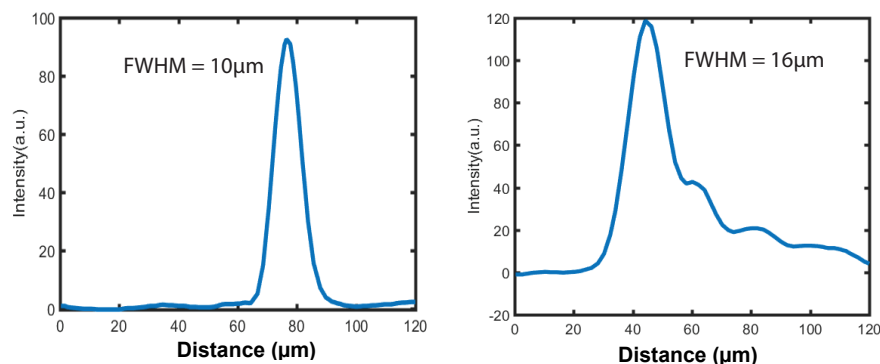
Figure 7.11: Spatial resolution of the CAGE sensor: An linecut from the CAGE image of the local field perturbation due to the microsphere demonstrates the detector spatial resolution.

uncertainty principle that leads to interference which appears as multiple secondary peaks in the direction of waveguide propagation.

Spatio-temporal resolution

We test the spatio-temporal dynamics using a proof-of-principle setup based on generating a local electric field via external electrode through a ionic solution. Figure 7.12 shows a schematic of our experimental setup. A platinum/iridium microelectrode is placed 5
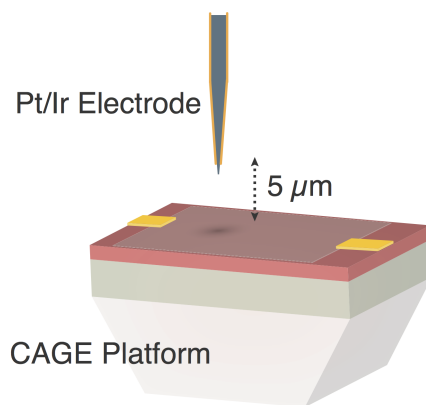
Figure 7.12: Geometry of the experimental setup. Applying a waveform to the microelectrode generates a spatially distributed electric field pattern and permits observation of the local electric field modulation in space and time.

μm above the device to create a spatially varying electric field distribution. The spatially

resolved reflection from the graphene plane is projected to the image plane using a long
working distance near-IR objective, which we image onto an InGaAs camera.

The spatio-temporal dynamics of local electric fields in solution are captured by the
CAGE device at the critical coupling condition and imaged onto a 1D InGaAs camera array
in Figure 7.13.

Figure 7.13: CAGE image with spatio-temporal resolution of the first 70 ms of local electric
field dynamics generated by a 1-mV 200 ms pulse applied to a microelectrode $5\mu m$ above
the surface

A 10mV electrical pulse with a 200 ms duration is applied at the microelectrode
generating a 1.8 mV local potential at the graphene/solution interface beneath the micro-
electrode tip. Positions A1, A2, and A3 are increasingly distant from the field source. The
time traces of these spatially resolved positions are plotted in Figure 7.14.

At position A1, immediately below the excitation electrode, we observe the perturbed
reflection intensity due to a fast transient voltage peak that decays in ≈ 25 ms to a stationary
potential (solid yellow line). As one moves increasingly distant from the field source, the fast
transient peak correspondingly reduces (green and blue solid lines).

This behavior matches well with the results of our finite element simulation and
may be qualitatively described by an equivalent circuit. The equivalent circuit consists of
impedance from the solution-electrode interface, resistance from the solution, and impedance
from the graphene-solution interface. The value of the resistance and capacitance extracted
from our data are consistent with values estimated from other experiments. The stationary
potential can be thought of as the stead-state of the circuit when the capacitor is fully
charged and the transient voltage is due to the capacitor charging. The dynamical solution
of the equivalent circuit is shown as grey dashed lines. The voltage sensitivity is determined
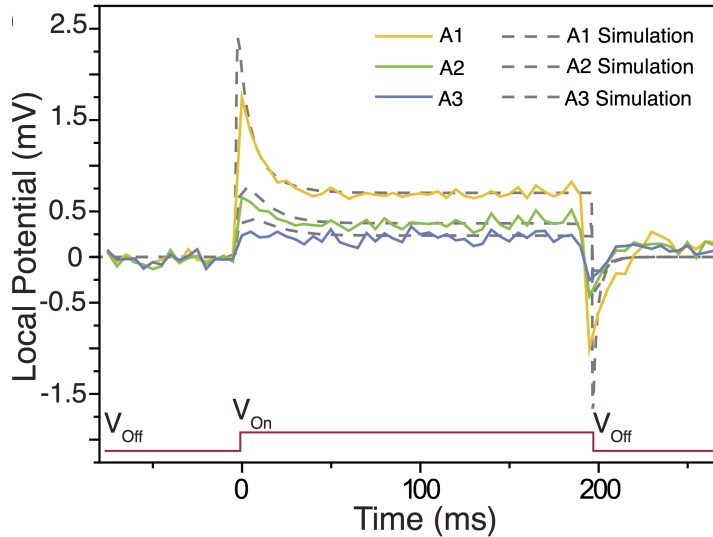
Figure 7.14: CAGE image with spatio-temporal resolution of the first 70 ms of local electric field dynamics generated by a 1-mV 200 ms pulse applied to a microelectrode 5μm above the surface.

by the $\approx$ 100 mV RMS noise present before the onset of the excitation; this sets the upper bound of voltage resolution in the one-dimensional camera array.

We observe the field dynamics with 5 ms temporal resolution and 100 mV voltage sensitivity across a full 200 mm. The lower voltage sensitivity in the imaging mode compared with a single InGaAs photodiode is due to the slower speed and a limited dynamic range of our InGaAs array. In the future, the voltage sensitivity and temporal resolution could be extended to is few-μV levels by adopting a better array detector.

Frames from a CAGE video of local electric field dynamics recorded via an 80 Hz 2D InGaAs camera are shown in Figure 7.15. The spatial resolution of our device is on the order of 10 μm as described above. Each frame is normalized by an image taken in zero-field. Compared with the recordings in Figure 7.14, we expect that time $t = -10$ to 0 ms captures the period in which a positive transient voltage emerges and subsequently dissipates away from the excitation micro-electrode, and $t = 190 - 240$ ms captures the period in which a negative transient voltage recovers to zero. Indeed, the data show that a positive voltage emerges and then diffuses spatially in frames 1–4, and a negative voltage appears and recovers to the equilibrium state in frames 5–8. These results demonstrate that dynamic spatial variations of local electric fields can be imaged in real time via the CAGE imaging platform.
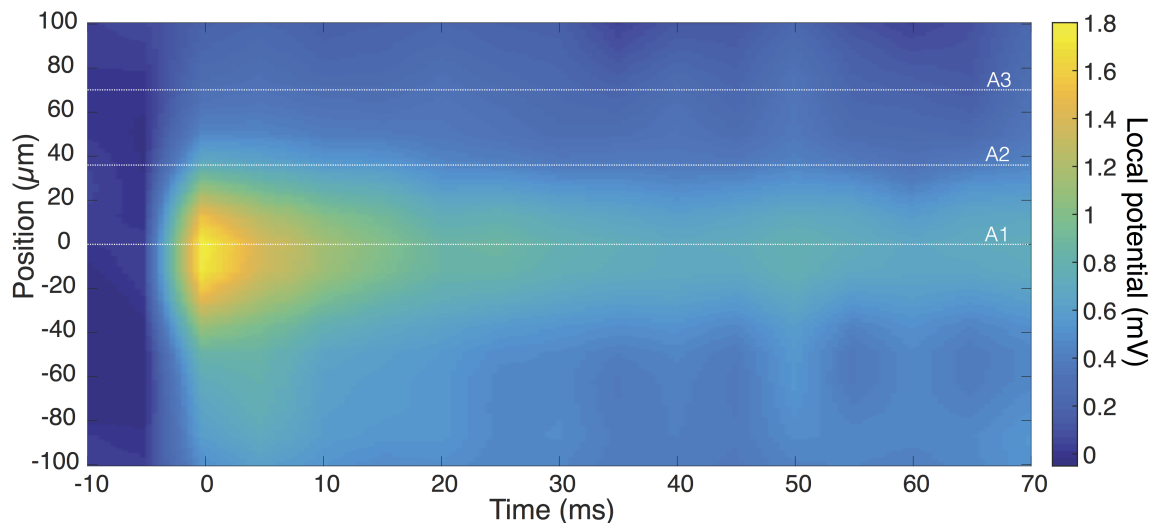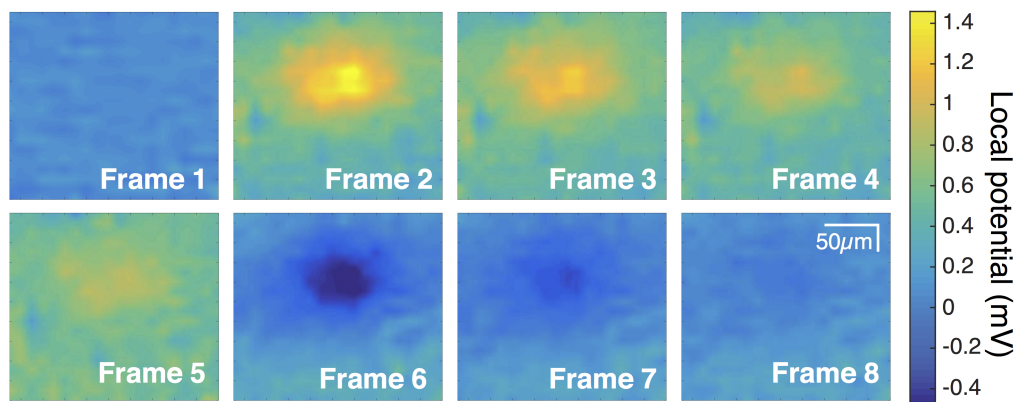
Figure 7.15: CAGE image with spatio-temporal resolution of the first 70 ms of local electric field dynamics generated by a 1 mV pulse with a duration of 200 ms applied to a microelectrode 5 μm above the surface.

7.9 Conclusion

In summary, we present a method of imaging local electric field dynamics under ambient conditions with high voltage and spatio-temporal resolution through the critically-coupled waveguide amplified graphene electric field (CAGE) imaging platform. This label-free and highly parallel technique offers over 200-fold improvement over conventional graphene based optical sensing and resolves sub-15 μV fluctuations with a bandwidth of 10 kHz across a wide field of view. The CAGE imaging platform may be used simultaneously with complementary measurements and may be spectrally tailored to enable broad applications from improved engineering of lab-on-a-chip devices to sensing bioelectric phenomena across cellular networks.

Chapter 8

Imaging Extracellular Action Potentials with Single Cell Resolution at Network Scale

> Our brains have approximately a quadrillion time a quadrillion atoms
> operating in absolutely superb design coordination by which, for
> example, you and I are communicating.
>
> <div align="right">Buckminster Fuller</div>

8.1 Introduction

The observation of electrical activity in networks of excitable cells underlies current progress in neuroscience, cardiology pharmacology, and cell biology. From microvolts to millivolts and microns to millimeters, the activity of electrogenic networks span multiple orders of magnitude in both space and time. The development of non-invasive, parallel, and scalable methods that permit network-scale recordings with single cell resolution remains a key goal in electrophysiological studies of electrogenic cells and cell networks. In this chapter, I will discuss our application of the CAGE sensor to demonstrate label-free imaging of extracellular potentials with single-cell resolution across an electrogenic network. I apply our technique to both monolayer and tissue cardiac cells and demonstrate the ability to noninvasively detect electrical activity from single-cell action potentials to the propagation of potentials across the cellular network and their modification by pharmacological agents. The platform is robust over long measurement times, is scalable in highly parallel detection, and is directly compatible with other existing microscopy techniques for multi-model bio-imaging.

1 meter	Central Nervous System	← You are here
10 - 1cm	Systems/Maps	
1 mm	Neuronal Networks	
100 um	Neurons	
1 um	Synapses	
1 Å	Molecules	
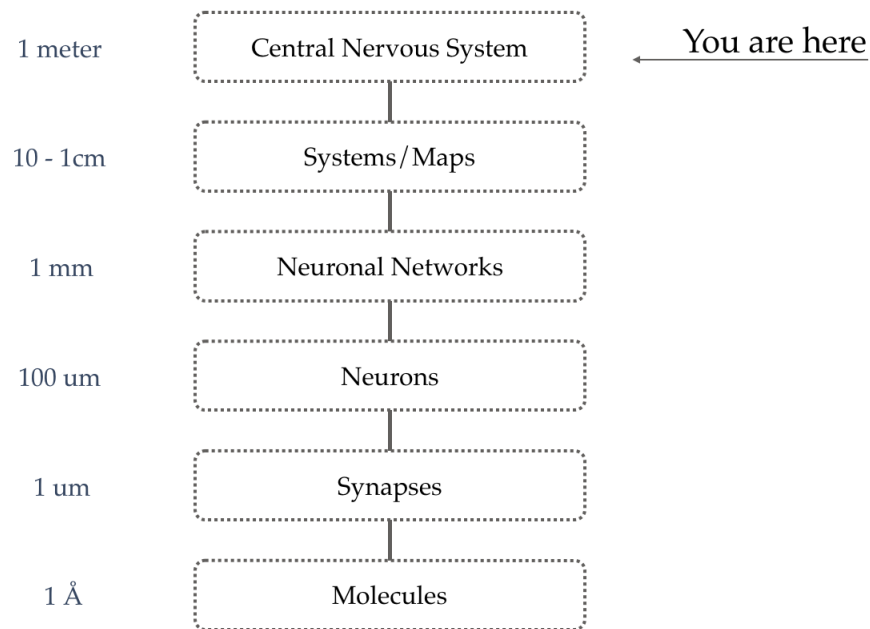
Figure 8.1: Scales of bioelectric activity span ten orders of magnitude.

8.2 Current approaches in bioelectric detection

For the past three decades, new technologies that detect electrophysiological signals have driven research spanning medical interventions for cardiac arrhythmias to the connectomics of neurons to our understanding of the neural network computation and new perspectives on information theory. New techniques have an outsized impact on scientific discovery, which makes it appropriate to (briefly) summarize some of the current tools of the trade.

Foundations of electrophysiology: patch clamp

The first method and gold standard of intracellular (i.e. cross-membrane) measurement of action potentials is through use of the patch clamp. The patch clamp technique was first implemented in 1976 by Neher and Sakmann to measure currents passing through a frog skeletal muscle. The principle of patch clamp is to electrically isolate a point in the cell lipid bilayer membrane such that measurements of the current and differential voltage across the membrane can be measured directly. To do so, one uses a glass pipette whose tip has been fire-polished to achieve a sub-nm surface roughness. The beauty of this approach is, it turns out, that glass polished in this way will form an irreversible seal with a cell lipid membrane that allows for a *seal resistance* in the 10 GΩ regime. Patch clamp permits us to directly measure the voltage drop across a cell membrane in real time. Moreover, each measurement has a one-to-one correspondence with a specific single cell. This permits correlation of cellular behavior as a function of known and unknown inputs and outputs at
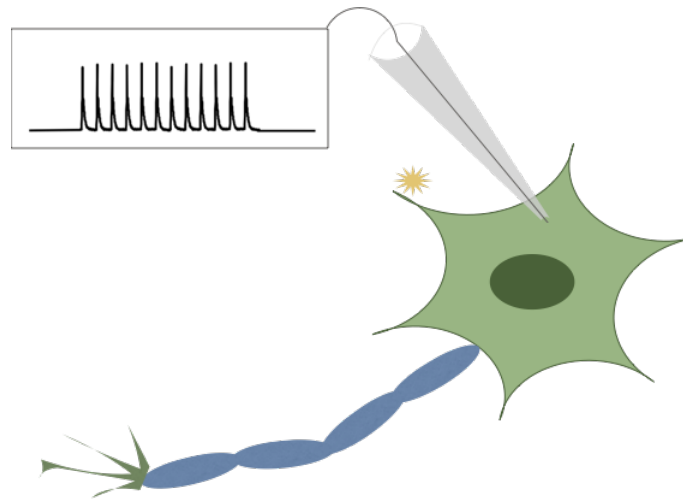
Figure 8.2: Illustration of a patch clamp measurement. Not to scale.

the single-cell level.

Downsides of the patch clamp approach are that it (naturally) irreversibly damages the cell membrane. The presence of the patch in the membrane further disturbs the membrane potential, which is sensitive to small changes in the local potential that drives intercellular signalling. As described above, patch clamp measurements are challenging to scale. The flip side of one-to-one correspondence is that the experimental task also scales as one-to-one.

Voltage-sensitive dyes

Excellent work in the development of voltage sensitive dyes leverage small-molecule fluorescence to transduce the bioelectric signal into the optical regime [107, 108, 109]. Voltage
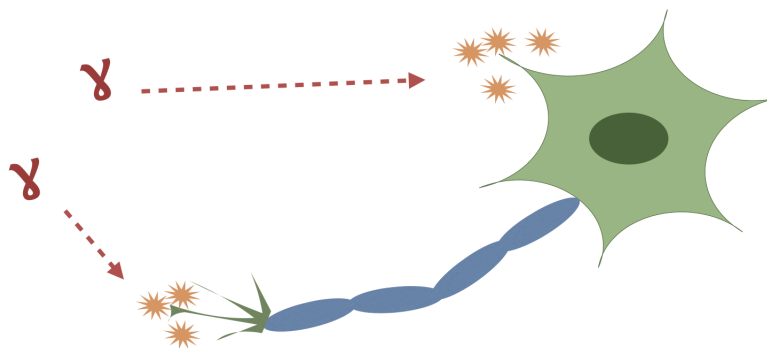
Figure 8.3: Illustration of fluorescence-based detection of action potentials and calcium transients via voltage sensitive dyes, calcium indicators, and small-molecule probes.

sensitive dyes offer a lower cost and more flexible approach compatible with a range of microscopies. Exogenous and endogenous dyes further permit mapping of electric activity across regions and even entire organisms, often with single cell or near-single cell resolution. While enormous advances have been made to overcome challenges of optical imaging through dense and highly scattering tissue, challenges persist in cytotoxicity, photobleaching, quantitative readout, and perturbation due to chemo-sensitivity.

Multi-electrode arrays and field effect transistors

Traditional semiconductor technologies gave rise to complimentary metal-oxide semiconductor multielectrode arrays (MEAs) and field effect transistors that couple to nearby AC signals in open-circuit mode [110, 111, 112, 113]. These multi-electrode arrays are scalable and sensitive extracellular measurements that rely on the use of a planar or extruding electrode over which an *in vitro* cell culture is grown. Among the greatest advantages of MEA-based measurements is the ability to measure populations of hundreds of cells simultaneously over extended time frames (weeks to months).
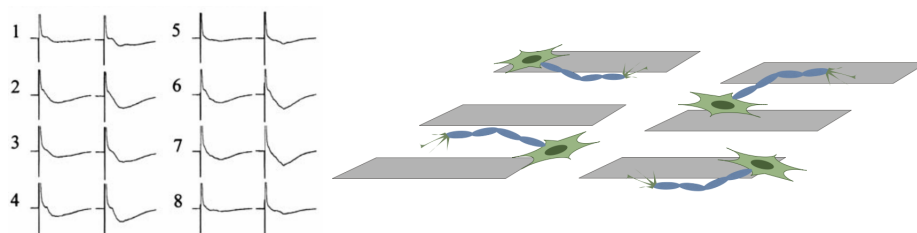
Figure 8.4: Illustration of measurements through multi-electrode arrays (MEA).

Though robust and mature, electrode-based techniques require individual amplification, are limited by crosstalk and available fabrication techniques, and do not permit continuous one-to-one mapping of cellular activity. In addition, these planar probes are restricted, largely, to *in vitro* or slice-based measurements.

CAGE sensing for label-free imaging of bioelectric signals with high spatiotemporal resolution

The challenges laid out above can be largely overcome by working in the optical regime where imaging naturally permits highly parallel detection and spatiotemporal resolution. In the following sections, I will describe how the CAGE sensor [91] discussed in the prior chapter retains advantages of both optical and electrical modalities, permitting label-free, real-time, spatiotemporal imaging of bioelectric signals with quantitative readout. Throughout the following sections, we will demonstrate label-free single shot imaging of action potentials in both live tissue and monolayer cultures, with single cell resolution across a wide field of view.

8.3 Simultaneous Imaging

Optically transparent and chemically inert, CAGE sensor can be easily integrated into measurements with other optical and chemical modalities such as white light and fluorescence microscopy. Figure 8.5 provides a photograph of the experimental apparatus and a schematic of the setup, respectively.
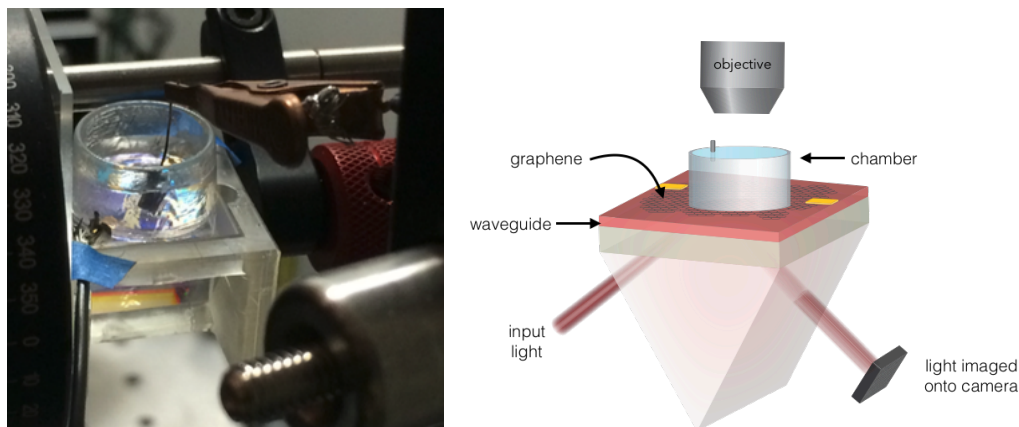
Figure 8.5: Left: Photo of the CAGE sensor under operational conditions. Right: Illustration of the CAGE sensor with simultaneous white-light imaging.

Our experiments use chicken primary cardiac tissue and human-induced pluripotent stem cells (hiPSC)-derived cardiomyocytes. Figure 8.5 (left) depicts the experimental setup. As before, an infrared laser couples into the waveguide, illuminating a $\approx$ 1.5 mm area at the waveguide/graphene interface. The presence of an action potential generates a local extracellular potential at the position of the cell on the graphene surface, which modulates the amplitude of graphene's local optical absorption in time. This change in absorption is amplified over the waveguide propagation distance and appears as a spatio-temporally resolved change in reflectivity in the light coupled out of the device. The signal can be collected on a single photodiode or imaged onto a 2D CCD array, respectively.

Figure 8.6 shows an optical micrograph of cardiomyocytes cultured on the CAGE detector and imaged using the white light microscope built above the sensor for simultaneous imaging.

Figure 8.7 show our white light microscope and a simultaneous white light and a CAGE image of cultured cardiomyocytes. Simultaneous imaging permits the correlation of multiple modalities in real-time and with one-to-one correspondence of network-scale behavior with single-cell resolution.

In future work, this simultaneous imaging could be extended to include fluorescence microscopy, spectroscopy, and be paired with advanced electrophysiological techniques including optogenetic excitation and superresolution microscopy.
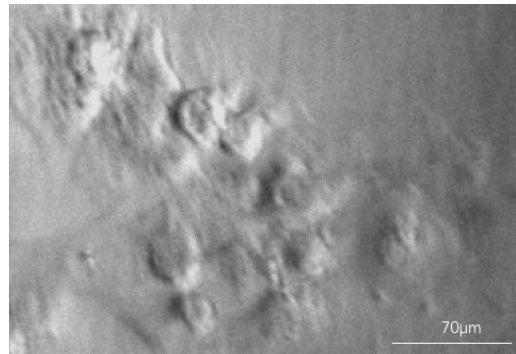
Figure 8.6: White light optical micrograph of the cultured cardiomyocytes on the CAGE detector.
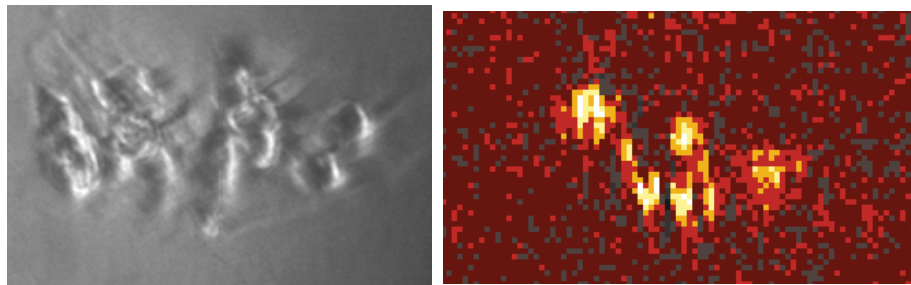
Figure 8.7: Left: Optical micrograph of cultured cardiomyocytes on the CAGE sensor. Right: Simultaneous CAGE image of the cultured cardiomyoctes.

We first demonstrate the label-free optical detection of extracellular field potentials from primary chicken cardiac tissue by the CAGE sensor (Figure 8.8). The sensor detects a signal with two components: a fast (5 ms) extracellular signal from the action potential (Figure 8.8 inset) and a slowly varying signal which peaks around 500 ms thereafter, generated by the spontaneous mechanical beating of the cardiac tissue.

8.4   Label free detection of bioelectric activity

Our detection scheme is sensitive to both changes in the local electric potential and modulations to the local refractive index. When cardiomyocytes fire action potentials, their myofilaments contract causing the cells to move relative to the detector. This relative motion modifies the local refractive index at the position of the firing cell and is captured by our detector, enabling us to simultaneously detect electrical and mechanical signals.   The electrical and mechanical signals can be quantitatively separated by a measurement of the gate-dependent reflectivity. The mechanical signal has contributions from changes to the local refractive index due to cell contraction. In contrast, the action potential produces
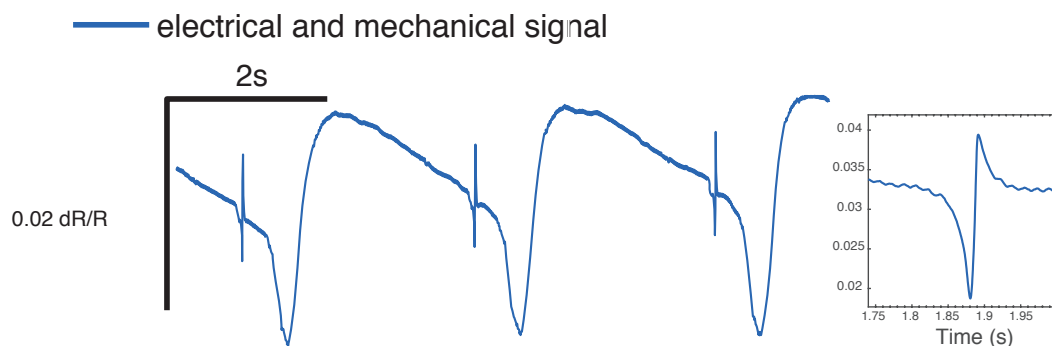
Figure 8.8: CAGE optical signal of extracellular field potentials from cardiac tissue.

a well-defined local electric field on the graphene surface, which quantitatively follows the
gate-dependent optical response of the sensor.
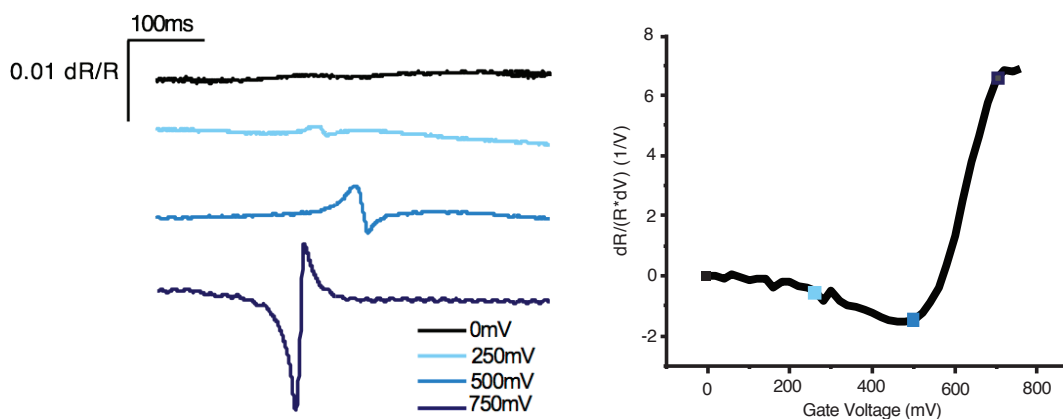
Figure 8.9: Optical response due to bioelectric signal follows graphene's reflectivity.

In Figure 8.9, we monitor the electrical signal in Figure 8.8 as a function of increasing
gate voltage. With increasing gate voltage, the waveguide approaches its critical coupling
condition and the amplitude of the electrical peak increases dramatically to clearly resolve
the bioelectric signal (Figure 8.9, right).

Plotting the peak amplitudes as a function of voltage, we see the sensor readout
of the electrical signal shows good quantitative agreement with expected sensitivity curve
of the CAGE device, including the expected change in polarity (Figure 8.9, left). The
extracellular potential drives a 1% change in reflectivity (dR/R) collected by the detector,
corresponding to an extracellular potential of 1.67 mV, in good agreement with our MEA
data and previously reported values, and a signal-to-noise ratio (SNR) of over 100.
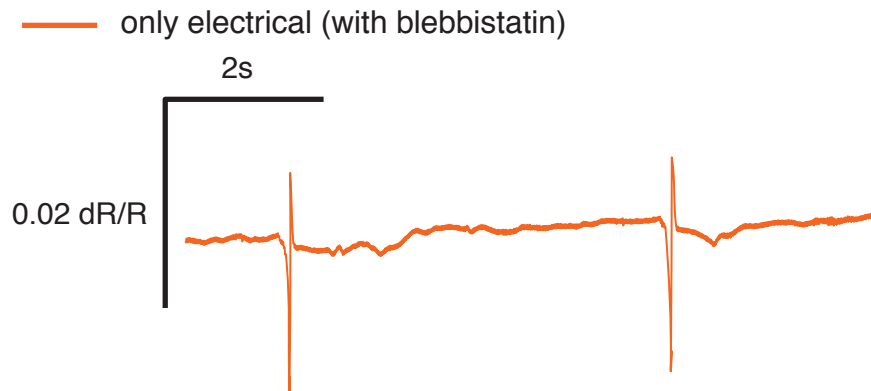
Figure 8.10: After the addition of an inhibitor of cellular contraction, the signal due to the mechanical beating disappears while the electrical signal remains strong.

Noninvasive and non-cytotoxic, the CAGE platform is compatible with small molecule drug delivery and detection. In Figure 8.10, we introduce blebbistatin, the small molecule inhibitor of myosin contraction. After incubation with blebbistatin, the optical signal attributed to mechanical beating is entirely suppressed by the small molecule inhibitor, while the electrical signal remains strong. Furthermore, with the suppression of the mechanical signal, we are able to resolve the repolarization period that follows the action potential.

8.5   Imaging bioelectric activity with spatiotemporal resolution

Two of the outstanding challenges in designing hardware for electrophysiological recordings are the complex circuit design of high-density extracellular arrays and the physical limits on electrode density due to electronic cross talk. The CAGE sensor addresses aspects of both challenges by leveraging optical detection by monolithic monolayer graphene, which permits continuous measurement across an arbitrarily large field of view as well as observation of network-scale activity with single-cell spatial resolution.

Single-shot imaging with the CAGE sensor can measure network-scale propagation of a cardiac local field potential wave across the tissue (Figure 8.11). Free of raster scanning or averaging, the infrared beam directly illuminates a $\approx$1.5 mm^2 area of graphene and the electro-optical signal from the CAGE sensor is coupled out of the waveguide and directly imaged onto a 2D InGaAs array. As cardiomyocytes fire spontaneous action potentials, the extracellular field locally modulates the reflectivity of graphene beneath the active cell. This optical modulation is amplified by the critically coupled waveguide and observed as a change in the reflection intensity at a given position in the field of view. In our experiments, the entire field of view is simultaneously monitored with 10 μm spatial resolution at a 186 Hz
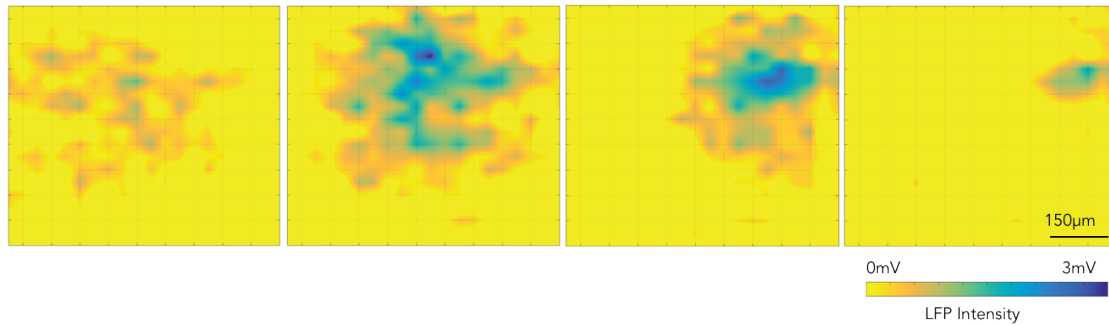
Figure 8.11: Still frames from a video of action potential waves crossing a sample of cardiac tissue under spontaneous beating conditions.

frame rate. Signals from selected spatial positions can be isolated and plotted as time traces of the local field potentials. In addition to the strength of the extracellular field, we extract the network-scale speed of potential propagation – here, we measure ≈14 cm/s from apex to base. This timescale is quite comparable to that which can be obtained through traditional
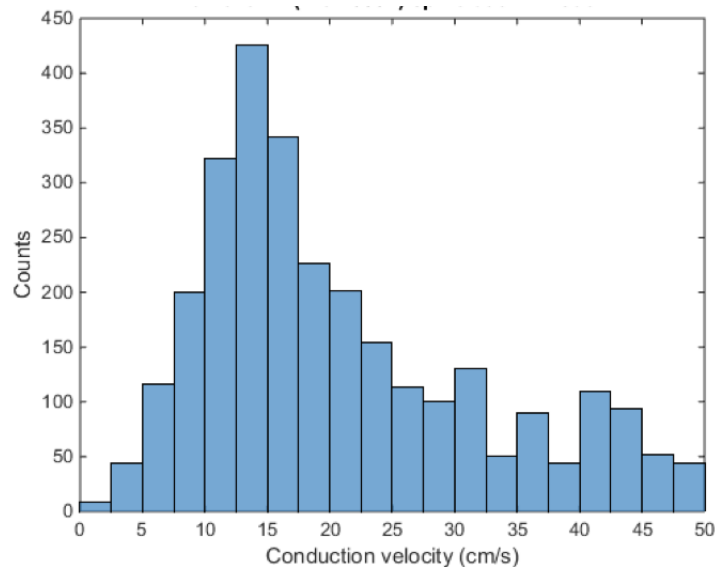
Figure 8.12: Statistics of velocity measurements taken from an MEA array of dimensions $300\mu m \times 300\mu m$ with a 200 μm pitch.

and extremely laborious MEA statistics. An example is shown in Figure 8.12 (right), where we measure the time it takes for pads on the same MEA array to receive the same signal. From this one can easily back out the velocity of the traveling action potential (15 cm/s ±5 cm/s FWHM).
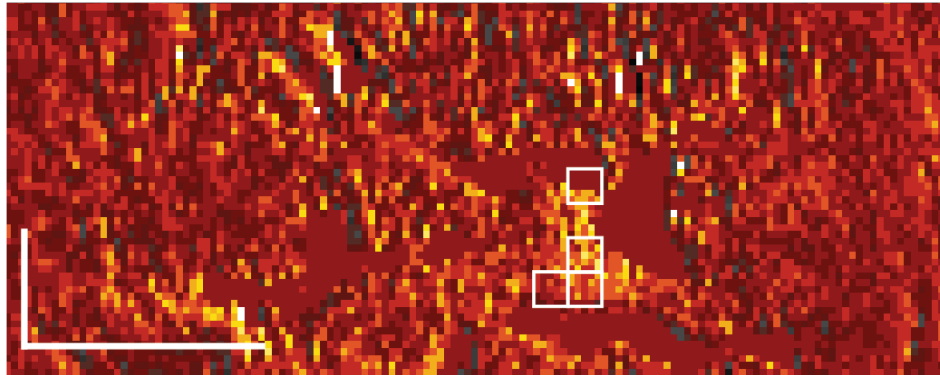
Figure 8.13: A two-dimensional CAGE image of a monolayer culture of hiPSC-CM. White
squares indicate smaller than single-cell areas selected to produce time traces of firing cells
below.

8.6 Resolving field potentials from single cells across a wide field-of-view

We can also measure single-cell extracellular field potentials from a monolayer culture of
human induced pluripotent stem cell-derived cardiomyocytes (hiPSC-CMs). Biocompatible
and robust, the devices permitted the culture of hiPSC-CMs directly on the device where
they remained healthy for weeks at a time.

A two-dimensional CAGE image encompasses a ≈ 1.5 mm^2 field-of-view, reflecting
≈ 14 μm/pixel imaged onto the 2D array (Figure 8.13). White squares indicate areas of 70
μm x 35 μm on the surface of graphene. From such an image, single-shot time traces were
extracted and overlaid from selected regions (Figure 8.14). The extracellular field potentials
had a FWHM of 5 ms and dR/R $\approx 0.11\%$ corresponding to an extracellular potential o f$\approx$
234 μV, consistent with previous reports and MEA recordings and were followed by a slowly
varying response due to the mechanical contraction of the cells. Field potential propaga-
tion can be measured between cells with ease, this time with single-cell spatial resolution
corresponding to 5 pixels/bin integrated area (Figure 8.15, 8.14). As in the myocardium
tissue, we extracted both the extracellular potential and the conduction velocity– here, we
measured $\approx$ 1.2 cm/s, typical of an immature (day 3) hiPSC-CM network [114]. In contrast
to multi-electrode arrays, in the CAGE system, we are able to easily extract signals from
contiguous regions and arbitrarily vary the integrated area.
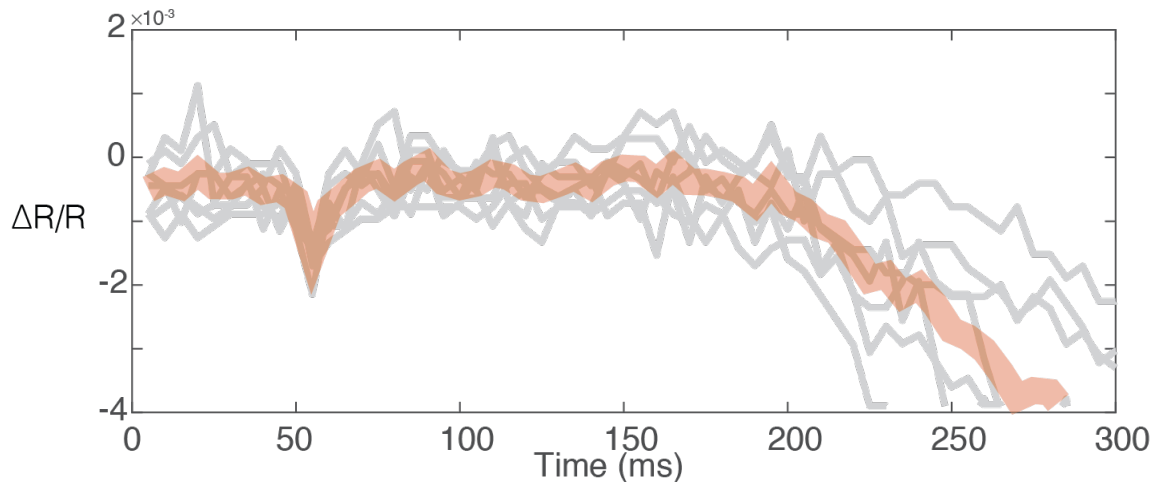
Figure 8.14: Individual (grey) and averaged (orange) time traces of single cell extracellular field potentials read from the CAGE sensor.
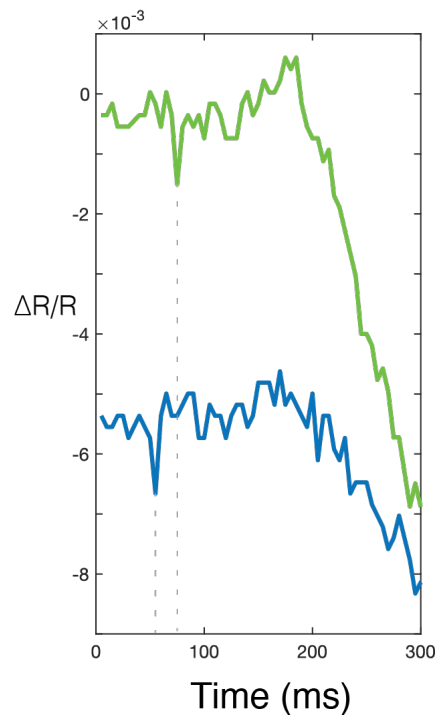
Figure 8.15: Time delay of the action potential wave as it arrives at two nearby cells.

8.7   Nonperturbative observation of network formation

One of the most striking aspects of living systems is their ability to respond to external stimuli. A single cardiomyocyte cell placed on a surface will begin to beat at 60 Hz. When
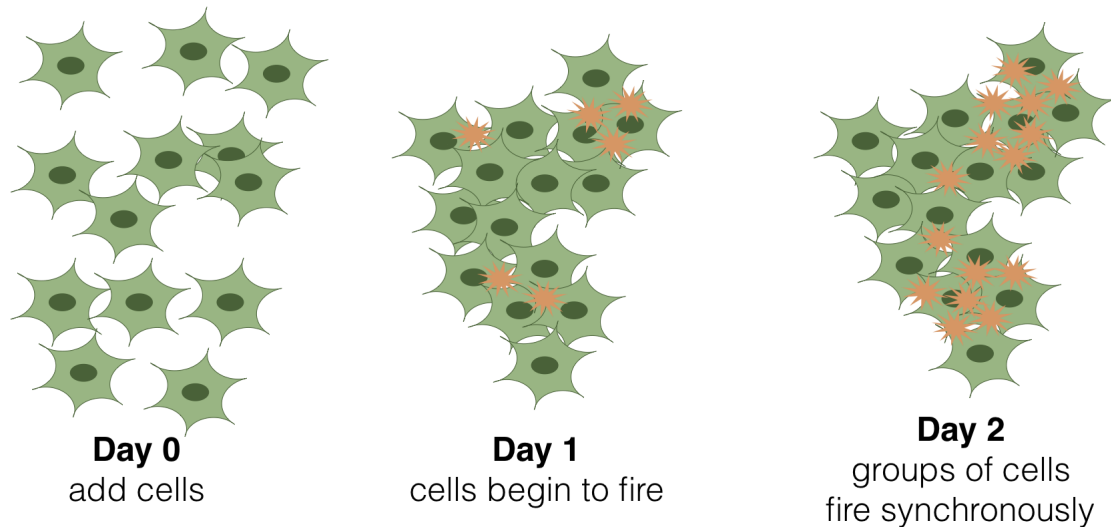
Figure 8.16: CAGE imaging of the formation of a coherent firing network in a monolayer culture of iPSC cells across a 1μm field of view.

multiple cardiomyocytes are in proximity, they will move to touch one another. Over time, these independently firing cells will begin to beat in concert. The synchronous beating is reflective of the increase in intercellular communication that literally strengthens as the cellular network emerges from the collective cell bodies. This network behavior underlies the long range communication that enables electrically active cells to function as carriers of information and regulation throughout living organisms. Using the CAGE sensor, we are able to observe this emergent behavior with single cell resolution, across a network of over 500 hiPSC-cardiomyocytes. In Figure 8.16, we show the time correlation between the beating of single cells across a monolayer of cardiomyocytes. The data plot the 2D image of the sensor surface upon which cells are cultured. The colorscale corresponds to the correlation of firing between cells relative to a fixed t=0. While on Day 1 we observe minimal coordination of cellular beating, after 48 hours, the culture has already begun to beat in concert with large areas of correlated firing are apparent. Without label, dye, or probe, we are able to observe the emergence of network-scale activity with single cell resolution.

8.8 Conclusion

In this work, we demonstrated that the critically coupled waveguide-amplified graphene electric field (CAGE) sensor enables noninvasive, label-free, real-time optical imaging of extracellular field potentials with single cell resolution across a network of electrogenic cells by leveraging the unique optical properties of graphene coupled to a photonic waveguide. Noncytotoxic, and scalable, the CAGE sensor benefits from the advantages of both electrode array recordings and optical microscopy, without the need for fluorescent tags, chemical
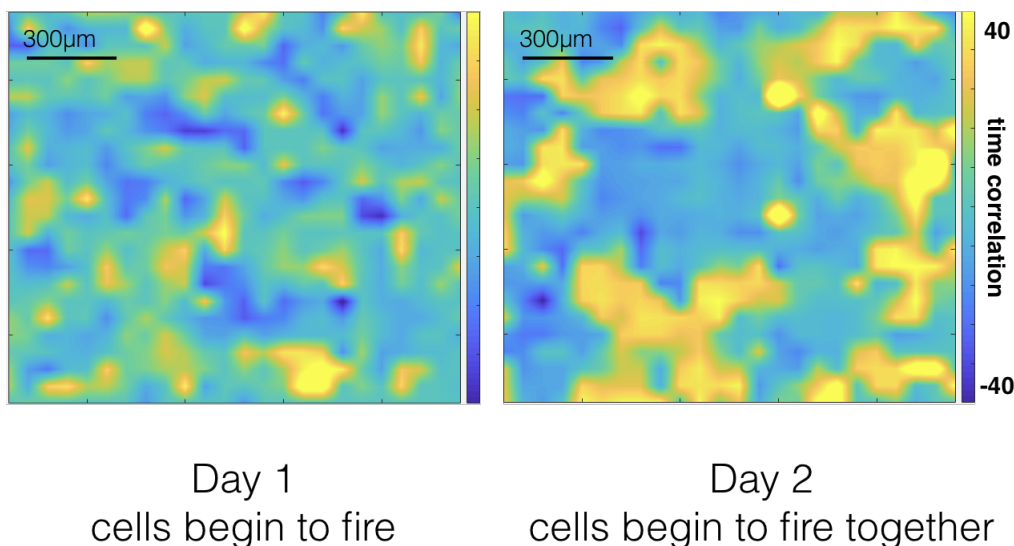
Figure 8.17: CAGE imaging of the formation of a coherent firing network in a monolayer culture of hiPSC cells across a $\approx 1\mu$m field of view.

labels, or complex circuitry. Fabrication of the sensor is commercially scalable and inexpensive, in contrast to traditional electrode arrays that rely on low-noise electrical amplification. The results presented here demonstrate the CAGE sensor can image extracellular field potentials in both tissue and monolayer cultures, permits 2D imaging of network-scale effects, and can monitor the effect of small molecule pharmacological inhibitors. The CAGE sensor is compatible with a range of chemical and thermal conditions and may be easily integrated with other techniques for simultaneous complementary measurements. Thus the CAGE device avails new opportunities for correlative measurements of bioelectric, biochemical, and biophysical processes. Future applications of the CAGE sensor with these complementary techniques could probe how electrical signaling and spatial organization of cells contribute to the formation of cellular networks or how electrical activity emerges during pluripotent stem cell differentiation.

Bibliography

[1]   William Henry Bragg. "The Atoms of Which Things Are Made". In: *Christmas At The Royal Institution*. WORLD SCIENTIFIC, Nov. 2007, pp. 199–229. DOI: `10.1142/9789812771100_0008`. URL: `http://www.worldscientific.com/doi/abs/10.1142/9789812771100%7B%5C_%7D0008`.

[2]   Charles Kittel. *Introduction to Solid State Physics*. Seventh Ed. Wiley, 1996. ISBN: 978-0-471-41526-8.

[3]   Richard Feynman. *The Feynman Lectures on Physics Volume 1*. Ed. by R. Leighton and M. Sands. Addison-Wesley, 1977.

[4]   Chetvorno. *Solid state electronic band structure*. 2017. URL: `Wikimedia%20Commons.%20Distributed%20under%20Creative%20Commons%20CC0%201.0.`.

[5]   J. M. Ziman. *Principles of the Theory of Solids*. Cambridge: Cambridge University Press, 1972. ISBN: 9781139644075. DOI: `10.1017/CBO9781139644075`. URL: `http://ebooks.cambridge.org/ref/id/CBO9781139644075`.

[6]   Paras N. Prasad and David N. Williams. *Introduction to nonlinear optical effects in molecules and polymers*. Wiley, 1991.

[7]   Nick (University of Liverpool) Greeves. *Bonding orbitals of ethylene sp2*. URL: `https://www.chemtube3d.com/orbitalsethene/`.

[8]   Wolfgang Brütting. *Physics of Organic Semiconductors*. Ed. by Wolfgang Brütting. Wiley, May 2006, pp. 1–536. ISBN: 352740550X. DOI: `10.1002/3527606637`. URL: `https://onlinelibrary.wiley.com/doi/book/10.1002/3527606637`.

[9]   M. Pope and C. E. Swenberg. *Electronic Processes in Organic Crystals and Polymers*. New York: Oxford University Press, 1999.

[10]   Eric L Spitler et al. "Lattice Expansion of Highly Oriented 2D Phthalocyanine Covalent Organic Framework Films". In: *Angewandte Chemie - International Edition* 8 (2012), pp. 2623–2627. DOI: `10.1002/anie.201107070`.

[11]   Archana Raja et al. "Coulomb engineering of the bandgap and excitons in two-dimensional materials". In: *Nature Communications* 8.1 (Aug. 2017), p. 15251. ISSN: 2041-1723. DOI: `10.1038/ncomms15251`. URL: `http://www.nature.com/articles/ncomms15251`.

[12] M. Iqbal Bakti Utama et al. "A dielectric-defined lateral heterojunction in a mono-layer semiconductor". In: *Nature Electronics* 2.2 (Feb. 2019), pp. 60–65. ISSN: 2520-1131. DOI: 10.1038/s41928-019-0207-4. URL: http://www.nature.com/articles/s41928-019-0207-4.

[13] Christian S. Diercks and Omar M. Yaghi. "The atom, the molecule, and the covalent organic framework". In: *Science* 355.6328 (Mar. 2017), eaal1585. ISSN: 0036-8075. DOI: 10.1126/science.aal1585. URL: http://www.sciencemag.org/lookup/doi/10.1126/science.aal1585.

[14] John W Colson et al. "Oriented 2D Covalent on Single-Layer Graphene". In: April (2011), pp. 228–232.

[15] Catherine R. Deblase et al. "Rapid and efficient redox processes within 2D covalent organic framework thin films". In: *ACS Nano* 9.3 (Mar. 2015), pp. 3178–3183. ISSN: 1936086X. DOI: 10.1021/acsnano.5b00184.

[16] H Wang et al. "Orientation transitions during the growth of imine covalent organic framework thin films". In: *Journal of Materials Chemistry C* (2017), pp. 5090–5095. DOI: 10.1039/C7TC01324H.

[17] John W. Colson and William R. Dichtel. "Rationally synthesized two-dimensional polymers". In: *Nature Chemistry* 5.6 (2013), pp. 453–465. ISSN: 1755-4330. DOI: 10.1038/nchem.1628. URL: http://www.nature.com/doifinder/10.1038/nchem.1628.

[18] Dana D. Medina et al. "Oriented thin films of a benzodithiophene covalent organic framework". In: *ACS Nano* 8.4 (2014), pp. 4042–4052. ISSN: 1936086X. DOI: 10.1021/nn5000223.

[19] Ryan P. Bisbey et al. "Two-dimensional Covalent Organic Framework Thin Films Grown in Flow". In: *Journal of the American Chemical Society* 138.36 (Sept. 2016), pp. 11433–11436. ISSN: 0002-7863. DOI: 10.1021/jacs.6b04669. URL: https://pubs.acs.org/doi/10.1021/jacs.6b04669.

[20] Brian J. Smith et al. "Colloidal Covalent Organic Frameworks". In: *ACS Central Science* 3.1 (Jan. 2017), pp. 58–65. ISSN: 2374-7943. DOI: 10.1021/acscentsci.6b00331. URL: https://pubs.acs.org/doi/10.1021/acscentsci.6b00331.

[21] Jeremy I. Feldblyum et al. "Few-layer, large-area, 2D covalent organic framework semiconductor thin films". In: *Chemical Communications* 51.73 (July 2015), pp. 13894–13897. ISSN: 1364548X. DOI: 10.1039/c5cc04679c.

[22] Wenyang Dai et al. "Synthesis of a Two-Dimensional Covalent Organic Monolayer through Dynamic Imine Chemistry at the Air/Water Interface". In: *Angewandte Chemie International Edition* 55.1 (Jan. 2016), pp. 213–217. ISSN: 14337851. DOI: 10.1002/anie.201508473. URL: http://doi.wiley.com/10.1002/anie.201508473.

[23] Hafeesudeen Sahabudeen et al. "Wafer-sized multifunctional polyimine-based two-dimensional conjugated polymers with high mechanical stiffness". In: *Nature Communications* 7 (Nov. 2016). ISSN: 20411723. DOI: `10.1038/ncomms13461`.

[24] Brian J. Smith et al. "Insight into the crystallization of amorphous imine-linked polymer networks to 2D covalent organic frameworks". In: *Chemical Communications* 52.18 (2016), pp. 3690–3693. ISSN: 1359-7345. DOI: `10.1039/C5CC10221A`. URL: `http://xlink.rsc.org/?DOI=C5CC10221A`.

[25] Yu Zhong et al. "Wafer-scale synthesis of monolayer two-dimensional porphyrin polymers for hybrid superlattices". In: *Science* 366.6471 (Dec. 2019), pp. 1379–1384. ISSN: 0036-8075. DOI: `10.1126/science.aax9385`. URL: `http://www.sciencemag.org/lookup/doi/10.1126/science.aax9385`.

[26] Michio Matsumoto et al. "Lewis-Acid-Catalyzed Interfacial Polymerization of Covalent Organic Framework Films". In: *Chem* 4.2 (2018), pp. 308–317. ISSN: 24519294. DOI: `10.1016/j.chempr.2017.12.011`.

[27] M. De Araújo. "Natural and man-made fibres: Physical and mechanical properties". In: *Fibrous and Composite Materials for Civil Engineering Applications*. Elsevier, 2011, pp. 3–28. DOI: `10.1533/9780857095583.1.3`. URL: `https://linkinghub.elsevier.com/retrieve/pii/B9781845695583500016`.

[28] Peter J. Waller et al. "Chemical Conversion of Linkages in Covalent Organic Frameworks". In: *Journal of the American Chemical Society* 138.48 (Dec. 2016), pp. 15519–15522. ISSN: 0002-7863. DOI: `10.1021/jacs.6b08377`. URL: `https://pubs.acs.org/doi/10.1021/jacs.6b08377`.

[29] Andrea Splendiani et al. "Emerging photoluminescence in monolayer MoS 2". In: *Nano Letters* 10.4 (2010), pp. 1271–1275. ISSN: 15306984. DOI: `10.1021/nl903868w`.

[30] Kin Fai Mak et al. "Atomically Thin MoS 2 : A New Direct-Gap Semiconductor". In: 136805.September (2010), pp. 2–5. DOI: `10.1103/PhysRevLett.105.136805`.

[31] Xiaoping Hong et al. "Ultrafast charge transfer in atomically thin MoS2 / WS2 heterostructures". In: *Nature Nanotechnology* 9.9 (2014), pp. 682–686. ISSN: 1748-3387. DOI: `10.1038/nnano.2014.167`. URL: `http://dx.doi.org/10.1038/nnano.2014.167`.

[32] Pasqual Rivera et al. "Valley-polarized exciton dynamics in a 2D semiconductor heterostructure". In: *Science* 351.6274 (Feb. 2016), pp. 688–691. ISSN: 0036-8075. DOI: `10.1126/science.aac7820`. URL: `http://www.sciencemag.org/cgi/doi/10.1126/science.aac7820`.

[33] Jonghwan Kim et al. "Observation of ultralong valley lifetime in WSe2/MoS2 heterostructures". In: *Science Advances* 3.7 (2017), pp. 1–7. ISSN: 23752548. DOI: `10.1126/sciadv.1700518`. arXiv: `1612.05359`.

[34] Chenhao Jin et al. "Ultrafast dynamics in van der Waals heterostructures". In: *Nature Nanotechnology* 13.11 (2018), pp. 994–1003. ISSN: 17483395. DOI: 10.1038/s41565-018-0298-5. URL: http://dx.doi.org/10.1038/s41565-018-0298-5.

[35] Chenhao Jin et al. *Observation of moiré excitons in WSe2/WS2 heterostructure superlattices*. Mar. 2019. DOI: 10.1038/s41586-019-0976-y. arXiv: 1812.09815.

[36] Kha Tran et al. *Evidence for moiré excitons in van der Waals heterostructures*. Mar. 2019. DOI: 10.1038/s41586-019-0975-z. arXiv: 1807.03771.

[37] Maria S. Lohse and Thomas Bein. "Covalent Organic Frameworks: Covalent Organic Frameworks: Structures, Synthesis, and Applications". In: *Advanced Functional Materials* 28.33 (Aug. 2018), p. 1870229. DOI: 10.1002/adfm.201870229.

[38] Enquan Jin et al. "Two-dimensional sp 2 carbon–conjugated covalent organic frameworks". In: *Science* 357.6352 (Aug. 2017), pp. 673–676. ISSN: 10959203. DOI: 10.1126/science.aan0202.

[39] Guillaume H V Bertrand et al. "Thiophene-based covalent organic frameworks". In: 110.13 (2017), pp. 4923–4928. DOI: 10.1073/pnas.1221824110.

[40] Shun Wan et al. "Covalent organic frameworks with high charge carrier mobility". In: *Chemistry of Materials* 23 (2011), pp. 4094–4097. ISSN: 08974756. DOI: 10.1021/cm201140r.

[41] Song Liang Cai et al. "Tunable electrical conductivity in oriented thin films of tetrathiafulvalene based covalent organic framework". In: *Chemical Science* 5.12 (2014), pp. 4693–4700. ISSN: 20416539. DOI: 10.1039/c4sc02593h.

[42] Derya Bessinger et al. "Spectrally Switchable Photodetection with Near-Infrared-Absorbing Covalent Organic Frameworks". In: *Journal of the American Chemical Society* 139.34 (Aug. 2017), pp. 12035–12042. ISSN: 0002-7863. DOI: 10.1021/jacs.7b06599. URL: https://pubs.acs.org/doi/10.1021/jacs.7b06599.

[43] Bing Sun et al. "Selective Growth of Covalent Organic Framework Ultrathin Films on Hexagonal Boron Nitride". In: *The Journal of Physical Chemistry C* 120.27 (July 2016), pp. 14706–14711. ISSN: 1932-7447. DOI: 10.1021/acs.jpcc.6b04410. URL: https://pubs.acs.org/doi/10.1021/acs.jpcc.6b04410.

[44] Song-liang Cai et al. "Tunable electrical conductivity in oriented thin films of tetrathiafulvalene based covalent organic framework". In: *Chem. Sci.* 5.12 (2014), pp. 4693–4700. ISSN: 2041-6520. DOI: 10.1039/C4SC02593H.

[45] Ergang Wang, Wendimagegn Mammo, and Mats R Andersson. "25th Anniversary Article: Isoindigo-Based Polymers and Small Molecules for Bulk Heterojunction Solar Cells and Field Effect Transistors". In: *Advanced Materials* 26.12 (Mar. 2014), pp. 1801–1826. ISSN: 09359648. DOI: 10.1002/adma.201304945. URL: http://doi.wiley.com/10.1002/adma.201304945.

[46] Derya Bessinger et al. "Spectrally Switchable Photodetection with Near-Infrared-Absorbing Covalent Organic Frameworks". In: *Journal of the American Chemical Society* 139.34 (2017), pp. 12035–12042. ISSN: 15205126. DOI: `10.1021/jacs.7b06599`.

[47] Letian Dou et al. "Low-Bandgap Near-IR Conjugated Polymers/Molecules for Organic Electronics". In: *Chemical Reviews* 115.23 (Dec. 2015), pp. 12633–12665. ISSN: 0009-2665. DOI: `10.1021/acs.chemrev.5b00165`. URL: `https://pubs.acs.org/doi/10.1021/acs.chemrev.5b00165`.

[48] Michio Matsumoto et al. "Rapid, Low Temperature Formation of Imine-Linked Covalent Organic Frameworks Catalyzed by Metal Triflates". In: *Journal of the American Chemical Society* 139.14 (Apr. 2017), pp. 4999–5002. ISSN: 0002-7863. DOI: `10.1021/jacs.7b01240`. URL: `https://pubs.acs.org/doi/10.1021/jacs.7b01240`.

[49] Fernando J. Uribe-Romo and William R. Dichtel. "Polymers stripped down". In: *Nature Chemistry* 4.4 (Apr. 2012), pp. 244–245. ISSN: 1755-4330. DOI: `10.1038/nchem.1317`. URL: `http://dx.doi.org/10.1038/nchem.1317%20http://www.nature.com/articles/nchem.1317`.

[50] David N. Bunck and William R. Dichtel. "Bulk Synthesis of Exfoliated Two Dimensional Polymers Using Hydrazone Linked Covalent Organic Frameworks". In: *Journal of the American Chemical Society* 135.40 (Oct. 2013), pp. 14952–14955. ISSN: 0002-7863. DOI: `10.1021/ja408243n`. URL: `https://pubs.acs.org/doi/10.1021/ja408243n`.

[51] Shan Wang et al. "Exfoliation of Covalent Organic Frameworks into Few-Layer Redox-Active Nanosheets as Cathode Materials for Lithium-Ion Batteries". In: *Journal of the American Chemical Society* 139.12 (Mar. 2017), pp. 4258–4261. ISSN: 0002-7863. DOI: `10.1021/jacs.7b02648`. URL: `https://pubs.acs.org/doi/10.1021/jacs.7b02648`.

[52] M. Abdul Khayum et al. "Chemically Delaminated Free-Standing Ultrathin Covalent Organic Nanosheets". In: *Angewandte Chemie International Edition* 55.50 (Dec. 2016), pp. 15604–15608. ISSN: 14337851. DOI: `10.1002/anie.201607812`. URL: `http://doi.wiley.com/10.1002/anie.201607812`.

[53] Bhaskar Nath et al. "A new azodioxy-linked porphyrin-based semiconductive covalent organic framework with I2 doping-enhanced photoconductivity". In: *CrystEngComm* 18.23 (2016), pp. 4259–4263. ISSN: 14668033. DOI: `10.1039/c6ce00168h`.

[54] Selma Duhović and Mircea Dincă. "Synthesis and Electrical Properties of Covalent Organic Frameworks with Heavy Chalcogens". In: *Chemistry of Materials* 27.16 (Aug. 2015), pp. 5487–5490. ISSN: 0897-4756. DOI: `10.1021/acs.chemmater.5b02358`. URL: `https://pubs.acs.org/doi/10.1021/acs.chemmater.5b02358`.

[55] Soyoung Kim and Hee Cheul Choi. "Light-promoted synthesis of highly-conjugated crystalline covalent organic framework". In: *Communications Chemistry* 2.1 (Dec. 2019), p. 60. ISSN: 2399-3669. DOI: 10.1038/s42004-019-0162-z. URL: http://www.nature.com/articles/s42004-019-0162-z.

[56] A G Cullis and L T Canham. "Visible Light Emission Due to Quantum Size Effects in Porous Silicon". In: *Nature* 353.September (1991), p. 335.

[57] Shun Lien Chuang. *Physics of Photonic Devices*. 2nd Editio. Hoboken, NJ: John Wiley & Sons, 2009. ISBN: 9780470293195.

[58] Haining Wang, Changjian Zhang, and Farhan Rana. "Ultrafast dynamics of defect-assisted electron-hole recombination in monolayer MoS2". In: *Nano Letters* 15.1 (Jan. 2015), pp. 339–345. ISSN: 15306992. DOI: 10.1021/nl503636c. arXiv: 1409.4518.

[59] Hongyan Shi et al. "Exciton dynamics in suspended monolayer and few-layer MoS2 2D crystals". In: *ACS Nano* 7.2 (Feb. 2013), pp. 1072–1080. ISSN: 19360851. DOI: 10.1021/nn303973r.

[60] Bernard Jusserand and Manuel Cardona. *Light Scattering in Solids V: Raman Spectroscopy of Vibrations in Superlattices*. Springer, pp. 49–152.

[61] Simil Thomas et al. "Electronic Structure of Two-Dimensional π-Conjugated Covalent Organic Frameworks". In: *Chemistry of Materials* 31.9 (2019), pp. 3051–3065. ISSN: 15205002. DOI: 10.1021/acs.chemmater.8b04986.

[62] Zheng Liu, Feng Liu, and Yong-Shi Wu. "Exotic electronic states in the world of flat bands: From theory to material". In: *Chinese Physics B* 23.7 (July 2014), p. 077308. ISSN: 1674-1056. DOI: 10.1088/1674-1056/23/7/077308.

[63] Adam E Cohen and Veena Venkatachalam. "Bringing bioelectricity to light." In: *Annual review of biophysics* 43 (2014), pp. 211–32. ISSN: 1936-1238. DOI: 10.1146/annurev-biophys-051013-022717. URL: http://www.ncbi.nlm.nih.gov/pubmed/24773017.

[64] Hideo Aiko and Mildred Dresselahus, eds. *Physics of Graphene*. Springer, 2014. ISBN: 978-3-319-02633-6. DOI: 10.1007/978-3-319-02633-6.

[65] P. R. Wallace. "The band theory of graphite". In: *Physical Review* 71.9 (1947), pp. 622–634. ISSN: 0031899X. DOI: 10.1103/PhysRev.71.622.

[66] M S Dresselhaus. *SOLID STATE PHYSICS PART I Transport Properties of Solids*. Tech. rep. 2001.

[67] R Saito, G Dresselhaus, and M S Dresselhaus. *Physical Properties of Carbon Nanotubes*. PUBLISHED BY IMPERIAL COLLEGE PRESS and DISTRIBUTED BY WORLD SCIENTIFIC PUBLISHING CO., July 1998. DOI: 10.1142/p080.

[68] A. H.. Castro Neto et al. "The electronic properties of graphene". In: *Reviews of Modern Physics* 81.1 (2009), pp. 109–162. ISSN: 0034-6861. DOI: 10.1103/RevModPhys.81.109. arXiv: 0709.1163.

[69] John R. Wallbank. "Introduction". In: 2014, pp. 1–18. DOI: 10.1007/978-3-319-07722-2_1.

[70] V. P. Gusynin and S. G. Sharapov. "Unconventional Integer Quantum Hall Effect in Graphene". In: *Physical Review Letters* 95.14 (Sept. 2005), p. 146801. ISSN: 0031-9007. DOI: 10.1103/PhysRevLett.95.146801. URL: https://link.aps.org/doi/10.1103/PhysRevLett.95.146801.

[71] Yuanbo Zhang et al. "Experimental observation of the quantum Hall effect and Berry's phase in graphene". In: *Nature* 438.7065 (Nov. 2005), pp. 201–204. ISSN: 0028-0836. DOI: 10.1038/nature04235.

[72] V. P. Gusynin and S. G. Sharapov. "Transport of Dirac quasiparticles in graphene: Hall and optical conductivities". In: *Physical Review B* 73.24 (June 2006), p. 245411. ISSN: 1098-0121. DOI: 10.1103/PhysRevB.73.245411. URL: https://link.aps.org/doi/10.1103/PhysRevB.73.245411.

[73] R. R. Nair et al. "Fine Structure Constant Defines Visual Transparency of Graphene". In: *Science* 320.5881 (June 2008), pp. 1308–1308. DOI: 10.1126/science.1156965.

[74] Rafael Yuste. "From the neuron doctrine to neural networks". In: *Nature Reviews Neuroscience* 16.8 (2015), pp. 487–497. ISSN: 1471-003X. DOI: 10.1038/nrn3962. arXiv: arXiv:1508.05133v2. URL: http://www.nature.com/doifinder/10.1038/nrn3962%7B%5C%%7D5Cnhttp://dx.doi.org/10.1038/nrn3962.

[75] Chong Xie et al. "Intracellular recording of action potentials by nanopillar electroporation." In: *Nature nanotechnology* 7.3 (Mar. 2012), pp. 185–90. ISSN: 1748-3395. DOI: 10.1038/nnano.2012.8. URL: http://www.pubmedcentral.nih.gov/articlerender.fcgi?artid=3356686%7B%5C&%7Dtool=pmcentrez%7B%5C&%7Drendertype=abstract.

[76] György Buzsáki, Costas a Anastassiou, and Christof Koch. "The origin of extracellular fields and currents–EEG, ECoG, LFP and spikes." In: *Nature reviews. Neuroscience* 13.6 (June 2012), pp. 407–20. ISSN: 1471-0048. DOI: 10.1038/nrn3241. URL: http://www.ncbi.nlm.nih.gov/pubmed/22595786.

[77] Kevin D. Dorfman et al. "Beyond Gel Electrophoresis: Microfluidic Separations, Fluorescence Burst Analysis, and DNA Stretching". In: *Chemical Reviews* 113.4 (Apr. 2013), pp. 2584–2667. ISSN: 0009-2665. DOI: 10.1021/cr3002142.

[78] C Zhang et al. "Dielectrophoresis for manipulation of micro/nano particles in microfluidic systems". In: *Analytical and Bioanalytical Chemistry* 396.1 (2010), pp. 401–420. ISSN: 1618-2642. DOI: 10.1007/s00216-009-2922-6. URL: http://dx.doi.org/10.1007/s00216-009-2922-6.

[79] Zachary R. Gagnon. "Cellular dielectrophoresis: Applications to the characterization, manipulation, separation and patterning of cells". In: *ELECTROPHORESIS* 32.18 (2011), pp. 2466–2487. ISSN: 1522-2683. DOI: 10.1002/elps.201100060.

[80] Barbaros Cetin and Dongqing Li. "Dielectrophoresis in microfluidics technology". In: *ELECTROPHORESIS* 32.18 (2011), pp. 2410–2427. ISSN: 1522-2683. DOI: 10.1002/elps.201100167. URL: http://dx.doi.org/10.1002/elps.201100167.

[81] A. Lambacher et al. "Electrical imaging of neuronal activity by multi-transistor-array (MTA) recording at 7.8 μm resolution". English. In: *Applied Physics A* 79.7 (2004), pp. 1607–1611. ISSN: 0947-8396. DOI: 10.1007/s00339-004-2991-5.

[82] M. Hutzler et al. "High-Resolution Multitransistor Array Recording of Electrical Field Potentials in Cultured Brain Slices". In: *Journal of Neurophysiology* 96.3 (2006), pp. 1638–1645. ISSN: 0022-3077. DOI: 10.1152/jn.00347.2006.

[83] Luke D Lavis and Ronald T Raines. "Bright ideas for chemical biology." In: *ACS chemical biology* 3.3 (Mar. 2008), pp. 142–55. ISSN: 1554-8937. DOI: 10.1021/cb700248m.

[84] Liang Shi Li. "Fluorescence probes for membrane potentials based on mesoscopic electron transfer". In: *Nano Letters* 7.10 (2007), pp. 2981–2986. ISSN: 15306984. DOI: 10.1021/nl071163p.

[85] Jeehae Park et al. "Screening Fluorescent Voltage Indicators with Spontaneously Spiking HEK Cells". In: *PLoS ONE* 8.12 (2013), e85221. DOI: 10.1371/journal.pone.0085221.

[86] Evan W Miller et al. "Optically monitoring voltage in neurons by photo-induced electron transfer through molecular wires." In: *Proceedings of the National Academy of Sciences of the United States of America* 109.6 (2012), pp. 2114–9. ISSN: 1091-6490. DOI: 10.1073/pnas.1120694109. URL: http://www.pubmedcentral.nih.gov/articlerender.fcgi?artid=3277584%7B%5C&%7Dtool=pmcentrez%7B%5C&%7Drendertype=abstract.

[87] Gaute T Einevoll et al. "Modelling and analysis of local field potentials for studying the function of cortical circuits". In: *Nat Rev Neurosci* 14.11 (Nov. 2013), pp. 770–785. ISSN: 1471-003X. URL: http://dx.doi.org/10.1038/nrn3599.

[88] Matthew R Angle, Bianxiao Cui, and Nicholas A Melosh. "Nanotechnology and neurophysiology". In: *Large-Scale Recording Technology (32)* 32 (June 2015), pp. 132–140. ISSN: 0959-4388. DOI: 10.1016/j.conb.2015.03.014. URL: http://www.sciencedirect.com/science/article/pii/S0959438815000690.

[89] Micha E Spira and Aviad Hai. "Multi-electrode array technologies for neuroscience and cardiology". In: *Nat Nano* 8.2 (Feb. 2013), pp. 83–94. ISSN: 1748-3387. DOI: 10.1038/nnano.2012.265. URL: http://dx.doi.org/10.1038/nnano.2012.265.

[90] Yixian Wang et al. "Imaging Local Electric Field Distribution by Plasmonic Impedance Microscopy". In: (2016). DOI: 10.1021/acs.analchem.5b04382.

[91] Jason Horng et al. "Imaging electric field dynamics with graphene optoelectronics". In: *Nature Communications* 7.1 (Dec. 2016), p. 13704. ISSN: 2041-1723. DOI: 10.1038/ncomms13704. URL: http://dx.doi.org/10.1038/ncomms13704%20http://www.nature.com/articles/ncomms13704.

[92] Feng Wang et al. "Gate-variable optical transitions in graphene." In: *Science (New York, N.Y.)* 320.5873 (2008), pp. 206–209. ISSN: 0036-8075. DOI: `10.1126/science. 1152793`.

[93] Kin Fai Mak et al. "Optical spectroscopy of graphene: From the far infrared to the ultraviolet". In: *Solid State Communications* 152.15 (2012), pp. 1341–1349. ISSN: 00381098. DOI: `10.1016/j.ssc.2012.04.064`. URL: `http://linkinghub.elsevier. com/retrieve/pii/S0038109812002700`.

[94] Ming Liu et al. "A graphene-based broadband optical modulator". In: *Nature* 474.7349 (June 2011), pp. 64–67. ISSN: 0028-0836. DOI: `10.1038/nature10067`. URL: `http: //dx.doi.org/10.1038/nature10067`.

[95] S.J. Koester and Mo Li. "Waveguide-Coupled Graphene Optoelectronics". In: *Selected Topics in Quantum Electronics, IEEE Journal of* 20.1 (Jan. 2014), pp. 84–94. ISSN: 1077-260X. DOI: `10.1109/JSTQE.2013.2272316`.

[96] Arka Majumdar et al. "Electrical Control of Silicon Photonic Crystal Cavity by Graphene". In: *Nano Letters* 13.2 (Feb. 2013), pp. 515–518. ISSN: 1530-6984. DOI: `10.1021/nl3039212`.

[97] Ren-Jye Shiue et al. "Enhanced photodetection in graphene-integrated photonic crystal cavity". In: *Applied Physics Letters* 103.24 (2013). DOI: `http://dx.doi.org/10. 1063/1.4839235`. URL: `http://scitation.aip.org/content/aip/journal/apl/ 103/24/10.1063/1.4839235`.

[98] Xuetao Gan et al. "Strong enhancement of light-matter interaction in graphene coupled to a photonic crystal nanocavity". In: *Nano Lett.* 12.11 (2012), p. 5626. ISSN: 1530-6992. DOI: `10.1021/nl302746n`. URL: `http://www.ncbi.nlm.nih.gov/ pubmed/23043452`.

[99] A N Grigorenko, M Polini, and K S Novoselov. "Graphene plasmonics". In: *Nat Photon* 6.11 (Nov. 2012), pp. 749–758. ISSN: 1749-4885. DOI: `10.1038/nphoton. 2012.262`. URL: `http://dx.doi.org/10.1038/nphoton.2012.262`.

[100] Jianing Chen et al. "Optical nano-imaging of gate-tunable graphene plasmons". In: *Nature* (2012), pp. 3–7. ISSN: 0028-0836. DOI: `10.1038/nature11254`. URL: `http: //www.nature.com/doifinder/10.1038/nature11254`.

[101] Z. Fei et al. "Gate-tuning of graphene plasmons revealed by infrared nano-imaging". In: *Nature* 487.7405 (2012), pp. 82–85. ISSN: 0028-0836. DOI: `10.1038/nature11253`. URL: `http://www.nature.com/doifinder/10.1038/nature11253`.

[102] Seung Hoon Lee et al. "Ultrafast refractive index control of a terahertz graphene metamaterial". In: *Scientific Reports* 3 (July 2013), p. 2135. URL: `http://dx.doi. org/10.1038/srep02135`.

[103] Yonghao Liu et al. "Approaching total absorption at near infrared in a large area monolayer graphene by critical coupling". In: *Applied Physics Letters* 105.18 (2014). DOI: `http://dx.doi.org/10.1063/1.4901181`. URL: `http://scitation.aip.org/content/aip/journal/apl/105/18/10.1063/1.4901181`.

[104] Eugene Hecht. *Optics*. 3rd Editio. 1998. ISBN: 021304252.

[105] S Zhu et al. "Frustrated total internal reflection: A demonstration and review". In: *Citation: American Journal of Physics* 54 (1986), p. 601. DOI: `10.1119/1.14514`. URL: `https://doi.org/10.1119/1.14514`.

[106] J.D. Jackson. *Classical Electrodynamics*. 3rd Editio. Wiley. ISBN: 978-0471309321.

[107] Yi-Lin Huang, Alison S. Walker, and Evan W. Miller. "A Photostable Silicon Rhodamine Platform for Optical Voltage Sensing". In: *Journal of the American Chemical Society* 137.33 (Aug. 2015), pp. 10767–10776. ISSN: 0002-7863. DOI: `10.1021/jacs.5b06644`. URL: `https://pubs.acs.org/doi/10.1021/jacs.5b06644`.

[108] Nina Vogt. "A bright future for voltage imaging". In: *Nature Methods* 16.11 (Nov. 2019), pp. 1076–1076. ISSN: 1548-7091. DOI: `10.1038/s41592-019-0653-y`. URL: `http://www.nature.com/articles/s41592-019-0653-y`.

[109] Ahmed S. Abdelfattah et al. "Bright and photostable chemigenetic indicators for extended in vivo voltage imaging". In: *Science* 365.6454 (Aug. 2019), pp. 699–704. ISSN: 0036-8075. DOI: `10.1126/science.aav6416`. URL: `http://www.sciencemag.org/lookup/doi/10.1126/science.aav6416`.

[110] Silvia Ronchi et al. "Single-Cell Electrical Stimulation Using CMOS-Based High-Density Microelectrode Arrays". In: *Frontiers in Neuroscience* 13 (Mar. 2019). ISSN: 1662-453X. DOI: `10.3389/fnins.2019.00208`. URL: `https://www.frontiersin.org/article/10.3389/fnins.2019.00208/full`.

[111] Jan Müller et al. "High-resolution CMOS MEA platform to study neurons at subcellular, cellular, and network levels". In: *Lab on a Chip* 15.13 (2015), pp. 2767–2780. ISSN: 1473-0197. DOI: `10.1039/C5LC00133A`. URL: `http://xlink.rsc.org/?DOI=C5LC00133A`.

[112] M. Hutzler et al. "High-Resolution Multitransistor Array Recording of Electrical Field Potentials in Cultured Brain Slices". In: *Journal of Neurophysiology* 96.3 (Sept. 2006), pp. 1638–1645. ISSN: 0022-3077. DOI: `10.1152/jn.00347.2006`. URL: `https://www.physiology.org/doi/10.1152/jn.00347.2006`.

[113] Francesca Santoro et al. "Interfacing Electrogenic Cells with 3D Nanoelectrodes: Position, Shape, and Size Matter". In: *ACS Nano* 8.7 (July 2014), pp. 6713–6723. ISSN: 1936-0851. DOI: `10.1021/nn500393p`. URL: `https://pubs.acs.org/doi/10.1021/nn500393p`.

[114] Hyun Seok Hwang et al. "Comparable calcium handling of human iPSC-derived cardiomyocytes generated by multiple laboratories". In: *Journal of Molecular and Cellular Cardiology* 85 (Aug. 2015), pp. 79–88. ISSN: 00222828. DOI: `10.1016/j.yjmcc.2015.05.003`. URL: `https://linkinghub.elsevier.com/retrieve/pii/S0022282815001510`.

Part III

Appendices

Appendix A

Methods for graphene transfer and sample preparation

A.1   Sample preparation

The CAGE imaging structure consists of 1000 nm SiO2 (coupling layer) and 150 nm Ta2O5 (waveguide layer) deposited on one face of a 1 cm per side equilateral SF-11 glass prism by ion-assisted deposition. The structure was designed using a custom Python simulation and fabricated by Edmund Optics. A large area graphene film was grown on copper foil using chemical vapor deposition (CVD). A 1-cm^2 area graphene was transferred onto the waveguide surface by PMMA-supported transfer. We obtain high-quality large-area graphene with near-uniform optical absorption at the device/solution interface. The Pt(2 nm)/Au(60 nm) electrodes were deposited on the graphene to make electrical contacts. The metal electrodes were insulated with nitrocellulose lacquer to prevent water-Au chemical reactions during measurements. The device was mounted in a solution chamber printed from PR48 resin (Autodesk) which permits access to the device from both the top and bottom. All data were obtained in a saline solution (155 mM NaCl, 2.966 mM Na2HPO4, -7H2O, 1.0588mM KH2PO4) except for imaging data obtained in 1 mg/L NaCl in water to accommodate the camera's frame rate. An external gate voltage Vg (0.53 V) was applied through a Ag/AgCl electrode in solution to set the Fermi energy of graphene and to test the optical response of CAGE detection under electrostatic gating. For the spatially resolved measurements, an external gate voltage Vg (1.1 V) was applied through the microelectrode, whose high impedance at the electrode/solution interface requires a larger applied voltage but yields the same voltage bias and critical coupling condition at the detector's graphene/solution interface. A 10mV electrical pulse generates a 1.8 mV local field at the graphene/solution interface beneath the Pt/Ir microelectrode tip (World Precision Instruments, Nr.PTM23B05KTH). To this we applied a small modulation to the micro-positioned microelectrode insulated in parylene with only the final 2μm exposed to the solution.

A.2 Optical measurements

Figure 7.2 shows, in detail, the optical set-up used in the study. A stable, 1.55 μm, 15 mW laser beam is generated by a butterfly telecomm laser (Newport Model 708 8-Channel Butterfly) with a current and temperature controller (Newport Model 9016 Modular Controller). The polarization is tuned to the TE-direction by a half-wave plate and further cleaned by a calcite polarizer. In the imaging mode, the incident beam is collimated and coupled into the CAGE platform for optimal sensitivity. In the scanning detection mode, the incident beam is controlled with a 17.5 cm focusing lens to have an NA=0.002 and selects an area at the graphene interface. The incident light couples into the waveguide from one side of the prism. The prism coated with the planar waveguide is placed on a XY-translational stage and a rotating stage which allow for fine-tuning of the sample position and incident angle. The reflected light is then collected by a 10X MPlan objective and sent into an In-GaAs two-dimensional camera (Allied Vision Technologies Goldeye 008 SWIR), an InGaAs one-dimensional camera (Andor 1.7 μm InGaAs DU490A) and into a low-noise InGaAs photodetector, respectively. A circular iris is used to select the probing area for photodiode measurements.

A.3 Preparation and transfer of CVD graphene

The growth and prepartion of monolayer CVD graphene is critical to the fabrication of the CAGE device. The most important parameters to imaging graphene are (1) the continuity of monolayer graphene (2) the absence of bilayer islands, (3) the homogeneity of the monoalyer across the imaging area. Deviations from perfection cause inhomogeneous doping and a decreased sensitivity across the surface of the detector.

Preparation:

1. RIE to remove the backside graphene (45 seconds at 100 watts)

2. Optional: polymeric polycarbonate has been found to be an effective protecting layer on monolayer CVD graphene. We found that it was indeed effective in producing high quality transfers. However, we note that it likely changed the intrinsic doping of CVD graphene, which results in a baseline shift of the charge neutral point. As a consequence, the gating required to reach critical coupling was 100 meV offset for prisms made with the PC protecting layer during transfer. Spin coat PC(3% in Chloroform) on graphene/Cu with a speed of 3000 RPM for 60 seconds. Acceleration should be set to maximum. There should be enough PC that it nearly reaches the edges of the carbon foil but does not yet touch them, else the underside will also remain, damaging the resulting monolayer.

3. Spin coat PMMA (A2 or A4, 495K or 950K) on top of the PC film using the same parameters as the above.

4. Etch away copper in Ammonium Persulfate, Sodium Persulfate, or FeCl3. Note: FeCl3 will etch Cu faster and more thoroughly. We find FeCl3 is better for the homogeneity desired in optical measurements but worse for transport.

5. Float PMMA/PC/Graphene stack in water for 1 hour

6. Repeat 3 times, with the third float overnight.

7. Pick up with target substrate (such as the wave guide prism). Contact the graphene film at a small angle, then increase the angle as you pull up.

8. Dry the sample using an air gun. Do not dry using a hot plate.

9. Develop the PC/PMMA layers in Acetone, DCM, or Chloroform overnight

10. Rinse in IPA and dry under nitrogen. Keep covered until use.

Index